2007

Improving hardness and toughness of boride composites based on AlMgB14

Justin Steven Peters
Iowa State University

Improving hardness and toughness of boride composites based on $AlMgB_{14}$

by

Justin Steven Peters

A dissertation submitted to the graduate faculty

in partial fulfillment of the requirements for the degree of

DOCTOR OF PHILOSOPHY

Major: Materials Science and Engineering

Program of Study Committee:
Alan Russell, Major Professor
Ashraf Bastawros
S. Bulent Biner
L. Scott Chumbley
Ralph Napolitano

Iowa State University

Ames, Iowa

2007

Table of Contents

Abstract

The search for new super-hard materials has usually focused on strongly bonded, highly symmetric crystal structures similar to diamond. The two hardest single-phase materials, diamond and cubic boron nitride (cBN), are metastable, and both must be produced at high temperatures and pressures, which makes their production costly. In 2000, a super-hard composite based on a low-symmetry, boron-rich compound was reported. Since then, many advances have been made in the study of this $AlMgB_{14}$ - TiB_2 composite. The composite has been shown to exhibit hardness greater than either of its constituent phases, relying on its sub-micron microstructure to provide hardening and strengthening mechanisms. With possible hardness around 40 GPa, an $AlMgB_{14}$ - 60 vol% TiB_2 approaches the hardness of cBN, yet is amenable to processing under ambient pressure conditions.

There are interesting aspects of both the $AlMgB_{14}$ and TiB_2 phases. $AlMgB_{14}$ is comprised of a framework of boron, mostly in icosahedral arrangements. It is part of a family of 12 known compounds with the same boron lattice, with the metal atoms replaced by Li, Na, Y or a number of Lanthanides. Another peculiar trait of this family of compounds is that every one contains a certain amount of intrinsic vacancies on one or both of the metal sites. These vacancies are significant, ranging from 3 to 43 % of sites depending on the composition.

TiB_2 is a popular specialty ceramic material due to its high hardness, moderate toughness, good corrosion resistance, and high thermal and electrical conductivity. The major drawback is the difficulty of densification of pure TiB_2 ceramics. A combination of sintering aids, pressure, and temperatures of 1800ºC are often required to achieve near full density articles. The $AlMgB_{14}$ - TiB_2 composites can achieve 99% density from hot-pressing at 1400ºC. This is mostly due to the preparation of powders by a high-energy milling technique known as mechanical alloying. The resulting fine powders have high activity, and Fe from wear debris acts as a sintering aid. Mechanical alloying improves the sinterability of the composite material, it has the same effect on pure TiB_2. TiB_2 processed by high-energy milling has been found to achieve 99% theoretical density at 1400ºC with the addition of ~1 wt% Fe.

Both the $AlMgB_{14}$ - TiB_2 composites and pure TiB_2 produced from these methods have enhanced mechanical properties due to their fine microstructures. These materials show exceptional promise in the field of wear resistance. This includes cutting tools, erosion resistant coatings, and low-friction sliding contacts to name a few. Under certain wear conditions, the composite material can show performance on par with that of current high-end cBN and WC materials tailored for wear resistance. The composite material also exhibits low reactivity with Ti alloys, a pre-requisite for effective machining of these alloys, a trait that few hard materials possess.

Chapter 1: Introduction

1.1: Introduction

The search for new super-hard materials has usually focused on strongly bonded, highly symmetric crystal structures similar to diamond. The two hardest single-phase materials, diamond and cubic boron nitride (cBN), are metastable, and both must be produced at high temperatures and pressures, which makes their production costly. Materials are considered super- and ultra-hard if their indentation hardness is greater than 40 and 70 GPa, respectively, correlating to the hardness ranges of cBN and diamond [1]. There exist many other hard materials such as tungsten carbide (WC) and alumina (Al_2O_3) that are less expensive to produce but exhibit significantly lower hardness. A variety of materials containing boron icosahedra also show high intrinsic hardness, though their hardness is not comparable to ultra-hard materials [2]. These crystal structures have lower symmetry than other common hard materials, and their unit cells are more complex.

Many compounds based on the icosahedral boron framework of $AlMgB_{14}$ have been discovered in the past few decades, but only recently has much interest been shown in their high hardness. New production methods and the addition of reinforcement phases have resulted in bulk materials with hardness comparable to cBN [3]. Measurements performed on single crystals of compounds isostructural with $AlMgB_{14}$ have shown high intrinsic hardness [4-6]. Interestingly, the occupancies of the metal atom sites in these structures are also less than 100% [6-12]. What roles the various elements or

occupancies play in the hardness and other properties of these materials are still poorly understood. The complex structures of these compounds may shed some light on how bonding and crystal structure relate to hardness because they are quite different than most common hard materials that possess simple crystal structures. Figure 1.1 below shows the structure of $AlMgB_{14}$, an icosahedral boron framework with interstitial Al (green) and Mg (red) atoms.

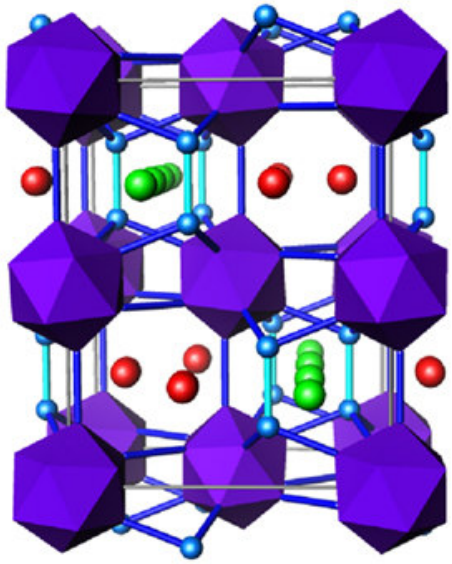

Figure 1.1: Atom positions in $AlMgB_{14}$, space group *Imam*. Blue and purple correspond to B and B icosahedra; red and green represent Mg and Al sites, respectively, assuming full occupancy of Mg and Al sites. [Modeled by Bruce Harmon, 1999]

The discovery of low-cost, super-hard materials would have great potential benefits for many industries where machining, grinding, and cutting are commonplace. Many applications in which advanced high-performance metals and ceramics could be used are hindered by the high cost of cutting and machining such strong, hard materials. At present, expensive super-hard cutting tools are needed to fabricate engineering parts from these materials. Even with super-hard cutting tools, tool lifetime is often disappointingly short due to reactivity between the tool and workpiece [13].

The goal of this project is to better understand the mechanisms that lead to high hardness in $AlMgB_{14}$ and its composites. This knowledge will be applied in hopes of producing composites with high hardness and toughness suitable for industrial cutting, grinding, and wear-resistant applications.

1.2: Thesis Organization

This dissertation is comprised of a general introduction to hard materials and $AlMgB_{14}$ composites followed by four journal articles and a general discussion containing additional results. Chapter 3 discusses the indexing of Mg_2B_{14}, a compound isostructural with $AlMgB_{14}$. Chapter 4 is an investigation of impurities and hardness in $AlMgB_{14}$. Chapter 5 involves the addition of TiB_2 reinforcement to $AlMgB_{14}$ and resulting hardness, microstructure, and erosion resistance. Chapter 6 examines the microstructure and erosion resistance of TiB_2 sintered from mechanically alloyed powders at comparatively low temperatures.

1.3: Hardness

Hardness is a measure of a material's resistance to plastic deformation, which usually occurs by motion of dislocations through the crystal. Traditional hard materials resist dislocation motion by the strength and arrangement of their interatomic bonds. Until the late 20th century, research on hard materials focused almost exclusively on *intrinsically* hard materials (e.g., those with simple, highly symmetric crystal structures and short bond lengths). Within the past decade, hard materials research has broadened to include

extrinsically hard materials, those whose high hardness is derived from their microstructures, as well as from their crystal structures and bond lengths.

Hard Materials.

The only two intrinsically super-hard bulk materials currently known are diamond and cBN. While cBN is only one-half to two-thirds as hard as diamond, it is quite similar to diamond. Both have the same crystal structure, commonly known as diamond cubic (space group *Fd3m*, and Pearson cF8), resulting in short, strong, tetrahedral bonds. They are also metastable crystal structures at ambient temperature and pressure; a hexagonal graphitic structure is the equilibrium structure for both C and BN (s.g. $P6_3/mmc$, Pearson hP4). The graphitic forms of each compound have drastically reduced mechanical properties. High pressure (~5 GPa or greater) and high temperature (~1800˚C) are required to convert the graphitic form to the diamond cubic structure [14]. Perhaps the greatest difference between diamond and cBN is the nature of the bonding. The tetrahedral bonds in diamond are nearly 100% covalent, while in cBN the covalency is reduced to 75% (25% ionic) [14]. Covalent bonding is strong and directional, whereas ionic character delocalizes the bonding, which is responsible for the large difference in hardness between the two compounds. As covalency is important for strong bonding, highly-symmetric crystal structures are typically another requirement for hard materials. Lattices with low symmetry may possess strong bonding, yet contain planes of low packing density and suffer from higher anisotropy, which can have an impact on hardness.

Table 1.1: Hardness and other selected properties of hard materials.

	Density (g/cm^3)	Hardness (GPa)	Bulk Modulus (GPa)	Shear Modulus (GPa)
C (diamond)	3.52	70-100	443	535
BN (cubic)	3.48	45-50	400	409
C_3N_4 (cubic)	1.95[15]	40-55	496	332
B_4C	2.52	38-44	292[16]	188[17]
TiB_2	4.50	26-33	244	263
WC	15.72	23-30	439[18]	282[18]
TiC	4.93	28-29	241	188
SiC	3.22	24-28	226	196
Al_2O_3	3.98	21-22	246	162
Si_3N_4	3.19	17-21	249	123
$AlMgB_{14}$ (baseline)	2.66	28-35	160-190	160
$AlMgB_{14}$ + 30 wt% TiB_2 *	3.22	33-46	180-190	175
$AlMgB_{14}$ + 70 wt% TiB_2 *	3.82	37-42	200-240	200-220
nc-TiN/a-Si_3N_4 †		40-100†		

Unless otherwise specified, values from Cook et al. [3].

* 30 and 70 weight % TiB_2 correspond to 21 and 59 volume % TiB_2, respectively.

† Nanocrystalline TiN and amorphous Si_3N_4 composite, Vepřek et al. [19].

Modeling calculations suggest that C_3N_4 would be an intrinsically super-hard material, but experimental verification of that prediction has been lacking [20]. The claim to high hardness was based on predictions of its bulk modulus, which is possibly greater than that of diamond. As with diamond and cBN, the hard cubic phase of this compound is also metastable, and as such has not yet been produced in single phase or bulk form [15,21]. Theoretical modeling has been used in the past to predict new hypothetical super-hard materials. Many of these investigations are based on the assumption that bulk modulus is directly related to hardness [20,22]. While high elastic modulus can be a good indicator for high hardness, it is an elastic property and not directly related to plastic behavior. Since plastic deformation occurs under shear stress, some contend that shear modulus is a better indication of high hardness potential [18,23-24]. Often, bulk modulus is used

because it is easier to calculate than shear modulus; shear can change the symmetry of a lattice and introduce additional elastic constants into the calculations [25].

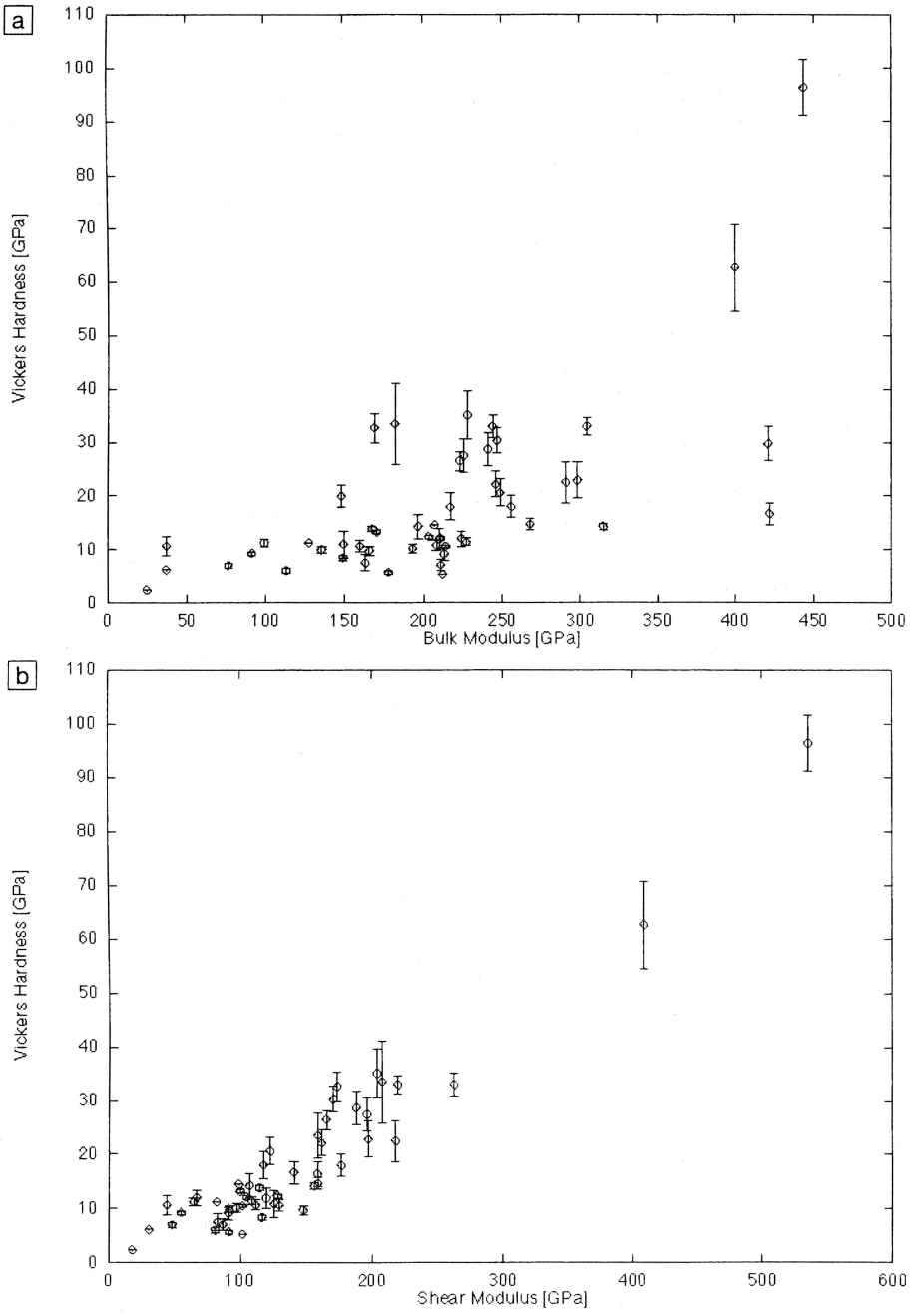

Figure 1.2: Hardness versus bulk modulus (a) and shear modulus (b) for many materials from Teter [23].

Bulk modulus can be a deceptive gauge of actual hardness. For example, WC has a bulk modulus between that of diamond and cBN (All three are greater than 400 GPa) yet its hardness is considerably lower than either (see Table 1.1). On the other hand, WC's shear modulus is significantly lower in comparison, which correlates more closely to the hardnesses of WC, cBN, and diamond [18]. Teter plotted the known hardness of about 50 materials versus bulk modulus and shear modulus as shown in Figure 1.2 [23]. Hardness vs. shear modulus indicates a strong linear trend. In a plot of hardness vs. bulk modulus, the data points fill a triangle, with an upper bound similar to the previous graph while many points fall far below in hardness.

Other approaches to creating novel hard materials rely heavily on extrinsic properties, such as modifications of the microstructure of a material and/or the interaction of two or more phases. Fine crystallites, grain boundaries, amorphous phases, and compressive stresses can be produced in strongly bonded materials in order to impede dislocation motion. There are many challenges associated with achieving and manipulating these conditions to produce a material with high hardness. The Hall-Petch equation is a well known relationship between decreasing grain size and increasing yield strength due to increasing barriers to dislocation motion [26]. It should be noted that this applies to ductile failure; in brittle materials, failure occurs by fracture and not by deformation due to dislocation motion. Brittle materials therefore have higher resistance to dislocation motion than to fracture, lower resistance to fracture being a consequence of critical-sized flaws.

Hard materials tend to be brittle (though not all brittle materials are hard) due to their inherent resistance to dislocation motion, so in these materials conditions for brittle fracture are usually met before those for plastic deformation. Such conditions imply the involvement of tensile stresses of some form. Under sufficiently high compressive stress, all materials deform plastically, as tensile fracture is impossible. It is only under compressive stress that hardness is applicable and measurable, as the property of hardness is a material's resistance to plastic deformation. Therefore, the Hall-Petch relationship can apply to the hardness of brittle materials, though not other properties such as tensile strength. Grain size is inversely proportional to grain boundary fraction, but if the grain boundaries are not comparable in strength to the lattice, the material will suffer a serious decline in hardness as grain boundary sliding begins to dominate. This is one of the mechanisms behind the reverse Hall-Petch relationship, and stronger grain boundaries can suppress this effect to finer grain sizes [27-28].

Vepřek has selected materials and methods that take advantage of all these effects to produce stable composites with the same hardness as diamond [19,22,29-33]. By depositing an amorphous film from two mutually insoluble hard phases, a strong driving force results in the spinodal decomposition of very fine nanocrystallites. In the case of TiN/Si_3N_4 mixtures, around 3 nm TiN crystals are segregated by an approximately 1 nm thick layer of amorphous Si_3N_4 [29,32]. Plasma-assisted chemical vapor deposition (PACVD) is used to deposit these coatings; one benefit of this is that the ratio of species in the vapor can be adjusted to optimize the properties of the film. The very fine nanostructure and mixture of crystalline and amorphous phases impede dislocation

motion, while sharp grain boundaries prevent sliding and the onset of the reverse Hall-Petch effect.

Vepřek also makes a distinction between materials in which super-hardness (and ultra-hardness) arises from microstructure and those in which it arises from strain [19,34-35]. In the latter, strain can, for instance, be the result of defects from ion bombardment or residual bi-axial compressive stress in un-annealed films. Such hardness is not intrinsic to the material, is strongly anisotropic, and commonly has poor thermal stability. Materials in which super-hardness is a result of an ordered or self-ordering nanocomposite have come to be known as superlattices or heterostructures [19,31,36]. Despite 1-5 nm features, Vepřek reports retention of hardness and crystallite size of heterostructures of TiN/Si_3N_4 up to 1100ºC [32-33]. Hardnesses of 40 to >100 GPa have been reported for these nanocomposites, with substantial efforts taken to ensure such values are not the result of residual stress or artifacts of measurement [19,30-31]. This method of producing high-hardness material has the disadvantage that it can be used only to produce thin films. Producing bulk materials in this way would require weeks-long deposition times.

A variety of super-hard materials has been created by thin film deposition techniques. Studies of TiB_2 thin films have shown that B contents above the stoichiometric concentration can enhance the hardness of the film [37-39]. $TiB_{2.4}$ films have exhibited hardness as high as 70 GPa after annealing to remove residual stress, approaching the realm of ultra-hardness [38-40]. The high energy of formation of TiB_2 and its narrow

solubility range result in a film of columns of TiB_2 about 5 nm in diameter which grow in the direction of the deposition. The enhancement in hardness results from the excess B forming a thin, amorphous "tissue" around each column [39]. Although the columnar arrangement of the TiB_2 nanocrystals may result in markedly anisotropic properties, these films share many similarities with Vepřek's self-organized heterostructures.

Similarly, cBN nanocomposites produced at pressures of 18 GPa and temperatures around 1800ºC have been reported with hardnesses as high as 85 GPa [41]. In these composites, cBN nanocrystals are interspersed with a modified structure, wBN. This is a wurtzite type structure between that of the cubic and graphitic forms, containing sp^3 bonds like the cubic form, which is sometimes called the hexagonal diamond structure as it can also be found in carbon [42]. In this and the nano-columnar TiB_2 composites, the reduction in grain size results in increased hardness, but this alone is not sufficient for the hardness achieved. In each composite, variations in composition or structure resulted in the presence of another, significantly softer phase (B or wBN) than the parent material (TiB_2 or cBN). Yet this softer phase can further enhance hardness by blocking dislocation motion and enhancing the stability of the nano-sized grains. Without the presence of this second phase, the nanocrystals would likely have grown much larger on formation or at least showed very poor thermal stability.

Other heterostructures can be formed manually if they will not self-assemble. Films of TiN/NbN approached 80 GPa in hardness by alternating the deposition of each into layers

[43]. Such an approach is difficult, though, and even more time consuming and impractical for large scale operations than most film deposition techniques.

Measuring Hardness.

At some point during any discussion of hardness, the question needs to be asked: "What exactly does hardness mean?" It is by no means a fundamental property of a material. Like modulus, tensile strength, and toughness, it is related to bond strength and crystal structure. As discussed earlier, there is debate as to whether bulk or shear modulus is the better indicator of hardness. Yet they are only indications, and there is no equation that relates modulus to hardness, tensile strength, etc. for all materials. Since the moduli are elastic properties, they are independent of the brittle or ductile nature of a material and are valid only for comparison between materials. Properties such as tensile strength, bend strength, and compressive strength for the most part evaluate only the plastic properties of ductile materials. Hardness on the other hand, is a measure of deformation under constrained compressive loading where both brittle and ductile materials behave plastically. Thus, perhaps the most significant value of hardness as a property is that it can be used to directly compare the limits of elasticity of all materials.

Since hardness is a measure of resistance to plastic deformation, the most basic way to compare hardness is to see which material will scratch another. That is the basis for one of the first scales of hardness, the Mohs scale, invented in the early 1800's [26]. By using milestones of popular (though not necessarily common) minerals, unknown materials were ranked between 1 (talc) and 10 (diamond). This is a simple test and does

not require the measurement of the parameters of the test (force, depth, etc.) only "scratch or be scratched." This is a very qualitative test, and the scale used is far from linear or even regular. Perhaps a more controlled experiment would be to scratch a material with a much harder one, using a constant force, and measure the width of the scratch. With the width of the scratch and the force used, the pressure or stress required to cause deformation can be calculated. Since the length of the scratch is unimportant, the shortest scratch possible is an indentation, which has become the modern method of hardness testing.

Indentation hardness (specifically static indentation hardness) is the most common type of hardness measured. Yet there are many ways of measuring indentation hardness, each with its pros and cons. In addition, each has its own scale for ranking hardness, though they are all far more linear (or at least systematic) than the Mohs scale. Due to various differences in each type of test, the scales also cannot be converted between each other with 100% consistency for all materials. The earliest popular scale, the Brinell scale, uses a spherical indenter of WC or hardened steel under a known load (or force) and measures the width of the indentation [26]. The drawback to this method is that both the force and the diameter of the ball are important, as the slope of the ball where it meets the sample surface can have elastic, frictional, and other effects that can introduce deviations into the measurement. This makes comparison between materials of great difference in hardness difficult, as well as the comparison of results obtained with different load or indenter diameter. The indentations are also usually around a few millimeters in diameter, considered large by many more modern tests. As with all hardness tests, the

test becomes less reliable as the material approaches the hardness of the indenter. With the Brinell test, large spherical indenters of materials harder than WC can become prohibitively expensive.

Another method, Rockwell hardness, actually consists of a number of scales and indenter types, depending on the hardness range of the material in question [26]. It is popular in industry, especially in the United States, because it is fast and reliable when only relatively small differences in hardness need to be known. By measuring the depth of indentation mechanically, it eliminates the need for analysis with a microscope. It has much less value in the scientific community due to its many different scales, which are for the most part limited to the range of hardnesses found in steels.

Designed to address some of the problems with the Brinell test, the Vickers hardness test was created so that hardness values would be independent of the size of the indenter [26]. Beyond a threshold value, it is also largely independent of testing load. This test incorporates a square pyramidal diamond indenter with an angle of 136º between opposite faces. This is equal to an angle of 22º between each face and the sample, because this was the angle between ball and sample at what was thought to be the most desirable penetration during a Brinell indentation test. Since a diamond indenter is used, a wide range of materials can be tested. This is also called the Vickers microhardness test because indents 20 μm across or greater are typically all that is necessary, and they are measured with a microscope. (Tests such as Brinell and Rockwell which produce larger indents are typically considered to be in the macrohardness regime.) Hardness is

calculated by the load divided by the contact area between the indenter and the sample, which can be extrapolated from the lengths of the diagonals of the square (or diamond) indentation by the following equation [26]:

$$H_V = \frac{P \times 2\sin(136°/2)}{d^2} \approx \frac{1.854P}{d^2} \quad (1)$$

Where H_V is the Vickers hardness number, P is the load (kg or kg-f), and d is the average of both diagonals (mm). H_V is often given in units of kg/mm^2 and kg and kg-f are often used interchangeably, assuming acceleration due to gravity is 9.807 m/s^2. Though H_V is force divided by contact area, not projected area, and is therefore not equivalent to the pressure under the indent, it can be converted to Pa by multiplying by 9.807×10^6.

Vickers hardness is largely independent of load because the geometry of the indentation is the same regardless of scale, and theoretically and experimentally, H_V remains constant with load. But this trend breaks down when the load is too low. What load is "too low" depends on the hardness of the material, harder materials require higher loads to avoid this effect. As testing load decreases beyond a certain value, the apparent hardness value increases exponentially. This is called the indentation size effect and is more significant in brittle materials [44-45]. What is actually happening is that at low loads, the material responds elastically as the indenter load is applied, some plastic deformation occurs, but the area under and around the indent does not become completely saturated with deformation processes (dislocations, microcracks, etc.) and upon unloading the elastic deformation relaxes, leaving a smaller visible indentation. This is true of all hardness tests, but only becomes an issue when measuring microhardness. This error can be large,

increasing apparent hardness by >200 %, but decreases rapidly to an asymptotic value as load increases. Since no indenter is perfectly sharp, one might imagine a load so light that contact would be completely Hertzian, leaving no indent and therefore "infinite hardness." This asymptotic or "plateau hardness" value is the only reliable value and all reported microhardness values should be reported in this regime [45]. The indentation size effect is not insurmountable, else nanohardness testing would not be possible, but different methods are required to acquire reliable results.

Because the Vickers hardness test resolves most of the shortcomings of previous hardness tests, it can be applied consistently to most materials softer than diamond, and values calculated can be converted to (pseudo)stress, it is widely used in the scientific community. Again, it is called the Vickers hardness *number*, meaning that it is only a rating and should not be casually confused with a true materials property. As long as the indentation size effect is avoided (At least two loads should be used in any test to verify this) data from all materials below super-hardness, whether ceramic, ductile, single-crystal, or composite, can be readily compared. The only limit to the range of the Vickers hardness scale is the hardness of its indenter. With hard and super-hard materials, the indentation size effect becomes more significant and loads greater than 1 kg are often required. In addition, as materials approach the hardness of diamond, the elastic effects become greater as the elastic strain of both the target material and the diamond indenter become significant. This has generated much debate as to the validity of hardness data reported in the super-hard and most certainly ultra-hard ranges [40,44-46].

Previously, reports of composites and film hardnesses of 70-100 GPa were discussed without mention of the obvious problem of measuring in the ultra-hard regime with an indenter that is barely, if at all, harder than the material tested. Many question whether any harder-than-diamond materials have actually been discovered. These doubts are based upon the facts that experimental data must be produced with a diamond indenter and many other ultra-hardness claims are based on bulk modulus predictions alone [20,30-31,38-39,41]. As yet, there is no work-around to this problem, and so the approach is taken in the chapters of this dissertation is that claims of ultra-hardness will be taken with minimal skepticism as long as sufficient details of the measurement process are provided. Additionally, ample care must be taken to avoid residual stresses and the indentation size effect. Some also recommend that the indenter tip geometry be checked both before and after indentation [30,45].

1.4: Icosahedral Borides

B_4C and other compounds containing boron icosahedra have been shown to possess high hardness despite lower symmetry of their crystalline lattices. The light atoms, larger unit cells, and inefficient packing of boron icosahedra give many of these compounds lower densities than other hard materials. The bonding of the boron icosahedra is strongly covalent, with bonding occurring between three boron atoms in the center of each face of the icosahedra (Figure 1.1) [47-48]. The number of available bonding electrons in each B atom and the structure of the icosahedra cause the B lattices to be electron deficient, requiring cations to stabilize the structure. One of these structures based on boron icosahedra contains a family of 12 known compounds with an orthorhombic lattice and a

64-atom unit cell. They consist of a framework of 14 boron atoms with two sites (generally) occupied by metal atoms, hereafter referred to as the 1:1:14 structure. The lattices are of space group *Imam*, Pearson symbol oI64. All are known or suspected to have partial vacancy on at least one, and more commonly both, of the metal sites as shown in Table 1.2 [6-7,9-12]. For instance, in $AlMgB_{14}$ approximately 25% of the Al and Mg sites are vacant [9]. The combination of low symmetry and high vacancies makes this family of compounds unique in the world of hard materials. As with many borides, they have a higher coefficient of thermal expansion (CTE) than most ceramics. Polycrystalline $AlMgB_{14}$ samples were determined to have CTE of 9.45×10^{-6}/K [49]. The properties of such a complex lattice would be expected to be highly anisotropic, yet the hardness of a single crystal remains high for all orientations, varying between 24 and 30 GPa [4-5,50].

Table 1.2: Interstitial site occupancies for the $AlMgB_{14}$ family.

	Occupancy				Reference
	Site I - Large		Site II - Small		
$AlMgB_{14}$	Mg	78%	Al	75%	[9]
Mg_2B_{14}	Mg	93%	Mg	100%	[7]
Mg_2B_{14} *	Mg	97% *	Mg	97% *	This Study *
$LiAlB_{14}$	Li	100%	Al	96%	[6]
$NaBB_{14}$	Na	100%	B	80% **	[7]
$YAlB_{14}$	Y	62%	Al	71%	[10-11]
$TbAlB_{14}$	Tb	†	Al	†	[10] †
$DyAlB_{14}$	Dy	†	Al	†	[10] †
$HoAlB_{14}$	Ho	63%	Al	74%	[10]
$ErAlB_{14}$	Er	62%	Al	73%	[10-11]
$TmAlB_{14}$	Tm	57%	Al	62%	[12]
$YbAlB_{14}$	Yb	†	Al	†	[10] †
$LuAlB_{14}$	Lu	†	Al	†	[10] †

* X-ray pattern from polycrystalline sample (Chapter 3), all others from single crystals.
** B not located in Site II, occupies position 1.46 Å away from Na atom. [7].
† Occupancies not reported.

$AlMgB_{14}$ was initially reported to have a composition of $AlMg_{0.5}B_{14}$ in which the smaller site (Site II) was 75% occupied by Al and the larger site (Site I) was 50% occupied by Mg and 25% occupied by Al (total 75% occupancy) [8]. Higashi and Ito later reported a composition of $Al_{0.75}Mg_{0.78}B_{14}$, with no element mixing between the sites [9]. They conclude that the initial report was likely in error due to the similar scattering abilities of the Al and Mg atoms and chemical analysis results tainted by residual Al flux. Their conclusions are further justified by subsequent independent reports of similar arrangements in Al-RE (Rare Earth) borides [10-12].

Chapter 3 reports that the refinement of the Mg_2B_{14} structure resulted in less than 100% occupancy in both the large and small Mg sites. Guette, et al reported 100% occupancy in the smaller site, since this parameter was held constant during refinement, likely a consequence of available computational power at the time of discovery [7]. Though not explicitly mentioned, if occupancy parameters were also held constant in the refinement of $AlLiB_{14}$ and $NaBB_{14}$, there is a chance that the Li and Na sites are not truly fully occupied either. This would imply that there may be no 1:1:14 borides with fully occupied metal sites.

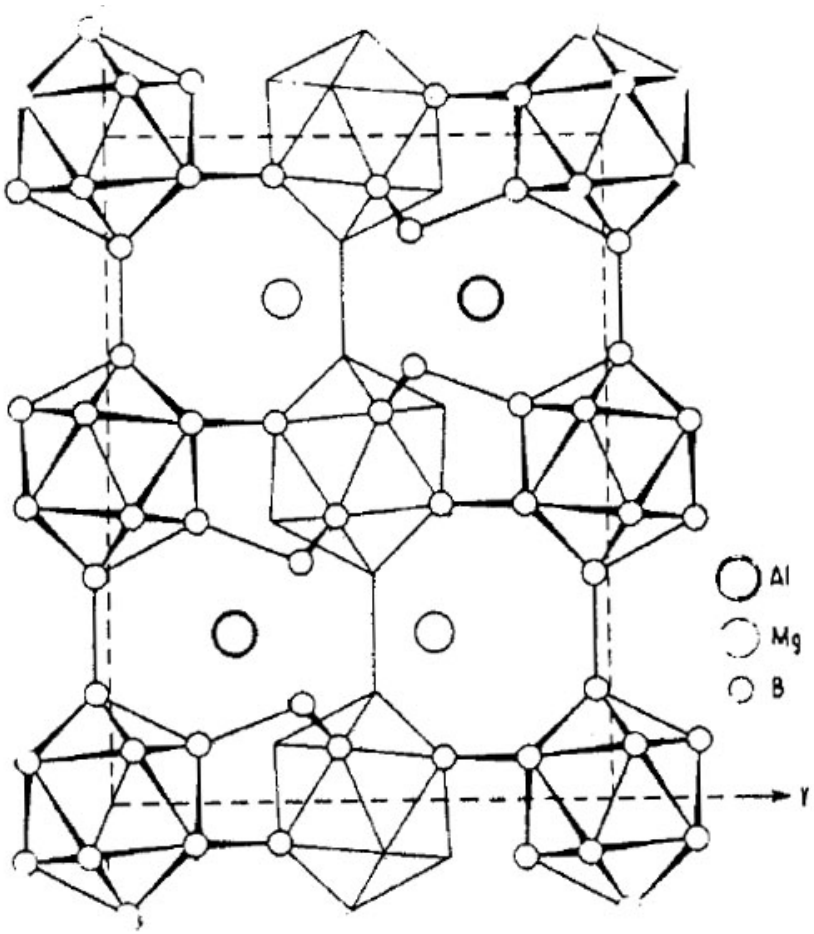

Figure 1.3: $AlMgB_{14}$ lattice diagram, *bc* projection from Werheit, et al [5]. Mg atoms on larger site (Site I) and Al atoms on smaller (Site II).

The interstitial sites I and II are caged by 16 and 12 neighboring boron atoms, respectively. Al, when present, occupies the smaller site, being a smaller ion than Mg. It appears in the above structures that one determining factor for low occupancy is the total electronic contribution from the interstitial atoms. Analysis of the valence of the metal atoms would suggest that for each pair of interstitial sites, an average of 4 electrons is donated to the B network [10-11]. Yet there are still vacancies in the structures with $^{+}4$ ion pairs such as Mg_2B_{14}. Analysis of electron density by Higashi has shown that the actual contribution to the network may be between 2 and 3 electrons per site pair [6,51].

This would mean that the interstitial atoms are not all fully ionized and would explain why there exist vacancies in all of the structures. If occupancy is governed by charge density, it furthers the possibility that both sites in $AlLiB_{14}$ and $NaBB_{14}$ may contain vacancies. Charge density analysis from diffraction of $LiAlB_{14}$ crystals showed that the bonds between the boron lattice and the metal atoms are mainly ionic [47]. Additionally, only some of the charge from each metal ion was donated to the boron structure, and the average charge of each ion was $Li^{0.7+}$ and $Al^{1.5+}$.

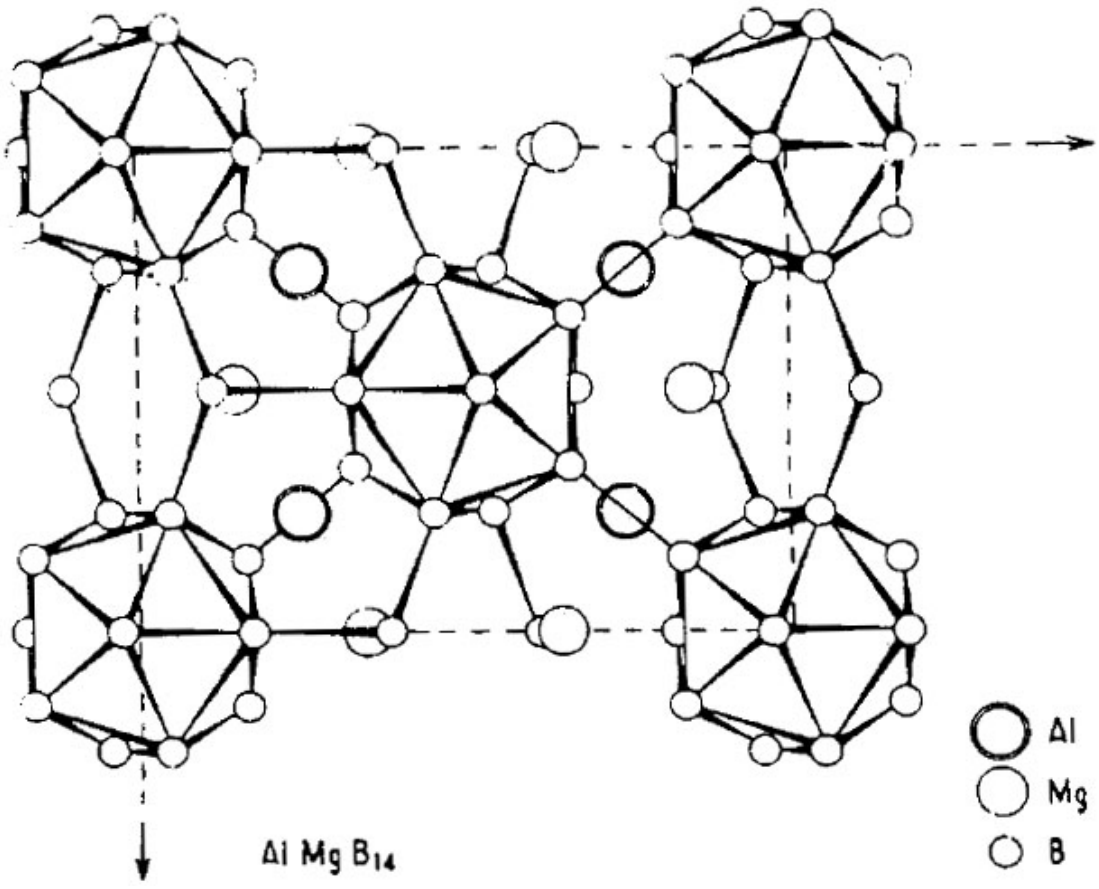

Figure 1.4: $AlMgB_{14}$ lattice diagram, *ab* projection from Werheit, et al [5].

Occupancy and size of the interstitial metal atoms combine to affect the lattice parameters by straining the surrounding B scaffold. This not only changes the lattice dimensions, but also causes minor changes in the orientation of the B icosahedra [5]. Note in Figures 1.3 and 1.4 above that the B icosahedra are not aligned on any major axis. This allows for variation of bond angles and distances with lattice parameter changes caused by the intersitial atoms.

Korsukova, et al show a linear relationship between each lattice parameter and the ionic radii of trivalent rare earth interstitials [10]. Figure 1.5 shows these results along with those for Li, Mg, Tm, and Y Site I substitutions. The lines in Figure 1.5 show the trend in lattice parameters *b* and *c* due to the size of the trivalent ions. Lattice parameters *b* and *c* both increase along with ionic radius, while the trend in *a* is less clear. There is a discontinuity at Yb which they claim may indicate a combination of valence states, Yb^{2+} is the more common and larger ion, which could account for the increase in lattice parameters [10]. There is also a smaller discontinuity at Tb, which may be due to a combination of +3 and +4 oxidation states, causing an overall decrease in the size of the unit cell. While Lu follows the trend of the trivalent ions with respect to lattice parameters *b* and *c*, there is a significant increase in lattice parameter *a*. The cause for this is unknown, but this higher degree of distortion could have a significant effect on the strength of this lattice.

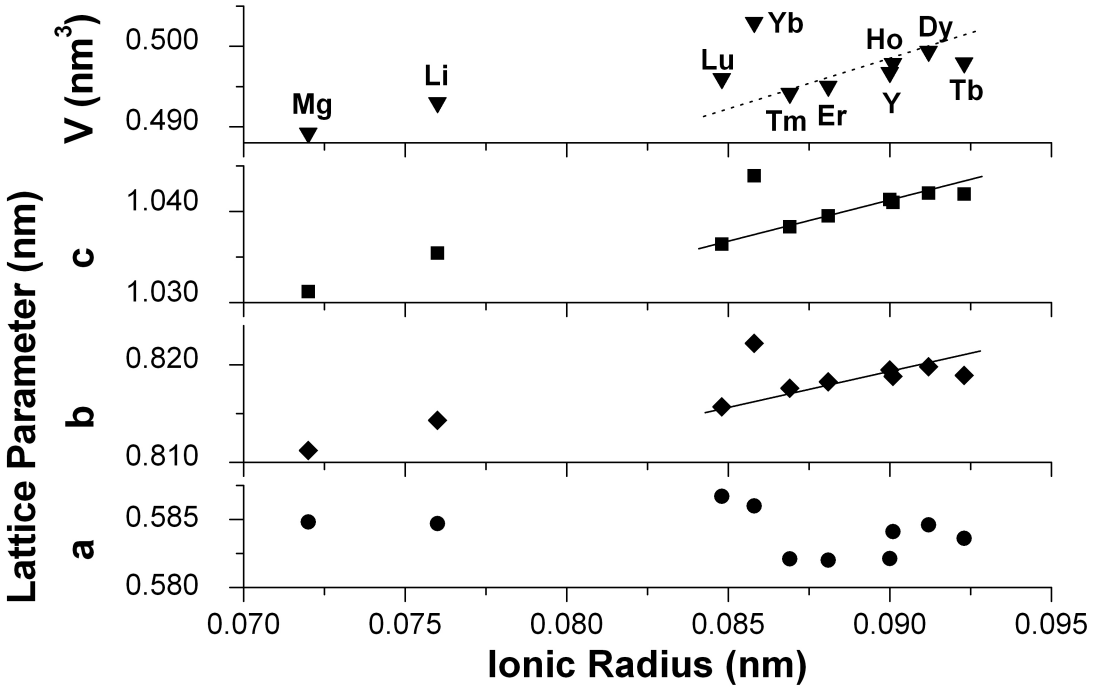

Figure 1.5: 1:1:14 lattice parameters vs ionc radii. Lattice parameter data from Higashi and Ito [6,9] for Al(Mg,Li)B_{14} and from Korsukova, et al [10-12] for Al(RE)B_{14}. Ionic radii from Shannon and Prewitt, and Barbalace [52-53].

The occupancies of the metal sites were not determined for most of the Al(RE)B_{14} compounds. So it is uncertain if the trends in ionic radius and lattice parameters are accompanied by a discontinuity in Yb or Tb occupancy; also, charge, occupancy, and ionic radius of Site I atoms may also affect the occupancy of Al on Site II. Since angle and distance can have a significant effect on a bond's strength, hardness and other properties should fluctuate as a function of occupancy and ionic radii. Hardness has only been reported for a few 1:1:14 crystals. Vickers microhardness with indentation perpendicular to the (001) plane has produced average values of 29.2 and 27.8 GPa for $AlLiB_{14}$ and $AlMgB_{14}$, respectively [4,50]. Further testing may be necessary to determine how statistically significant this difference is, and should include a variety of 1:1:14 compounds.

Although there have been no reported discoveries of additional compounds isostructural to $AlMgB_{14}$ since 1992, others may yet exist [11-12]. All the above compounds contain light and rare earth metal atoms, but no combinations involving transition metals have yet been found. There have also been no reports of solubilty between these phases, i.e. $Al_{1-x}Mg_{1+x}B_{14}$ or Al(Y-Er)B_{14}. Since Mg is known to be able to occupy both sites and the larger site can accommodate many rare earth elements, such combinations seem possible. Since the two metal sites appear to be strictly ordered by element, it begs the question as to the arrangement of the vacancies as well. If the vacancies are ordered there may be an ordered-disordered transition that could affect various properties of the compounds. All of these questions are intriguing and probably significantly affect the properties of these materials. Better understanding may allow "tweaking" of the lattice in order to optimize the strength of the bonding in the B framework.

1.5: Transition Metal Diborides

The metal diborides of space group *P6/mmm* (Pearson symbol hP3) have hardnesses that fall between oxide ceramics and super-hard materials [54]. Like many hard materials, they are quite refractory, yet unlike many ceramics, they have high thermal and electrical conductivities. In fact, the electrical conductivity of Ti metal is lower than that of its diboride [55-56]. Some of these, especially TiB_2, also have considerable resistance to various forms of corrosion including attack from oxidation, liquid metals, and acids [55,57-58]. Since these diborides have the same crystal structure, many of these compounds also have complete solid solubility with each other [54,59-60]. With at least 27 known diborides, this can allow for a multitude of combinations of properties [55]. If

composites of these materials are desired for strengthening, some combinations have smaller solubility ranges and/or sluggish solutionizing rates that can be exploited to produce spinodal decomposition microstructures and multi-phase ceramics [54,61-62].

The major drawback to engineering use of these materials is their refractory nature, which makes fabrication of high-density parts quite difficult and expensive. TiB_2 is of particular interest because it excels in all the aforementioned properties and has reasonable toughness. TiB_2 is a common specialty ceramic for many applications. Diffusion studies of B isotopes in TiB_2 have shown it to have low self-diffusivity of B atoms, even when near its melting temperature of 3225ºC [58]. This is evidence of the strong covalent bonds present and explains the difficulty of sintering this material. Densification of TiB_2 is discussed further in Chapter 6, but in summary the extreme temperatures required push the limits of methods such as uni-axial hot pressing, hot isostatic pressing, etc. Significant amounts of metallic binders, nitrides, and/or carbides are typically used as sintering aids [63-68]. While these additions decrease porosity, they are largely detrimental to mechanical properties compared to monolithic TiB_2. Metallic binders are particularly troublesome. Whether added for liquid or solid state sintering, most metals will react to form a number of different borides with lower strength and hardness than TiB_2; also, reaction of the binder eliminates the possibility of a ductile, toughening phase [65-68].

TiB_2 has also been selected as a reinforcement phase in $AlMgB_{14}$ composites due to its exceptional strength and hardness, and this use is discussed in more detail in Chapters 1.8 and 5 [3,14,24,69-70].

1.6: Mechanical Alloying

The super- and ultra-hard composites discussed in Chapter 1.3 have all been produced by various thin-film deposition techniques. Such methods can be suitable for coating technologies, but have so far been largely limited to research activity rather than commercial utilization. A wider variety of potential applications for hard and wear-resistant materials require bulk materials. The nanosized microstructures produced in thin films are difficult to reproduce in bulk materials.

For ductile composites, extreme plastic processing such as extrusion can result in very fine microstructures with enhanced hardness and rigidity. Yet this is entirely unsuitable for brittle materials. Fine microstructures in bulk ceramic materials generally must arise from the consolidation of fine ceramic powders. The major difficulty is in preserving fine crystallites during densification, as sintering and grain growth often occur simultaneously. For this reason pressure is sometimes applied during sintering, to achieve maximum density at the lowest temperature and in the shortest time possible. Pinning grain boundaries is another effective method of slowing grain growth. This is usually done with very fine particles that are more refractory than the matrix. In producing hard, nanoscale composites, the addition of an even finer and more refractory phase becomes

less feasible. But grain growth can be inhibitied in a similar fashion by using two or more immiscible phases, as with many of the films mentioned in Chapter 1.3 [32,39].

Milling is frequently used to reduce particle sizes of ceramic powders. Milling can take many different forms, and these forms have a great effect on the average particle size and properties of the resulting powder. Conventional milling includes such machines as tumbler, planetary, and attritor mills. These types of mills involve rolling or stirring media among loose powders. The major action against the powder particles is from rolling and sliding of the media, shearing and fracturing brittle crystallites. The limit to the reduction in particle size is generally related to the energy of the mill, or the energy transferred to the powder from the media. As most impacts are from sliding and rolling, the energy is limited, and these types of milling are referred to as low-energy milling [71]. Schwarz has shown through modelling that due to the inefficency of energy transfer, these types of mills are generally not capable of inducing significant amounts of plastic deformation in many materials [72]. Action that only reduces particle size, and causes little deformation or strain, is called mechanical milling (MM).

Higher energy can be delivered by impact between media, as occurs in shaker or vibratory mills, than by rolling impact. Attritor mills are sometimes designed to impart such high velocity on the media that collision impacts can occur (thus increasing the rate of comminution), but the media and impellers can suffer significant wear and damage in the process [71,73]. Yet higher energy does not necessarily mean smaller particle size. In most high-energy milling processes, there is a size limit where larger particles fracture

while finer particles tend to cold weld or deform together on impact [71-72,74]. While high-energy milling does not always produce finer powder, it can induce much higher plastic strain. This can lead to some interesting effects. First, deformation can be so high as to produce amorphous material [71-72,74,75]. If different elements or compounds are combined in such a fashion, they can be intermixed on the atomic level. This is the main concept behind mechanical alloying (MA). Constituent materials are "mashed" together, the layers folded and thinned until the lammelar spacing becomes indistinguishable (Figure 1.6) [74,76-77]. New compounds can be created by subsequent heating of the powders, during hot-pressing, or even during the milling itself. Amorphous phases can remain during consolidation of the powders, as can other metastable phases such as non-stoichiometric or super-saturated solid solutions [71,75].

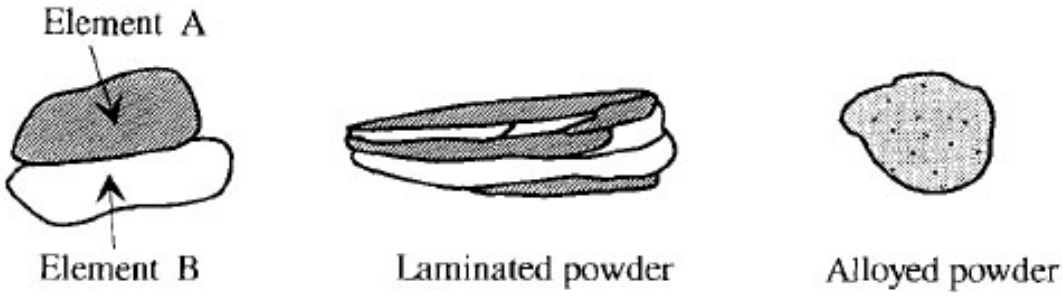

Figure 1.6: Progression of comminution during typical MA, from Lü [77].

If the energy of formation of a new compound is high enough, the reaction can occur energetically and quickly throughout the powder mixture by a self-heating synthesis (SHS) reaction. SHS reactions induced by MA are called mechanically-induced self-propagating reactions (MSR) [78-80]. Many metal diborides and mixed metal diborides can be formed by MSR . Ti + B is a well known example that readily undergoes

transformation by MSR due to the high energy of formation of TiB_2 [81-83]. The mechanism behind the initiation of an MSR is that the activity of the powders increases with the level of deformation and intermixing. When the majority of the powders are deformed to a certain point, the heat of an impact ignites the reaction, and it proceeds rapidly throughout the powder in the chamber, usually in less than one second [82,84].

The high level of deformation induced by MA can also be used to produce an intimate mixing of immiscible phases without a reaction [74]. This can help preserve the often nanoscale grains during sintering. Nanocrystalline $TiN/TiB_2/Ti_xSi_y$ powders have recently been produced by ball milling, similar in structure to and approaching the scale of Veprek's thin films, though they were not consolidated into bulk articles [19,85]. If such mixtures of immiscible phases were amorphized into metastable solutions, spinodal decompositions could produce fine microstructures on consolidation.

Mixing is a frequent problem in all forms of powder processing. Thorough mixing can be impeded by the tendency of powders to segregate by size, density, morphology, surface properties, etc. during handling. Nanoscale powders have a greater tendency to agglomerate, since the ratio of interparticle van der Waals forces to particle mass is much greater in nanoscale powders. The greater particle surface area in finer powders makes agglomerates held by such forces stronger and harder to break down. The mixing produced by MA is at a much finer scale and often more evenly mixed than powders produced by MM. MM powders of different phases are difficult to mix and often

agglomerate and segregate, even when milled together. MA powders can still agglomerate, but since the constituients are intimately mixed, they cannot segregate.

Three types of mills were used in the studies on $AlMgB_{14}$ composites reported in Chapters 4-6. Due to the high affinity of fine powders for O, all the mills used were capable of milling under inert atmosphere. The first, a Fritsch P5 planetary mill, is typical of mills of its type. Rolling impact reduces particle size with moderate deformation. Due to the low energy, it also produces the least contamination from wear of the media and milling chamber. The second, and most commonly used in these studies, is a Spex 8000 mixer/mill. It is termed a vibratory/oscillatory mill because the milling vial travels rapidly along a "figure-eight" path designed to induce more random collisions and eliminate dead spots within the vial. It is also among the highest energy ball mills, producing estimated media speeds of 6-18 m/s which are more than sufficient for most MA experiments, and thus it is a popular mill in research [71,86-87]. The major drawbacks of the Spex 8000 are the considerable wear rate of media and the small sample size of ~2 cm^3 (suitable for laboratory experiments but inadequate for commercial use) . The third type of mill is designed to produce the comminution rates of a Spex 8000 mill in much larger batch sizes of ~500 cm^3 of powder. This mill, a Zoz CM01 Simoloyer, is a high-speed attritor mill that stirs media at speeds up to 12 m/s [73]. As mentioned earlier, contamination of the powder from wear debris is quite high, as the impellers sustain heavy damage from stirring the media at high velocities. Although the Fe content of powder from the Zoz mill is considerably higher than that from the Spex mill, the comminution rates are similar, as discussed in Chapter 7.1.

1.7: Wear

Hardness is commonly considered to be among the most important of materials properties and is thus often considered in engineering applications. However, there are few instances where hardness is the sole factor or even the most important factor in materials selection. When hardness is important, it is often in applications involving wear, and is by no means the only aspect to consider. Wear can still occur when the incident material is softer than the target, and hardness does not determine the mechanisms of failure. Impact or concentrated stress can easily cause strong, but brittle, ceramics to fail. Yet if enough energy is absorbed through a toughening mechanism, failure can be prevented or minimized.

Erosion.

Abrasive and erosive wear are similar concepts, both governed by a material's hardness and toughness, but with subtle differences. In abrasive wear, hardness determines a material's resistance to penetration by the abrasive and toughness determines the energy absorbed in removing material. In most abrasive situations, such as polishing, the abrasive particle is held against the material with presumably constant force, the penetration depth is determined by the hardness of the material, and material is swept away by movement of the penetrating particle. As the abrasive particle is typically entrained on a moving substrate, energy dissipation has little to do with the material removal rate unless the motion of the substrate is thus slowed appreciably. This does not mean that toughness has no effect on abrasion resistance as it affects crack propagation and the depth of sub-surface damage. But in abrasive wear, hardness is the dominant

property and is why the relative hardness of abrasive media must be much higher than that of the target material to efficiently remove material.

The situation is reversed in many ways during erosive wear. Erosion differs from abrasion in that the erosive particles impact the specimen with a certain energy, opposed to an abrasive particle which is under constant load. Each impact event has an amount of energy that must be dissipated and relative hardness determines, in part, how much energy is absorbed respectively by the erodent and the target, and so erosive particles need not be harder than the target to cause noticeable wear. The toughness of the target material affects how much damage the proportion of the energy absorbed by the target causes. The tougher a material, the less deeply penetrating cracks will be. For materials that fail largely by fracture, sub-surface lateral cracks are the most serious, as they cause material to delaminate from the surface. Theoretical calculations based on lateral crack formation and empirical data have shown that for brittle materials, material removal is inversely proportional to both hardness and toughness as follows [88-89]:

$$V \propto \frac{P_i^{11/16}}{K_{IC}^{4/3} H^{1/2}} \qquad (2)$$

Where V is the volume of material removed, P_i is the impulsive load, K_{1c} is the fracture toughness, and H is the hardness. Therefore, erosion rates decrease more rapidly with increasing toughness than with hardness. The relationship is usually multiplied by a factor, ω, the wear coefficient, that is dependent on the system and usually determined experimentally. Since V is the volume per impact, a number of impacts, N·V, would equal the total material removed, and divided by time, N·V/t, would equal the erosion rate

[88]. The mass and velocity of a particle determine the impact energy, and impulsive load, so erosion rates are typically reported as volume of material removed per mass of erodent, along with the average particle velocity during testing. The morphology of the erodent is also important, round particles cause the least damage and angular particles are the most aggressive erodents, this factor is included in the wear coefficient term.

Impact angle is another significant factor. For brittle materials (as described above) erosive wear is highest at impact normal to the surface and drops quickly as impact angle becomes more glancing [90-92]. Erosion rates are highest at 90º because the impact loading and unloading causes lateral cracks to form below the surface (as modeled by Equation (2)) and the force perpendicular to the material surface is highest at 90º, so the failure stress also reaches deepest into the material at this angle. For ductile materials, erosion is highest at an angle around 30º from the surface and drops to a moderate value at 90º impact [90,92]. At normal impact, a ductile material will generally plastically deform heavily, work-hardnening until fracture initiates, absorbing significant energy in the process. Glancing impact of rounded particles causes ductile material to pile up until these asperities shear off. Angular particles at low angles of impact tend to plow away material immediately. In either case, the removed material has not fully deformed and absorbs less energy. Materials with intermediate behavior such as Co-bonded WC composites, show maximum erosion at angles less than 90º depending on the amount of ductile binder.

Reinforcement.

In addition to inhibiting dislocation motion and improving hardness in nanoscale composites, reinforcement phases are more commonly used to increase strength and toughness. The wrong combination of phases and microstructures can be detrimental to the performance of a composite, so care must be taken in selection and design of these. Strength and toughness are increased in ceramic composites through mechanisms such as crack deflection and crack blunting. Residual stresses are common in multi-phase composites, because of CTE mismatch resulting in differential strains upon cooling from the forming temperature [93-94]. Residual stresses that are too high can seriously degrade the properties of a ceramic by causing spontaneous cracking, similar to that caused by thermal shock but having little dependence on cooling rate. Minor residual stresses can be advantageous with a proper microstructure. Since brittle materials fail perpendicular to the direction of maximum tension, an advancing crack can be deflected by these local stress fields. As the path length of a crack increases, the surface area of fracture also increases, and the amount of energy absorbed goes up. Pre-existing microcracks can deflect a crack by directly interacting with the crack or by changing the stress concentration in the vicinity of the crack front [94]. Crack splitting is also possible, which can further increase the fracture area. However, the surface of a pre-existing microcrack does not add to the energy-absorbing surface area of the fracture surface, and therefore too many microcracks can be detrimental. A crack can also be deflected by reinforcement particles, taking a longer fracture path along the boundaries between phases. Too weak an interface will provide no increase to, or even decrease, energy absorption. Too strong an interface will cause the reinforcement particle itself to

fracture. For a high strength or high modulus reinforcement, this can be beneficial as well. This situation can lead to crack tip bridging, a method of crack blunting [93-95].

Crack blunting is largely a strengthening mechanism and occurs when propagation of a crack is impeded by changes in stress concentration, distribution, or orientation. An advancing crack is typically atomically sharp and therefore has maximum stress concentration at the tip. An advancing crack tip opening into a pore can be blunted by the sudden decrease in stress concentration, but porosity has many detrimental effects on hardness, modulus, etc. and pores often act as stress concentrators and crack initiation sites. As a result, porosity is often avoided in strong materials. A more favorable situation would be for a crack to advance upon a reinforcement particle. To pass around the particle (whether through the matrix or the interface), the crack must change its orientation to the tensile stress causing failure [93-94]. As this angle changes, the crack opening stress decreases, resulting in partial blunting of the tip. If the crack were to pass through the particle, the difference in moduli of the reinforcement and matrix cause the local stresses to be redistributed. The higher modulus phase limits strain in the other, effectively lowering the stress concentration at the tip. If the particle and interface are strong enough, this generally leads to the crack propagating around the particle through the matrix. When the crack front meets on the other side of the particle, the stress at the tip is reduced. Stress that was concentrated solely on the advancing crack front is now distributed between the crack front and the intact particle in its wake, “bridging” the crack [93-95].

Another effective method of increasing toughness and blunting cracks is by formation of a process zone [93-94,96]. Residual stress around a reinforcement particle that alone is not high enough to cause the formation of microcracks can interact with the stress concentration field around an approaching crack tip. When the sum of these fields becomes greater than the failure stress of the matrix, microcracks can spontaneously form, as shown in Figure 1.7. Proper residual stress levels will cause these microcracks to form well ahead of the crack tip. The formation of the microcracks absorbs energy, adding toughness, and their existence redistributes stress, blunting the crack and strengthening the ceramic. Effectively, the damaged region has a lower elastic modulus, and the surrounding higher modulus material shares a higher fraction of the stress. These properties make a process zone very similar to a plastic zone ahead of a crack in a ductile material [94].

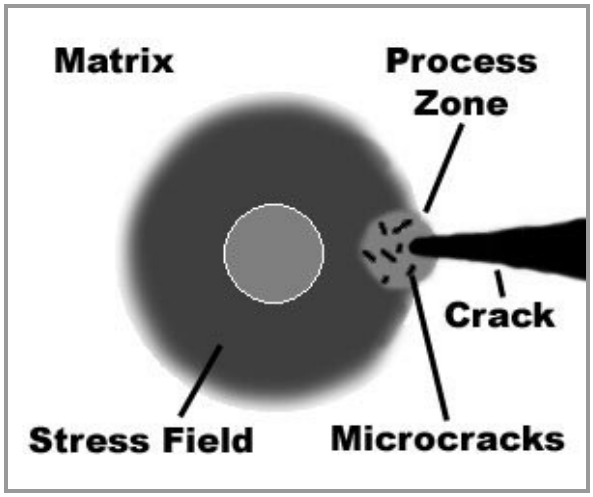

Figure 1.7: Residual stress in a ceramic matrix composite leading to formation of a process zone.

Increased toughness can have little or no effect on wear resistance though, if the scale of wear mechanisms are smaller than that of the reinforcement fibers. Erosive wear is

equivalent to multiple fracture events on a small scale. Thus a material designed to resist wear must possess strengthening mechanisms of a smaller scale than the failure events. If the scale of the microstructure is too large, the matrix and reinforcement phases will fail independently of one another.

To design a composite resistant to erosion, with impact diameters typically tens of microns across, the microstructure must be of a much finer scale for strengthening and toughening mechanisms to function. This limits such composites to sub-micron and nanoscale microstructures. Li, et al have used dynamic modeling to study the particle erosion of composites. Their results predicted that finer reinforcement particles are more effective against erosion, specifically when the reinforcement is of a much smaller scale than the erodent [97]. Also, a distribution of reinforcement sizes was typically superior to a single size, which is fortuitous since a distribution of sizes can be more easily achieved in real materials [98].

Palmqvist Toughness.

Toughness of brittle ceramics can be estimated using the Palmqvist method as follows [99-100]:

$$K_{IC} = 0.016\left(\frac{E}{H}\right)^{1/2}\left(\frac{P}{C^{3/2}}\right) \tag{3}$$

In the above equation, E is the elastic modulus, H is the Vickers hardness (kg/mm^2), P is the applied load (N), and C is half the average length (μm) of the cracks radiating from the corners of the Vickers indent, from tip to tip. The constant, 0.016, is a materials

constant which has been found experimentally for many materials to be approximately 0.016 [99]. This type of measurement provides only an estimation of the toughness of a material. Accurate toughness values must be measured by large scale fracture of an entire specimen. This usually requires samples of a minimum size, certainly larger than thin-film materials and also larger than those easily produced in the following experiments. Still, the Palmqvist equation can be used to generate consistent, reliable data if adequate care is taken during measurement. The Palmqvist cracks have been found to form upon unloading for most materials, and thus arise from residual stress due to the plastic zone remaining after indentation [88]. The size of the plastic zone and the intensity of the residual stresses can be calculated for most materials with regular behavior with knowledge of the indentation parameters and the elastic modulus of the material.

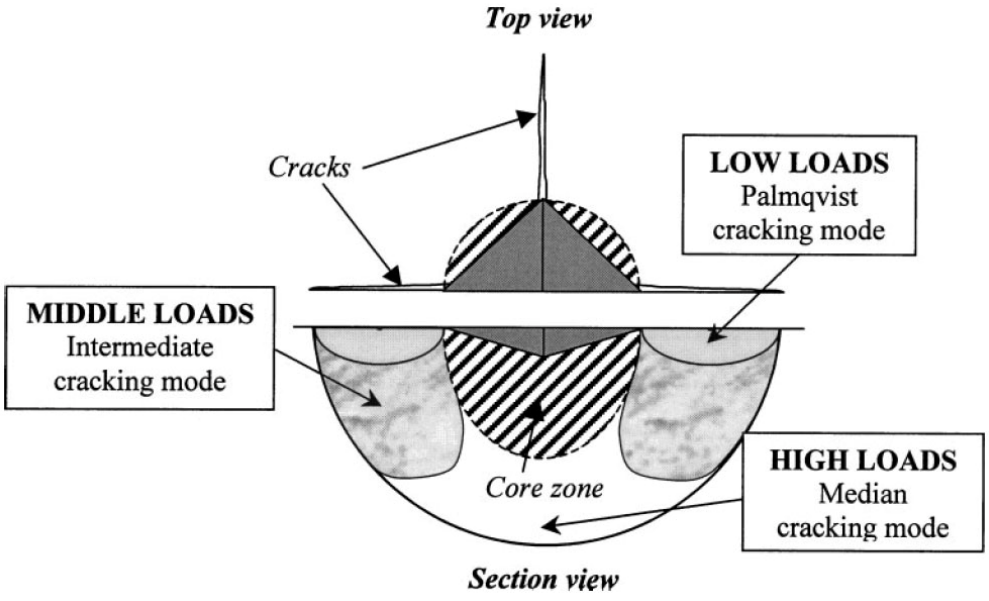

Figure 1.8: Diagram of variations of indentation cracking, “High Loads” indicates half-penny crack and “Low Loads” indicates true Palmqvist cracks. From Chicot, et al [100].

A serious down-side to the Palmqvist method is that there are two major crack morphologies that can result from indentation, one resulting from “high” loads, the other from “low” loads (which depends on the material), and each with a different form of the Palmqvist equation [100]. Diagrams of each are shown in Figure 1.8. The crack morphology cannot be determined from the surface of the sample. The only way to determine the mode of crack formation, without fracturing the sample, is to plot both forms of the equation over varying loads and find the crossing point. Equation (3) is the form for median, or half-penny cracks that form two full hemi-circles below the indentation, each parallel to a diagonal of the indentation. These cracks typically develop at higher loads. Equation (4) below is the form for true “Palmqvist” cracks, which consist of four separate, semi-elliptical cracks that project outward from the tips of the indent diagonals. These cracks do not propagate below the indent and appear only at lower loads [100].

$$K_{IC} \propto \left(\frac{E}{H}\right)^{1/2}\left(\frac{P}{al^{3/2}}\right) \qquad (4)$$

In the above equation, a and l are components of C in Equation (3), a is half the average indent diagonal and l is equal to the average crack length, measured from the indent to the crack tip. A further complication arises at intermediate loads. Palmqvist cracks initiated under higher and higher loads begin to grow underneath the indentation until they meet in the middle and form a half-penny shaped crack, now in the high-load regime. This progression is shown in Figure 1.8. Intermediate cracks produce invalid results and occur at a range of loads between “high” and “low.” Measurement of indentation cracks at loads in this intermediate region will not give a clear picture as to

the limits of the “high” and “low” load regimes, exploratory testing at indentation loads well into each regime are necessary to determine a minimum or maximum “safe” load.

The transition of the indentation crack modes and the onset of the indentation size effect do not necessarily correspond to one another. For consistent results with the Palmqvist-style cracks, or low-load cracks, this “low” load must still be sufficiently high to avoid the indentation size effect. If the indentation size effect interferes with Palmqvist-type crack measurements, a higher load that would cause half-penny type cracking could be used.

Toughness measurements of brittle materials by large scale fracture are particularly susceptible to critical-sized flaws which can drastically reduce the energy absorbed during failure. Wear resistance is only affected by such flaws locally, unless the concentration of flaws is significant, overall wear resistance will not be severely affected. As mentioned earlier, erosion is dependent on both the toughness and the scale of the microstructure. A large grained, fiber-reinforced ceramic composite can have a high toughness measured by large-scale fracture, but would have no more wear resistance than its constituent materials. Toughness estimated by indentation cracks may be a better representation with respect to wear, as the size of microhardness indentations and erosive impacts are of similar magnitudes.

1.8: Past Work

As mentioned in Chapter 1.4, the 1:1:14 borides were first studied decades ago, and the early research focused on the crystallography of these compounds. There was little interest in their hardness until Cook, et al reported an $AlMgB_{14}$ - 30 wt% TiB_2 composite with hardness up to 46 GPa [3]. Hardness of 1:1:14 single crystals were reported previously, approaching 30 GPa, but were largely forgotten by the hard materials community until this more recent discovery [4,50]. Polycrystalline $AlMgB_{14}$ produced from MA powder showed hardess greater than 30 GPa. The addition of a small amount of Si resulted in slightly higher hardness, and the addition of TiB_2 showed the most significant increase to over 40 GPa [3,24]. Both Si and TiB_2 were added to increase the electrical conductivity of the composites, but the increase in hardness was the most noticeable effect. If Si atoms could substitute into the $AlMgB_{14}$ lattice, changing electronic states and vacancies, it was theorized that it could have a significant effect on the bonding of the metal atoms in the lattice [24-25]. It is uncertain if the addition of Si caused any modification to the $AlMgB_{14}$ lattice, and it may have acted mostly as an oxygen getter. At present the role of Si additions to 1:1:14 compounds remains unclear.

The 30 to 40+ GPa hardnesses reported are especially noteworthy when one considers the amount of impurities and porosity in these materials. The starting powders for these specimens were produced by high-energy ball milling in steel vials with steel media, and this introduced significant amounts of Fe into the powders. O is also present in these materials, originating from the starting materials, especially the B powder. EDS and XRD analysis has identified the majority impurity phases as FeB, Fe_3O_4 and Al_2MgO_4

(spinel) [101]. All of these phases are significantly softer than $AlMgB_{14}$ and TiB_2. In addition, SEM analysis indicates that they bond poorly to the matrix and are the source of significant flaws. For most samples, porosity ranges from 1-4 % which can significantly degrade mechanical properties. Initial estimates of total impurity phases ranged anywhere from 5 to 30 vol % [101]. Due to the ease of absorption of low energy X-rays, there is considerable uncertainty in any EDS analysis of light elements (B-rich compounds and O) in these materials. Since the bulk material is mostly B, other element concentrations are also misrepresented as the heavy element signals cannot be compared to an accurate representation of the bulk, thus contributing to significant error in these estimates.

Various $AlMgB_{14}$ composites were produced with reinforcement phases other than TiB_2. These included TiC, AlN, and hBN [14]. TiC was selected because of its high hardness and refractory nature. Also, like Si additions, if Ti were to substitute into the $AlMgB_{14}$ lattice, it could change the band structure and possibly alter hardness [14,25]. AlN is used in as a sintering aid in many boride, nitride, and carbide ceramics and in addition is known to getter impurities, especially O, during sintering. Mechanical alloying of hBN can produce amorphous material, and the possibility of producing an amorphous boundary phase, similar to that in Veprek's work, was investigated [19,74-75]. The highest-quality TiC samples did not show notable differences in properties to those of the baseline $AlMgB_{14}$. For other samples there was considerable scatter in mechanical properties and density. TiC did appear to help refine the grain size of $AlMgB_{14}$, as it does in TiB_2 sintering [14,102]. AlN and hBN additions produced less favorable results.

High porosity, and possibly undesirable side reactions, were present in these samples. This and subsequent results indicate that nitrides, and to some degree carbides, can react unfavorably in $AlMgB_{14}$ composites and consume the 1:1:14 boride.

Additions of stabilized zirconia were made to $AlMgB_{14}$ in the hope of improving fracture toughness by the transformation toughening mechanism. This quickly proved unfeasible, however, as ZrO_2 reacts readily with the boride at sintering temperatures to produce a porous mixture of spinel and ZrB_2. This was due to the high thermodynamic stability of the transition metal dibordes and spinel. TiB_2, one of the most stable diborides, is relatively compatible with ZrO_2 and many transformation toughened TiB_2 composites have been prepared [103-105]. It may be possible that a high concentration of TiB_2 in an $AlMgB_{14}$ - ZrO_2 composite could slow the reaction to an acceptable rate to allow for sintering.

Since TiB_2 additions were found to improve mechanical properties, composites with higher concentrations were prepared. Both hardness and toughness were found to follow a greater-than-rule-of-mixtures relationship in $AlMgB_{14}$-TiB_2 composites when compared to single-phase $AlMgB_{14}$ and single-phase TiB_2. Unexpectedly, 100% TiB_2 prepared by high-energy milling in a similar fashion to $AlMgB_{14}$ was found to be readily sinterable at 1400ºC. A more detailed description of this research is provided in Chapters 5 and 6, but some related points of interest are presented in the following paragraphs.

The samples described in Chapters 4 and 5 were produced with more refined techniques than the first boride composites, resulting in reduced porosity, impurity concentration, and grain size. However, measured hardness values were actually somewhat lower than those reported initially for some of the first composites produced [3]. Average values for recent baseline ($AlMgB_{14}$ without TiB_2 additions) materials are around 28 GPa (vs. 33 GPa initially), 33 GPa for 30 wt% TiB_2 composites (vs. 42 GPa previously), and the hardest composites, 70 wt% TiB_2, averaged 37 GPa [70]. Due to the high hardness of all of these composites, Vickers microhardness indentations at 1 kg load (the maximum load for typical microhardness testers) are between 20-25 μm across, and are thus difficult to measure optically with consistent reproducibility. Erroneous indent measurements can skew hardness data to higher values as hardness is inversely proportional to the square of the indent diagonals. Additionally, Lewis reported that 1 kg load should be sufficent to avoid the indentation size effect for baseline and 30 wt% TiB_2 samples [14]. As can be seen from Figure 1.9, hardness for these samples barely reaches the aysmptotic region of the curve, likely putting higher quality and higher hardness samples farther into the exponential region and requiring that valid hardness measurements be taken at higher load. Higher indentation loads would also produce large indents, which would help alleviate deviation in results due to the difficulty of measuring small indents optically.

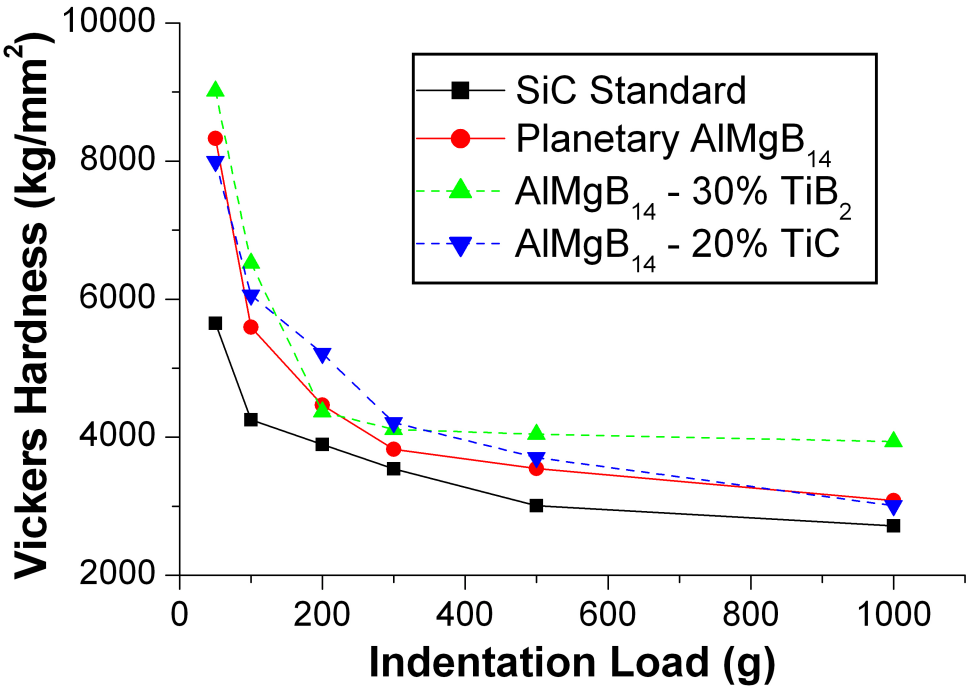

Figure 1.9: Indentation size effect on Vickers hardness of four materials from 50 to 1000 g load from Lewis [14].

Ahmed, et al examined the full range of $AlMgB_{14}$ - TiB_2 composites, studying their wear performance during scratching, abrasion, and high-speed machining [69-70]. All tests showed the best performance at a composition of $AlMgB_{14}$ - 70 wt% TiB_2, a composition that is nominally equivalent to $AlMgB_{14}$ - 59 vol% TiB_2. Scratch testing with a diamond indenter showed the composites to be superior to SiC and WC/Co tool pieces, and composites with 70 wt% TiB_2 approached the scratch resistance of commerical cBN [69]. This agrees well with respective hardness values of the materials, but the fracture modes are also of interest. In the 70 wt% TiB_2 composites, there was evidence of plastic deformation and transgranular fracture, while cBN appeared to fracture heavily along grain boundaries, with frequent grain ejection. This may indicate higher toughness in the $AlMgB_{14}$ - 70 wt% TiB_2 composites, which is supported by the abrasion and machining

tests. In wet diamond belt abrasion tests, the $AlMgB_{14}$ - 70 wt% TiB_2 composite performed as well as, and sometimes better, than cBN, depending on load and belt speed [70]. Perhaps more noteworthy was the superior performance of the 70 wt% TiB_2 composite versus WC/Co and cBN during dry high-speed machining of a Ti-6Al-4V alloy. Both crater and nose wear were lower with the $AlMgB_{14}$ composite due to a combination of hardness, toughness, and corrosion resistance [70]. Reduced crater wear is a good indicator of corrosion resistance, as it is wear due to hot (and reactive) Ti chips bonding and being torn away repeatedly from the top surface of the cutting tool.

Diffusion couples of Ti and Ti alloys paired with baseline $AlMgB_{14}$ corroborate the cutting tests as well. These tests lasted 120 hours at 1000ºC. Compared to similar diffusion couples with Ti and WC/Co, the $AlMgB_{14}$ couples had less than half the thickness of reaction product, consisting of a TiB and TiB_2 layer, while the thicker WC reaction product had four diffusion layers [106-107]. Similar diffusion couples between $AlMgB_{14}$ and Ti and Fe showed some reaction with Fe at shorter times (2 hours) and no noticeable reaction or bonding in the Ti couple [3,14]. In a separate study, films of $AlMgB_{14}$ deposited by pulsed-laser deposition (PLD) on WC/Co substrates significantly increased the life-time over uncoated WC/Co during high-speed machining tests on Ti-6-4 alloy [108]. The $AlMgB_{14}$ coated tools also performed as well as commerical WC/Co tools with TiAlN coating, even though the laboratory prepared $AlMgB_{14}$ coatings are likely far from optimized [13].

Amorphous $AlMgB_{14}$ films deposited on SiO_2/Si substrates by PLD were found by nanoindentation to have hardnesses from 40-50 GPa [109-110]. Residual compressive stress may be a contributing factor in the reported values, but another interesting aspect of these films was their low coefficient of friction, between 0.04 and 0.05 [110]. The low friction was attributed to the formation of a boric acid (H_3BO_3) layer on the surface. A super-hard material could be particularly useful in micro-electro-mechanical systems (MEMS), especially since it develops its self-lubricating coating under typical atmospheric conditions.

1.9: Applications

The high pressures and temperatures required for formation of cBN and diamond are the prime reason for their high cost. The production cost of $AlMgB_{14}$ composites is potentially much lower. Very high pressures and temperatures are required to form the metastable cubic phase of boron nitride, on the order of 5000 MPa at 2000ºC and prices can range from $2000 to $7000 per pound [14]. Industrial quality diamond is even more expensive. The best $AlMgB_{14}$ composites are formed at only 106 MPa and 1400ºC and have an estimated cost of around $700 per pound at commercial production levels [3,14]. Additionally the metastable nature of diamond and cBN compromises their integrity at elevated temperatures, such as those encountered in high-speed machining. Degradation can be accelerated in the presence of reactive metals, such as Fe or Ti. Judging by hardness alone, diamond would be the ideal cutting material for all machining operations. But due to the high affinity of Fe for C, diamond tools degrade quickly during machining of steels. The temperature at the contact point between tool and workpiece has been

estimated anywhere from 700º to 1300ºC during machining due to friction and rapid shearing of the workpiece [13,56,106]. The high temperatures cause C from the diamond to diffuse into the steel chips and quickly dull the cutting edge. Effectively, the world's hardest material is eliminated from use in machining applications involving the world's most common alloy.

Current cutting tools used in titanium machining consist of WC-Co coated with TiN, TiC, AlN, or combinations of these [13]. This is done to protect the WC substrate from the Ti workpiece which, when hot, reacts aggressively with WC. Ti carbides, nitrides, and borides are all highly thermodynamically stable compounds, so Ti tends to react with all common tool materials (WC, cBN, and diamond). WC is selected only because of its lower cost and to act as a strong, hard substrate for the coating materials, which have lower strength. TiN and TiC protect the tool due to their stability with Ti metal, but once the coating is breached, the tool will wear rapidly. Since $AlMgB_{14}$ and TiB_2 are harder than WC and also show high stability against Ti metal, these composites are probably even more appropriate as bulk cutting materials than coatings, and this is substantiated by experimental findings mentioned in Chapter 1.8 [69-70,106-107].

Hard compounds such as diamond, SiC, and Al_2O_3 are commonly used in particulate form as abrasives. $AlMgB_{14}$-based composites may not offer improvement in this area due to the formation of a self-lubricating boric acid layer. But it has great potential as a low-friction and wear-resistant coating. As mentioned earlier, this includes coatings on MEMS devices, sliding mechanical contacts, digging and drilling faces, and slurry

processing plumbing, to name a few. Proposals vary from coatings on rotary components of vane pumps to helicopter blade faces for use in sandy environments [111]. Additionally, it is difficult to form the metastable diamond and cBN phases coatings by thin-film deposition techniques and impossible by certain thick-film techniques such as plasma spraying. $AlMgB_{14}$ films can be applied by PLD, and other techniques, including plasma spray, may be possible [14]. Although unrelated to the hard composites, $AlMgB_{14}$ is also a semiconductor and due to the arrangement of the B lattice and interstitial metal atoms, it is possible that electronic conduction in single crystals may be very anisotropic [25]. Preliminary observations by EDS have indicated that the metal atoms are mobile when irradiated by an electron beam, similar to ions in many oxide glasses [112-115].

1.10: Purpose of Study

The purpose of this study is to improve upon the mechanical properties of $AlMgB_{14}$ - 30 wt% TiB_2 composites initially reported in 2000 to exhibit microhardness up to 46 GPa [3]. The general goal is to find a ratio of $AlMgB_{14}$ and TiB_2 that results in an optimum combination of mechanical propeties. Doing so will hopefully increase the understanding of the mechanisms behind these properties. This includes the effects of microstructure, grain size, and impurity phases. Investigations into the origins of the intrisic high hardness of $AlMgB_{14}$ and its related compounds will also be made. Current and potential evaluation methods will be investigated in order to improve reliability of testing and possibly illuminate new potential applications.

Chapter 2: General Experimental Procedure

2.1: Powder Processing

The majority of the samples examined in this study were prepared through high-energy milling of powders and uni-axial hot-pressing into dense compacts. Though starting materials from a variety of sources were used in the work reported in Chapters 4-6, most $AlMgB_{14}$ samples are currently made using amorphous B (from 95 to 99 % pure, metals basis), distilled Mg (99.99 % pure), and Al wire (99.9999 % pure). Availability of boron powder has fluctuated over the course of experimentation, each change in source resulted in a change in purity. Aside from unknown levels of O contamination, the major contaminant of boron powder is Mg remaining from the reduction process, and this was of little concern in the preparation of $AlMgB_{14}$. The B powders were outgassed by the Ames Laboratory Materials Preparation Center between 800º and 1400ºC in vacuum to further reduce impurities, especially O which was found by neutron activation analysis to be present in objectionably high levels. Temperatures greater than 1100ºC resulted in a reaction between B and the Al_2O_3 crucible, and outgassing since has been limited to 1100ºC. The materials were handled in a He-filled glove box and weighed out with a 1:1:14 atomic ratio of Al, Mg, and B. The components were then loaded in small, hardened steel vials with a sealed lid along with three 8-gram and three 1-gram Cr-steel milling media. The small size of the vials and machines limits samples to only a few grams. Milling was done in high-energy Spex 8000 vibratory/oscillatory mills for 12 hours. The sealed vials were returned to the glove box after milling to retrieve the milled powder. Some material was lost to agglomeration against the walls of the vials, and only

powder that could be scraped away easily was recovered. The powder was then ready for hot-pressing to produce $AlMgB_{14}$ compacts (both powder and compacts hereinafter referred to as "baseline" material) or for subsequent processing to add second phases.

A second milling is usually used to add reinforcement phases to produce a boride composite. The most common additive is TiB_2; any other additional phases used were added by the following method unless otherwise described. Commercially prepared Aesar -325 mesh TiB_2 powder (99.5 % pure) was added in the fraction desired with milled baseline powder and loaded into a clean vial as in the previous step. This milling was done for only 30 minutes to reduce wear and contamination caused by the hard additive; it was only necessary to break down the <45 μm powder and ensure even mixing, not induce any mechanical alloying. TiB_2 (or other second phase) introduced by this method will be hereinafter referred to as mechanically milled (MM) powder.

Two other methods were sometimes used to introduce TiB_2 into the $AlMgB_{14}$ powder. The first involves milling B (as above) and Ti (Aesar -325 mesh, 99.5 % purity, metals basis) in a 2:1 (respectively) atomic ratio. Preparation and milling of the powder was done as described for the baseline powder, except the milling time was reduced to 6 hours. Powder recovered from this milling is referred to as mechanically alloyed (MA) TiB_2 and was added to the baseline powder in the same fashion as for the MM TiB_2. Again, only a 30-minute milling was required to ensure mixing and break-down of agglomerates, no additional alloying was needed. The third method involved weighing out Al, Mg, B, and Ti for the proper stoichiometric ratio of $AlMgB_{14}$ and TiB_2 in the

desired proportions of these two phases. This was mechanically alloyed for 12 hours, similarly to the production of baseline $AlMgB_{14}$. As the $Ti + 2\ B \rightarrow TiB_2$ reaction occurs during milling in the presence $AlMgB_{14}$ powders, this is referred to as the "in-situ method", or "in-situ TiB_2". No further powder processing steps were required.

As discussed earlier, two other mills employed in this study were a Fritsch P5 planetary mill and a Zoz CM01 Simoloyer high-speed attritor mill. These mills were used much less frequently, and the parameters of milling varied significantly. Both were capable of milling under inert atmosphere and the loading and unloading of powder within a glove box. Quantities of powder and media/powder ratios varied, but raw materials were weighed out stoichiometrically as above. Planetary milling times typically lasted 50 hrs, and the milling in the Zoz mill lasted 16 hrs.

Regardless of the milling method used to begin the processing, the powders were most often hot-pressed by the same method. Graphite dies with a bore diameter slightly larger than one-half inch were prepared by coating their interiors with a thin layer of hBN for both lubrication and protection of the dies. Half-inch diameter pushrods were also coated with hBN. The die components were then layered with a flexible graphite sheet material for additional protection. Powder was loaded into a die within the glove box, and the die-specimen assembly then transferred to the pressing chamber as quickly as possible to minimize contact with room air. The pressing chamber was then evacuated immediately, and high vacuum induced with a diffusion pump. The press used is capable of hot-pressing under vacuum or under inert gas, but in these studies pressing was done under

flowing Ar to help reduce Mg loss by vaporization. Pressing occurred at 1400ºC under 106 MPa for 1 hour, unless otherwise specified. Sintering temperatures as low as 1300ºC or as high as 1500ºC have been used occasionally. After pressing, the pellet was removed and cleaned by sand blasting. A dense compact was usually produced, and this was typically polished on at least one surface prior to subsequent analysis.

Since the resulting compacts are very hard, polishing requires much more time, effort, and resources than normal metallographic polishing operations, and diamond is the only effective abrasive. As-hot-pressed compacts have a rough surface and have significant amounts of extrudate attached resulting from powder flow and extrusion around the pushrods. Facing of the compacts with a high-speed diamond grinder or by electro-discharge machining (EDM) can reduce hand grinding time and produce flat, parallel faces. Facing of both sides is required for ultrasonic modulus testing, with sample thicknesses ranging from 1 to 3 mm. High-speed diamond grinding could result in violent fracture of compacts, but EDM was only effective when the sample conductivity is high enough (typically when the TiB_2 fraction is greater than 50 wt%).

When at least one flat surface was produced, the samples were mounted in Buehler Epoxicure resin. Past attempts to mount samples in diallyl phthalate or phenolic resin resulted in significant thermal shock to the composites due to rapid cooling cycles typically used. To save time, batches of up to six samples were polished with a Buehler Automet 2 mechanical polisher. The first polishing step involves grinding with a combination of a metal-bonded 45-µm diamond pad and a 45-µm diamond suspension to

increase material removal rates. The next two steps use 9- and 6-µm diamond suspensions, respectively, on discontinuous pads to again improve removal rates. A 3-µm diamond suspension on felt is used next. Due to the hardness of the samples, 3-µm diamond particles leave few scratches, though there is usually some material pull-out from the polishing process that gives the illusion of higher porosity. A final step can be used to remove most of this effect, by vibratory polishing of the samples under a submersion of colloidal silica. The majority of material removal is by action of etching, and differential erosion rates of the various phases can result in a slightly uneven surface which may give the illusion of non-existent microstructural features during microscopy. Polished samples were then ready for hardness testing, SEM analysis, etc.

2.2: Direct Reaction

High-purity boride samples have been produced by a direct reaction synthesis method. Batches were again weighed out stoichiometrically to a 1:1:14 atomic ratio in an inert atmosphere and then loaded into Ta tubes. The Ta tubes were closed by arc welding and subsequently sealed in quartz tubes. Due to the low strength of fused quartz at the highest temperatures used, the tubes were backfilled with Ar to a pressure that would reach roughly 1 atm at the heat treatment temperature. The pure elements used were distilled Mg (99.999 % pure), isotopically pure ^{11}B (99.999 % pure), and Al wire (99.9999 % pure). This B is used only because of its high elemental purity, the isotope is not a concern and is assumed to have little effect on the chemical properties. Borides in the $AlMgB_{14}$ family studied thus far appear to require different heat treatments to produce the purest samples, and therefore treatments lasted from 6 to 100 hours at

anywhere from 950 to 1300ºC. Additional details of these experiments are presented in Chapter 3.

2.3: Analysis

Standard analysis of the composite materials included microhardness and ultrasonic modulus testing. From these results, toughness was also estimated. Scanning electron microscopy was frequently used to analyze the microstructure as the majority of the materials contained sub-micron grains. X-ray diffraction was used to verify phases and identify unknown impurities and reactions. Wear resistance was commonly evaluated by dry impact erosion testing, although occasionally by wet abrasion or scratch testing [69-70].

A brief description of commercial hard material samples used for comparison is listed here. WC/Co refers to K-68 grade cemented carbide from Kennametal, containing 6 wt% Co binder and engineered for reasonable wear resistance and toughness. WC usually refers to a near-binderless (monolithic), fine-grained WC tool also from Kennametal, sold under the name RocTec500, consolidated by a rapid, high-pressure compaction technique and also designed for wear resistance, among the best for WC and comparable in many applications to the most wear resistant grades of cBN tools. This aforementioned superior wear-resistant cBN tool is called Borazon 7000 from Diamond Innovations. Another cBN tool is mentioned in Chapter 5 (simply referred to as CBN), is from J&M Diamond, and is in most respects a lower grade tool than the Borazon 7000. Another sample, a poly-crystalline diamond tool (PCD) also from J&M Diamond is used in some

tests, but it does not typically perform better than the $AlMgB_{14}$ -TiB_2 composites nor the wear-resistant grades of WC and cBN, and is thus not particularly scrutinized.

Hardness measurements were performed with a Wilson-Tukon 200 model microhardness tester using a Vickers indenter. This microhardness unit was limited to a testing load of 1000 gm-f. Toughness was estimated by the Palmqvist technique which measures average crack length extending from indentation corners, and calculated using Equation (3) in Chapter 1.7. Equation (3), for penny-shaped cracks, is used because it provides the most conservative estimate for toughness since the largest fracture area is assumed. Until equipment with the range of loads required to determine the regimes of each indent crack mode is available, this minimum estimation will be used for consistency.

Elastic properties were measured by ultrasonic wave propagation on compacts with both sides faced parallel (polishing was not necessary). A sample was clamped between transmission and receiver transducers connected to a receiver and oscilloscope. Due to the low thickness and high modulus of the samples, the time of wave travel was measured with a thicker quartz block standard to slow the sound waves and differentiate peaks on the detector. Honey was used as a medium between the transducers and materials as it is effective at transmitting both shear and longitudinal waves. Transverse and longitudinal wave speeds were measured separately with different pairs of transducers. With the time of travel and thickness of the sample, the speed of each wave was known. From these two waves and the sample density, five elastic constants could be calculated, as shown in the following equations [116]:

$$L = \rho v_L^2 \qquad G = \rho v_T^2$$

$$E = \rho v_T^2 \frac{(3v_L^2 - 4v_T^2)}{(v_L^2 - v_T^2)} \qquad B = \rho(v_L^2 - \frac{4}{3} v_T^2) \qquad (5\text{-}9)$$

$$\nu = \frac{(v_L^2 - 2v_T^2)}{2(v_L^2 - v_T^2)}$$

Where ρ is the density (kg/m^3) and v_L and v_T are the longitudinal and transverse sound velocities (m/s), respectively. L, G, E, and B are the longitudinal, shear, elastic, and bulk moduli (Pa), respectively, and ν is Poisson's ratio.

Erosion testing was performed with a Comco, Inc. Microblaster, in accordance with the ASTM G 76 standard. Typically, +100 micron, angular Al_2O_3 grit was used as the abrasive at speeds of approximately 77 m/s. The samples were cleaned with ethanol and an ultrasonic bath to remove loosely bonded grit before weighing. The mass of each sample was measured 10 times each at 0, 30, 60, 120, 180, and 240 minutes total of erosion. Multiple measurements were averaged to reduce error as the mass loss of a typical sample at each stage was only about 1 mg or less. The mass of erodent used was also weighed at each stage. The erosive jet was constrained to a diameter much smaller than each sample so that all erodent impacts the target, and used grit was collected and never reused.

A JEOL 5910 thermal emission, tungsten filament SEM was used primarily to study the microstructure of the various composites; this unit has EDS capabilities for verifying phases. SEM was typically not used for measurement of hardness indentations since the

features of the indents offered much less contrast than in optical microscopy and were further obscured by the high Z-contrast of the phases. The propagation of cracks resulting from hardness indents were examined though, along with failure modes on fracture surfaces and erosion craters. Secondary electron (SE) imaging typically provided some degree of phase contrast in the $AlMgB_{14}$ - TiB_2 composites. Backscattered electron (BSE) imaging was also used for higher phase contrast and location of impurity phases. As mentioned earlier, EDS is especially unreliable for quantitative compositional analysis of boron-rich materials, and only was used to identify elements present.

XRD patterns were taken with a Scintag PadV diffractometer using CuK_α radiation. Diffraction patterns were typically used only for phase verification, though occasionally patterns were indexed to identify unknown phases or used in structure refinement analysis. Only as-milled powder and the occasional crushed hot-pressed sample were examined by powder diffraction. Most hot-pressed samples were analyzed on their polished faces, and it was assumed that the fine microstructure did not produce any preferential orientation.

Chapter 3: Direct reaction synthesis of Mg_2B_{14} from elemental precursors

A paper published in *Scripta Materialia*

J.S. Peters[1], J.M. Hill[2], A.M. Russell[1]

[1]Ames Laboratory and Department of Materials Science and Engineering, and
[2]Ames Laboratory and Department of Physics and Astronomy,
Iowa State University, Ames, IA 50011 USA

3.1: Abstract

Mg_2B_{14} prepared by reaction of high-purity Mg and B was analyzed by XRD and Rietveld analysis. The structure refinement for space group *Imam* resulted in residuals R_p = 6.95 % and R_{Bragg} = 3.72 % with lattice parameters a = 5.9738(3) Å, b = 8.1255(4) Å, and c = 10.4809(5) Å. $AlMgB_{14}$ produced by the same method did not yield high-purity specimens.

3.2: Introduction

The hard material $AlMgB_{14}$ possesses properties that differ from conventional hard materials. One important distinction is the compound's complex crystal structure (oI64, space group *Imam*), which is unlike the high-symmetry unit cells (cF8) of compounds like diamond, cubic boron nitride (CBN), and the hexagonal unit cell of δ-WC. Previous studies of $AlMgB_{14}$ have focused primarily upon crystal structure determination with little investigation of electrical, thermal, and mechanical properties. $AlMgB_{14}$ is intrinsically hard (30 GPa), and two-phase sub-micron composites of $AlMgB_{14}$ and TiB_2 have been produced exhibiting hardness values as high as CBN (45 GPa) [3]. To

improve understanding of these $AlMgB_{14}$ - TiB_2 composites, the basic properties of $AlMgB_{14}$ need to be investigated, especially its structure-hardness relationship.

The Al and Mg lattice sites in $AlMgB_{14}$ are not fully occupied; an actual stoichiometry of $Al_{0.75}Mg_{0.78}B_{14}$ has been reported [9]. Thus, any study of $AlMgB_{14}$ should account for the variability in Al and Mg site occupancy. This phenomenon makes it important to also study the isostructural compound Mg_2B_{14}, which represents the limiting case of complete substitution of Mg for Al on the Al sites. In previous experiments on the crystallography and properties of $AlMgB_{14}$, material was produced by crystal growth in a molten Al flux [8-9]. In the processing of high-hardness $AlMgB_{14}$-based composites, the material was prepared by high-energy milling of the constituent elements and subsequent hot-pressing of the nanoscale powders. It is unknown what effect different methods of production may have on the stoichiometry of $AlMgB_{14}$, partly because the high-hardness composites contain impurity phases that make structure refinement particularly challenging. In this study, high-purity Mg_2B_{14} was produced and crystal structure refinement was performed using powder X-ray diffraction measurements. The reaction methods employed for Mg_2B_{14} were then applied to synthesis of $AlMgB_{14}$ in order to determine if these methods might reduce the comparatively high impurity levels typically seen in $AlMgB_{14}$ produced by mechanical alloying and hot pressing [101].

Mg_2B_{14} and $AlMgB_{14}$ are both characterized by an orthorhombic unit cell consisting of a framework of B_{12} icosahedra with B, Mg, and Al atoms located on interior sites within the unit cell. There are two different metal sites within the unit cell (Mg on the 4e and Al

on the 4d sites), each possessing a different size. In addition, there are 8 B sites in the interior of the unit cell, given by the 8h Wykoff positions. As mentioned in the preceding paragraph, these metal sites are not fully occupied; the actual stoichiometries have been reported as $Mg_{1.93}B_{14}$ and $Al_{0.75}Mg_{0.78}B_{14}$ [7,9]. There are 10 other known compounds with this same structure in which the metal sites are occupied by various other elements, each having different site occupancies [6,10-12]. The stoichiometry of these compounds ranges from $Al_{0.96}Li_1B_{14}$ to $Al_{0.62}Tm_{0.57}B_{14}$ [6,12]. Microhardness measurements on single crystals of some of these compounds suggest that hardness may depend on the identities and occupancies of the elements on the metal sites, and how these atoms are chemically bonded to the icosahedra [4,50]. Most of these previous investigations examined crystals produced in the presence of an excess of one of the metal constituents (i.e., flux growth), and it is uncertain whether the same compounds produced by other methods might possess a range of stable or meta-stable occupancies on the metal sites.

Hill, et al used high-temperature reaction synthesis to produce $AlMgB_{14}$ powders, though none were sufficiently phase-pure for accurate crystal structure refinement by X-ray diffraction [117]. In this study, the earlier methods were modified in an attempt to produce both $AlMgB_{14}$ and Mg_2B_{14} powders of higher purity. The high-hardness $AlMgB_{14}$ composites discussed earlier were produced with the stoichiometric ratio (1:1:14) of the constituents. Therefore, the same ratio was used in this synthesis, and flux growth methods were avoided due to the possible excess of metallic elements.

3.3: Experimental Procedures

Mg_2B_{14} powders were prepared by reaction of high-purity elemental Mg and B in Ta tubes at elevated temperatures, employing a method similar to that described by Hill, et al [117]. Distilled Mg produced by Ames Laboratory's Materials Preparation Center and isotopically pure ^{11}B from Eagle-Pitcher (both 99.999% pure, metals basis) were used as starting materials. The pure elements were weighed to achieve a ratio of 0.2400 g Mg to 0.7600 g B per gram of sample, which produces the 1:7 molar ratio of stoichiometric Mg_2B_{14}. The weighed materials were then placed into Ta tubes under He atmosphere in a glove box. To minimize O contamination, the tubes were tightly crimped in the glove box and transferred immediately to an arc welding chamber that was evacuated and flushed repeatedly with Ar. The tubes were chilled by direct contact with large Cu heat sinks and welded rapidly to prevent Mg vaporization. The Ta tubes were then sealed in silica ampoules to protect them from oxidation during heat treatment. Table 3.1 shows the time and temperature schedule for the seven reaction trials. $AlMgB_{14}$ samples were also prepared as described above, with Al wire from Cominco (99.9999% pure, metals basis), but with a 1:1:14 molar ratio of Al, Mg, and B to simulate the material in the previously mentioned high-hardness composites. Two samples were heated for 6 and 24 hours at 1300ºC.

Table 3.1: Isothermal reaction times and temperatures employed for synthesis of seven Mg_2B_{14} and two $AlMgB_{14}$ samples.

	6 hours	24 hours	100 hours
950ºC		Mg_2B_{14}	Mg_2B_{14}
1100ºC	Mg_2B_{14}	Mg_2B_{14}	Mg_2B_{14}
1300ºC	Mg_2B_{14}, $AlMgB_{14}$	Mg_2B_{14}, $AlMgB_{14}$	

3.4: Results

X-ray diffraction (XRD) patterns were taken for each powder sample using a Scintag PadV X-ray diffractometer with CuKα radiation. The $AlMgB_{14}$ samples were found to contain $AlMgB_{14}$ in addition to other phases. There were some differences between these samples and those produced by Hill et al, however, the diffraction patterns contained too many impurity peaks to allow crystal structure refinement; consequently, they were not studied further [117].

All of the samples prepared as Mg_2B_{14} contained at least some of the desired phase, although the reaction appeared to reach completion only for those heat-treated at 1300ºC. A brick-red powder was observed when treated at this temperature, as described by Guette, et al [7]. The powders synthesized at the lower temperatures contained Mg_2B_{14} and MgB_4, resulting in samples that had a dark grey appearance with varying degrees of redness. The progression of the reaction from low to high temperature can be seen in the XRD patterns in Figure 3.1. The unindexed peak at about 44º 2θ was seen in all samples, but was weakest in the samples that were produced at 1300ºC. The XRD pattern of one such sample is shown in Figure 3.2. This peak was also prominent in the $AlMgB_{14}$ samples. The peak did not match any of the expected alternate or impurity phases; neither did it appear in the diffraction pattern of the B starting material. From comparison of XRD patterns of the $AlMgB_{14}$ and Mg_2B_{14} samples, the strongest unidentified peak at about 44º 2θ, in conjunction with other peaks, appears to correspond to an AlB_2-type phase (hP3 , space group *P6/mmm*). The peak positions suggest existence of a $(Mg,Ta)B_2$ phase of undetermined composition, possibly containing Al as

well in the $AlMgB_{14}$ samples. This phase has not been detected by energy dispersive spectroscopy (EDS) of the powders.

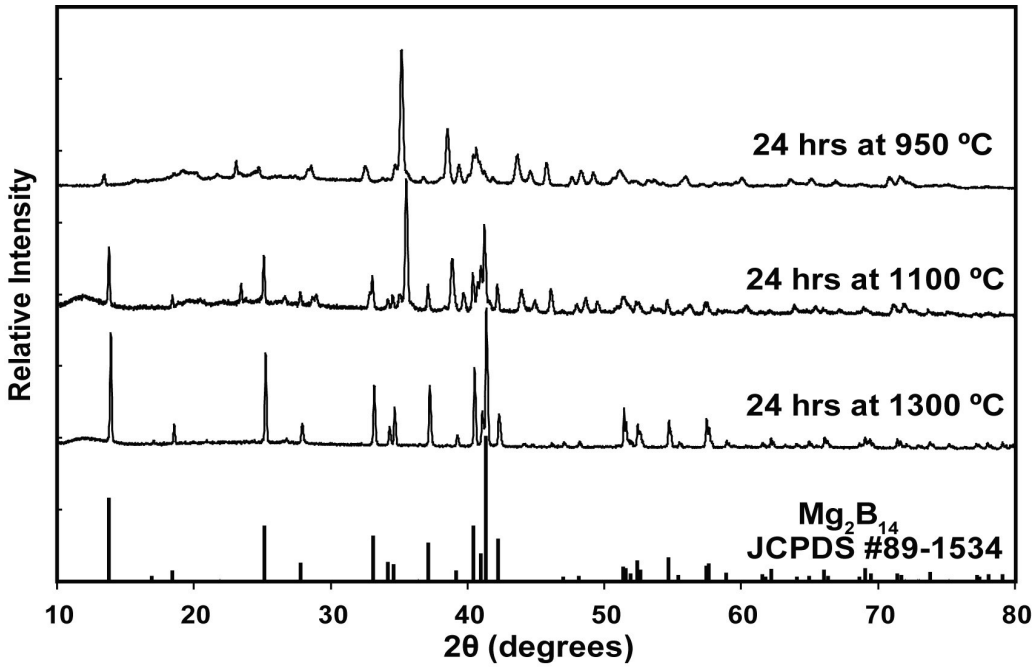

Figure 3.1: X-ray diffraction patterns for Mg_2B_{14} samples prepared over a range of temperatures.

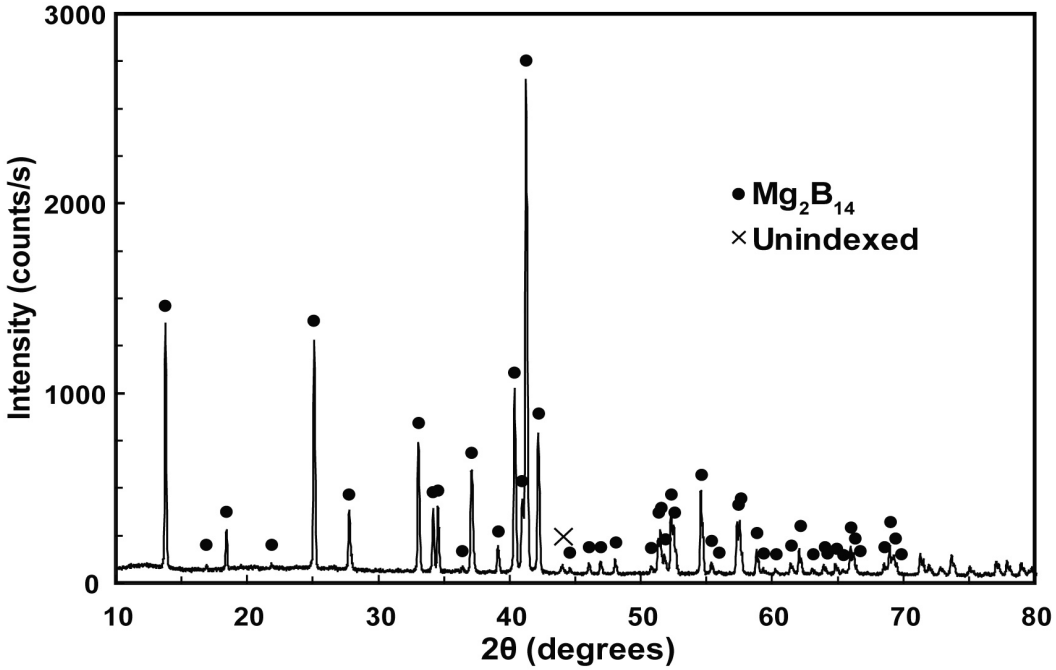

Figure 3.2: X-ray diffraction pattern of Mg_2B_{14} synthesized at 1300ºC for 6 hours.

The coarse Mg_2B_{14} powder synthesized at 1300ºC for 6 hours was ground with an agate mortar and pestle in a glove box, though the powder had been previously exposed to air for about 2 weeks. The ground powder was sealed as before and held for an additional 19 hours at 1300ºC to determine if the Mg_2B_{14} reaction would proceed further and to observe its effect on the unidentified peaks. The XRD pattern for this reprocessed sample was virtually the same and still contained the small unidentified peak at 44º 2θ. An identical sample was prepared and heated at 1300ºC for 6 hours followed by a quench in liquid N_2 to see if any metastable phases might form. The quench rate appeared to be rather moderate because the silica capsule was not breached and boiling N_2 vapor inhibited direct contact between the liquid N_2 and the silica capsule. The diffraction pattern for this sample was essentially identical to that for other powders produced at 1300ºC.

The powder diffraction pattern of the sample prepared at 1300ºC for 6 hours was refined by the Rietveld method [118] using Rietica software. The unidentified peaks were excluded from the refinement (see Figure 3.2). The structure refinement resulted in final residuals R_p = 6.95 % and R_{Bragg} = 3.72 % [119]. By indexing the Mg_2B_{14} pattern for the orthorhombic space group *Imam*, the lattice parameters were found to be: a = 5.9738(3) Å; b = 8.1255(4) Å; and c = 10.4809(5) Å. These values are in close agreement with those reported by Guette, et al [7]. The Mg occupancies were calculated to be about 97% for both the large and small sites.

3.5: Discussion

The synthesis approach described above was found to produce both Mg_2B_{14} and $AlMgB_{14}$ powders. However, the two compositions did not possess a comparable degree of purity. The spinel phase that resulted from O contamination in mechanically alloyed and hot pressed samples, as well as in earlier $AlMgB_{14}$ produced by direct reaction [117], was absent in the $AlMgB_{14}$ compositions. Still, the levels of other phases remained too high (approximately 30%) for the structure to be refined. The powder diffraction pattern for one $AlMgB_{14}$ sample can be seen in Figure 3.3. Since the stoichiometry has been reported as $Al_{0.75}Mg_{0.78}B_{14}$, the higher 1:1:14 ratio used in the production of this material may be the source of some of the impurity phases [9HigIto]. This would suggest an upper bound on the solubility of Al and Mg in the 1:1:14 structure. If there is a solubility range in the structure, perhaps sub-stoichiometric compositions should be examined.

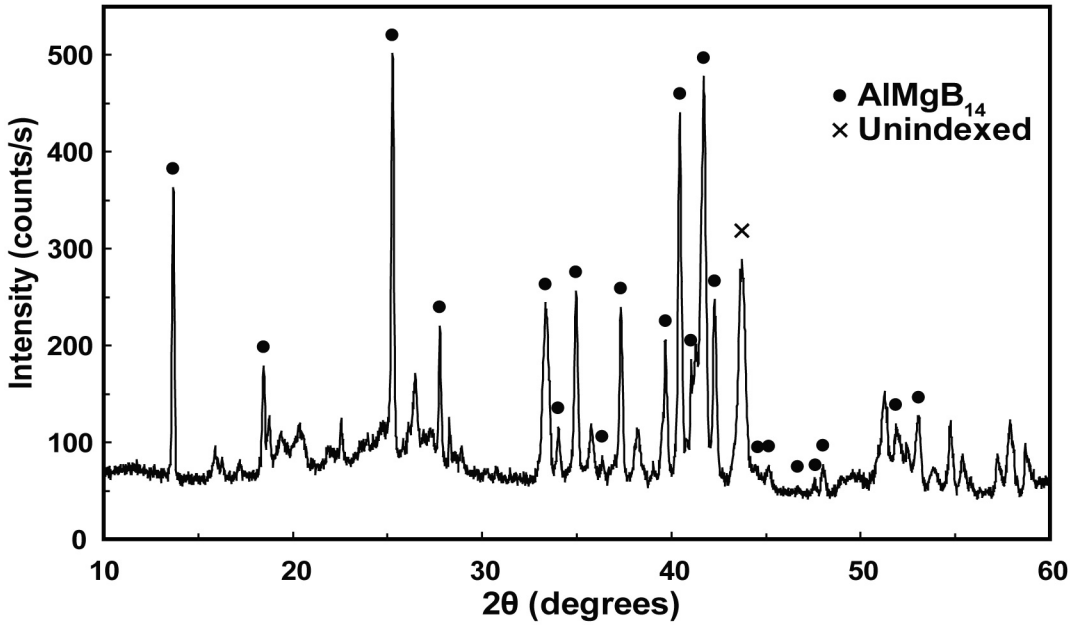

Figure 3.3: X-ray diffraction pattern of $AlMgB_{14}$ reacted for 6 hours at 1300ºC. Unindexed peak marked with "X" matches unidentified peak seen in Mg_2B_{14} samples.

The Mg_2B_{14} produced was sufficiently pure for crystal structure refinement, which resulted in both Mg site occupancies equaling about 97%. Guette, et al reported occupancies of 93% for the larger site. The larger site was the only occupancy parameter refined; Guette held the smaller site occupancy at 100% [7]. It has not yet been resolved whether these differences are a result of material preparation or data analysis.

In order to understand the origin of high hardness in single phase $AlMgB_{14}$, high-purity samples of the material are needed. The inability to produce $AlMgB_{14}$ and Mg_2B_{14} by the same method suggests the likelihood of thermodynamic and/or kinetic differences between the two compounds. If the major impurity phase is of the AlB_2-type, the presence of aluminum in the $AlMgB_{14}$ samples may increase the driving force for the formation of this impurity phase. Another intriguing possibility would be to produce an intermediate boride with a composition between $Al_{0.75}Mg_{0.78}B_{14}$ and $Mg_{1.93}B_{14}$ to determine if a single-phase solution of the compounds is possible.

3.6: Acknowledgments

The authors gratefully acknowledge the guidance provided by David Johnston and Bruce Cook in planning these experiments and in and analyzing the results. This work was supported by the U.S. Department of Energy, Office of Energy Efficiency and Renewable Energy, Industrial Technology Program. Ames Laboratory is operated for the U.S. Department of Energy by Iowa State University under Contract Number W-7405-ENG-82.

Chapter 4: Microstructure-property relationships in ultra-hard $AlMgB_{14}$

A paper published in *Proceedings of the 2005 International Conference on Powder Metallurgy & Particulate Materials*

Justin S. Peters[2], Bruce A. Cook[1],
Joel L. Harringa[1], Alan M. Russell[2], and Alfred Kracher[1]

[1]Materials and Engineering Physics Program, Ames Laboratory, USDOE
[2]Department of Materials Science and Engineering,
Iowa State University
Ames, Iowa 50011

4.1: Abstract

$AlMgB_{14}$ based composites have many potential applications in industry, but better understanding of the mechanisms responsible for high hardness and wear resistance is required for the implementation of this technology. This study was performed to determine if the results of electron probe microanalysis (EPMA) could be correlated with the observed variations in local hardness and toughness. The relationship between microstructure and hardness in $AlMgB_{14}$ was investigated to improve the processing of this ultra-hard ceramic and its related composites. High-energy milling and subsequent hot-pressing of the powders produced dense composites with high hardness, but inconsistencies in powder processing and microstructure have led to variations in hardness. The morphology of the microstructure and distribution of O and Fe containing impurities were compared to the local hardness.

4.2: Introduction

Several years ago, research on hard materials centered primarily on bond strength, but recent discoveries in the search for new hard materials have broadened the focus to

include microstructural effects on hardness, whereby increased hardness is partially achieved by producing nanoscale microstructures [22,120]. High wear resistance is another attribute of many hard materials. Wear resistance is a result of not only hardness, but also the toughness of a material. It has been suggested that a microstructure consisting of a multi-modal distribution of reinforcement sizes is more desirable for improving wear resistance than one with rigid size control [98].

In the production of wear resistant and ultra-hard $AlMgB_{14}$ based composites, these types of microstructures are produced by the hot consolidation of nanoscale powders which are themselves produced by high-energy milling [3]. There are many variables in such a powder processing method and a considerable range of particle sizes produced by any given set of variables. Inhomogeneous microstructures are often observed in materials consolidated from these powders. For example, Figure 4.1 shows agglomeration of TiB_2 powder particles that often results from high-energy milling. Each agglomerate is composed of many finer particles, yet they result in uneven densification and distribution of the phases and impurities in the final product.

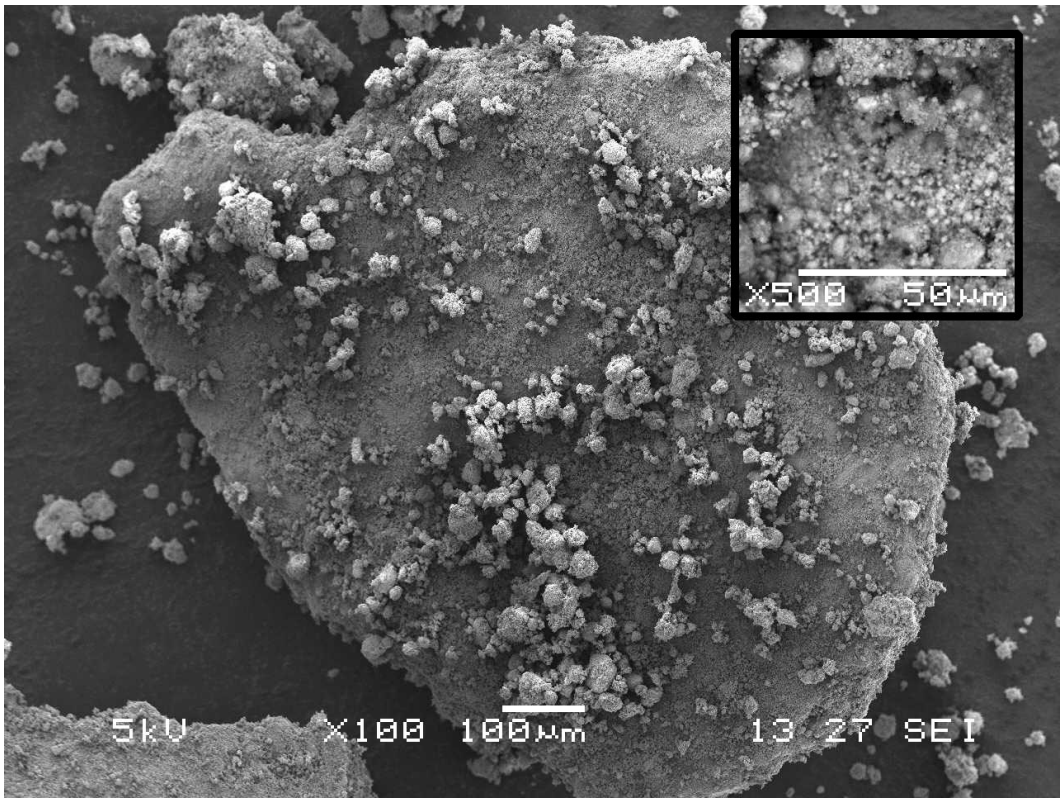

Figure 4.1: Secondary electron image of high-energy milled TiB_2 powders in heavily agglomerated form.

$AlMgB_{14}$ is an intrinsically hard compound, around 30 GPa, but some of its composites exhibit hardness considerably greater than would be predicted from the properties of their constituent materials by a rule of mixtures [3,69]. The most heavily studied of these composites, $AlMgB_{14}$-TiB_2, has shown a maximum observed hardness of 46 GPa [3]. A significant portion of this hardness increase is attributed to sub-micron and nanoscale microstructures, and therefore their properties, including hardness, should be strongly dependent on these microstructural variations.

Powder processing of the constituent materials, followed by uni-axial hot pressing can produce a wide range of microstructures, depending on the form of the precursor material (e.g., chunk vs. powders), milling parameters (ball-to-charge mass ratio, milling

environment, milling duration), and use of process control agents. Figure 4.2 shows the wide range of microstructures obtained in composites of $AlMgB_{14}$-TiB_2 prepared by mechanical alloying.

Figure 4.2(A) illustrates an extreme example of an inhomogeneous microstructure resulting from high-energy milling using chunk boron precursor material where the size of single phase regions measures from many microns to less than 100 nanometers. In this micrograph, the dark regions correspond to remnants of the elemental boron pieces that were incompletely comminuted. Figure 4.2(B) shows a microstructure obtained by high-energy vibratory milling of elemental powders, while Figure 4.2(C) shows a representative microstructure resulting from attritor powder. Note the significant difference in phase distribution and size resulting from the various types of milling equipment (all micrographs were obtained at a magnification of 1000x.) The microstructure represented in Figure 4.2(B) gives the best wear resistance of the three shown.

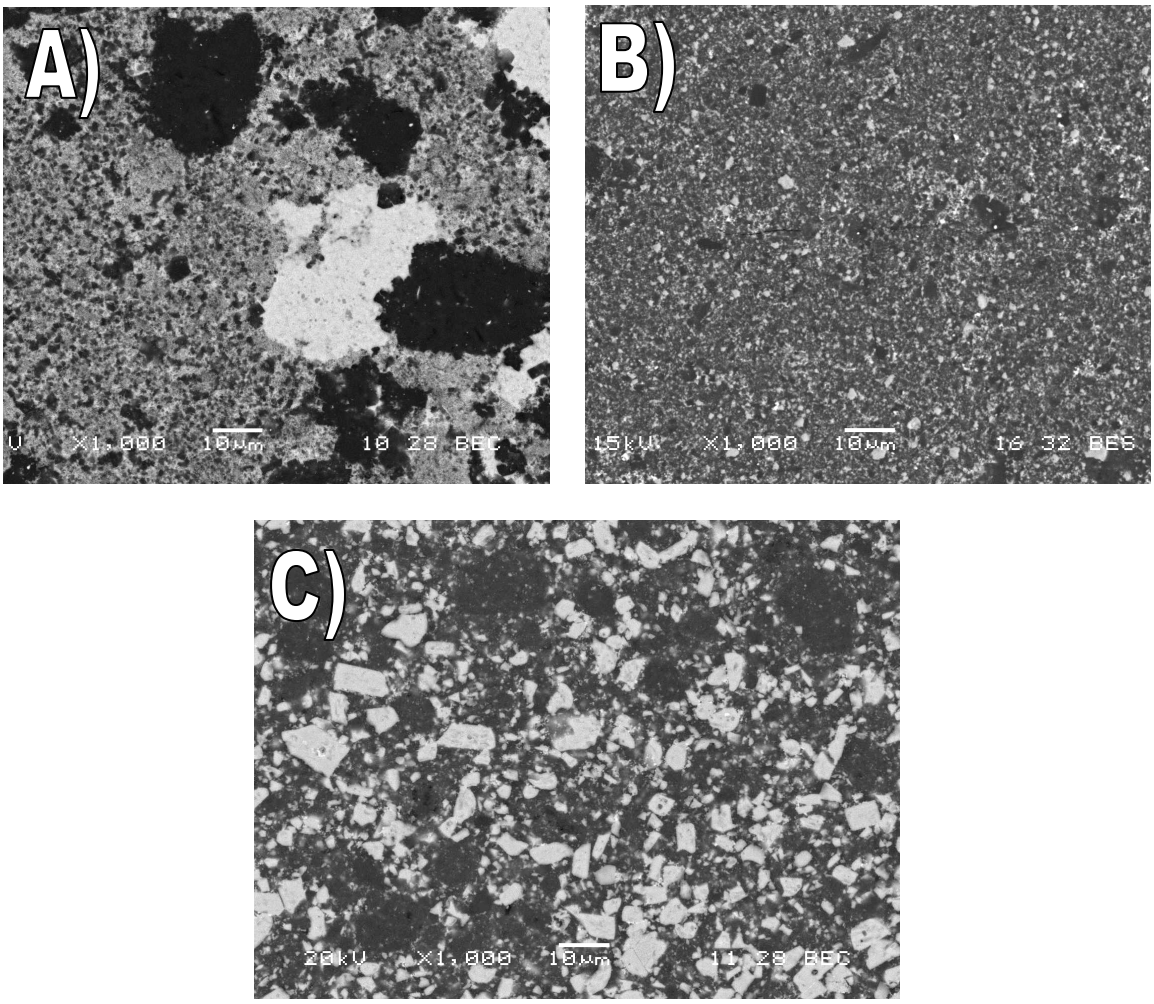

Figure 4.2: Backscattered electron images showing range of microstructural variations in $AlMgB_{14}$ - 30 wt% TiB_2 composites prepared by mechanical alloying. Dark regions are $AlMgB_{14}$, white corresponds to TiB_2, and the grey regions are a nanoscale mixture of the two phases. A) vibratory-milled, prepared from chunk boron, B) vibratory-milled, prepared from elemental powders, C) attritor-milled, prepared from elemental powders. Note the difference in phase distribution and size resulting from the various types of milling equipment (all micrographs were obtained at a magnification of 1000x)

Changes in processing parameters can result in differences in properties, but quantification of the microstructural aspects that result in these differences is the current challenge. Always present in these microstructures are an inhomogeneous distribution of reinforcement phases of varying size range, impurity phases, and porosity. In the two-phase composites, phase size can be determined, but the actual grain size is largely unresolved due to the extremely small crystallite size and difficulty in chemically etching

the material. TEM analysis and SEM observations of selected samples suggests that the crystallite size can range anywhere from 1 μm to 100 nm or smaller [101]. Most impurity phases (caused by oxygen and iron contamination) are also smaller than 1 μm, making them unsuitable for identification by energy dispersive spectroscopy (EDS). The impurity phases commonly expected are FeB and $MgAl_2O_4$ (spinel), both of which reduce the hardness and toughness of the bulk material [24,101].

One method for quantifying the effects of different microstructures is to produce materials by using different processing parameters. It is possible to adjust starting material form and purity, second phase fraction, and milling parameters such as time and media loading to produce different microstructures. In powder processing, these changes can also introduce other issues, such as impurity concentration and extent of particle agglomeration, which complicates the direct comparison of the varying microstructures. In these composites, altering any of these parameters often results in equally inhomogeneous microstructures, and the effects on the mechanical properties cannot be directly correlated to a single variable, which again makes quantification on the microscale challenging [71].

An alternate approach is to examine the variations in microstructure present within one inhomogeneous sample. With a fixed set of processing parameters, the number of unwanted variables could be minimized. In this study, average composition in the region directly under a hardness indent was used as an indicator of the level of O and Fe contamination and therefore impurity phase concentration. Composition was measured

by X-ray dispersive spectroscopy using an electron probe microanalyzer (EPMA). $AlMgB_{14}$ with no additives was selected in order to minimize the number of processing and microstructural parameters. This method gives one set of quantifiable parameters that can be related to hardness with more certainty than qualitative observations about the microstructure.

Another aspect of $AlMgB_{14}$ under investigation is the occupancy of the Al and Mg atoms within the lattice. The actual stoichiometry of the compound has been shown to be $Al_{0.75}Mg_{0.78}B_{14}$ [9HigIto]. The previous study produced material by a flux growth method in liquid Al, and it is unknown if high-energy milling produces $AlMgB_{14}$ of a different stoichiometry. Verification of the actual stoichiometry of the milled and hot-pressed $AlMgB_{14}$ by X-ray diffraction has been complicated by the presence of impurity phases [117]. If the site occupancies vary in this material, it may affect the hardness, among other properties. The local concentrations of Al and Mg within the lattice were also examined for evidence of changes in occupancy.

4.3: Experimental

$AlMgB_{14}$ powder was produced by comminuting high-purity elemental powders in a Spex-8000 vibratory/oscillatory mill. The initial charge was a mixture of B powder, Al wire, and distilled Mg of 99%, 99.9999%, and 99.99% purity by metals basis, respectively. The boron was previously outgassed under vacuum at 800ºC to reduce impurities, especially oxygen. This mixture was sealed under He atmosphere in a hardened steel vial with three 8 g and three 1 g chrome steel milling media. Milling was

performed for 12 hours, and the powder was retrieved in a dry He atmosphere glove box. The milled powder was loaded in a graphite die for pressure-assisted reaction sintering in a uni-axial hot press under inert Ar atmosphere. Pressing occurred at 1400ºC under a pressure of 106 MPa for 1 hour, which produced a half-inch compact of nearly 100% theoretical density. The compact was polished with diamond abrasives down to 1 μm for optical and electron microscopy.

Microstructual variations were quantified by measuring the local composition where a hardness indent was to be placed. This was done prior to indentation because X-ray spectroscopy requires a flat surface for semi-quantitative analysis. Attempts were made to analyze the composition around the perimeter of previously made indentations, but this method did not adequately characterize the microstructure directly under the plastic zone. Regions of interest were mapped on the sample surface by establishing a rectangular outline of Vickers micro-indents. The outline of indents served as reference points for the multiple points that were to be subsequently analyzed. Micrographs of each region were taken with a JEOL 5910 LV SEM. The composition of each corresponding region was measured by wavelength dispersive spectroscopy (WDS) in a JEOL 8200 EPMA utilizing standards correction for quantitative analysis. A 20 μm defocused beam was used to approximately match the size of a typical Vickers indent in the baseline material. Vickers hardness indents were then placed on the measured points using a Wilson Tukon microhardness tester with a load of 1000 g. The reference indents were again used to locate these points because the microstructural features of interest were not clearly visible

in the optical microscope. Each indent was measured multiple times to reduce error. Figure 4.3 shows one analyzed region with indents marked for clarity.

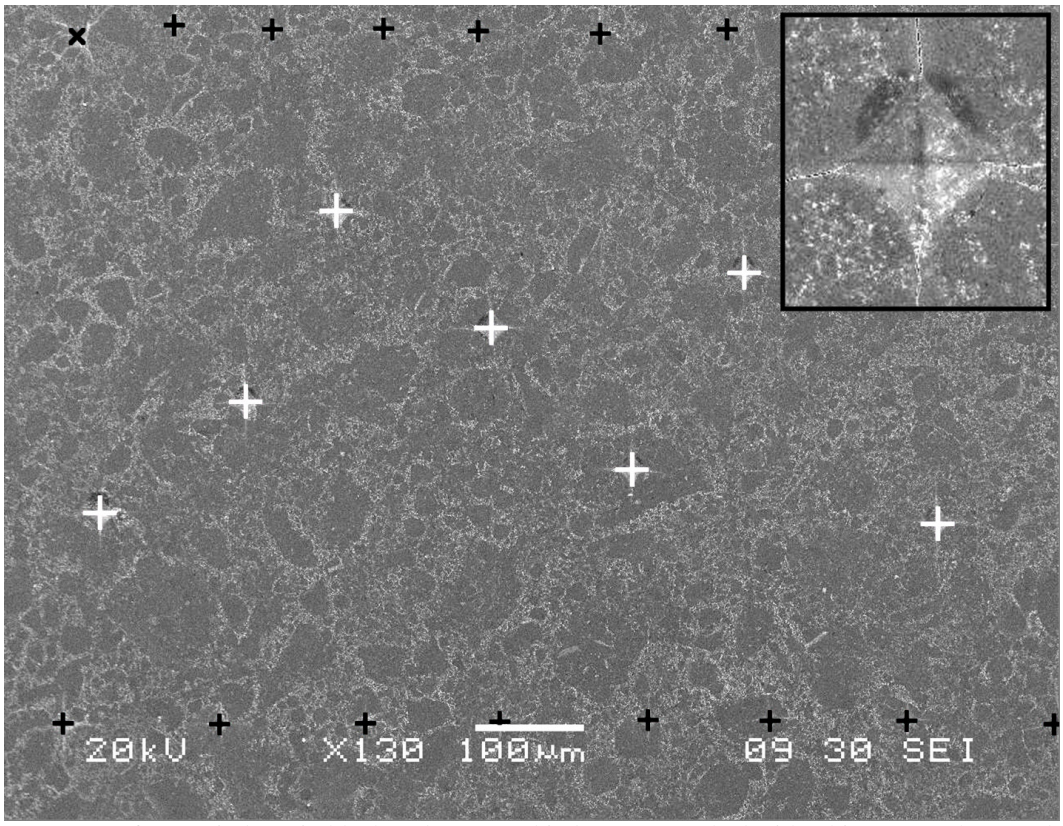

Figure 4.3: Reference indents in black and measured indents are marked with white. Inset shows a dark circle etched by the electron beam and its proximity to the diamond of the plastically deformed region overlapping the analyzed point. Brighter contrast regions contain higher levels of O, Fe, and/or porosity.

4.4: Results

Multiple data values from the EPMA were compared to the results of hardness measurements to evaluate possible relationships between phase composition and hardness. The elements of interest were B, Al, Mg, O, Fe, and Cr. Oxygen is present due to contamination of the surfaces of the initial powders before processing and iron and chromium are both introduced during the milling process as a result of wear debris from the milling media. A relationship between hardness and the ratios of the Al and Mg

concentrations was also examined because the exact occupancies of Al and Mg within the lattice are not known for this method of production of $AlMgB_{14}$. A total of 23 points were analyzed, with Vickers hardness measurements ranging from 2500 to 3300 kg-f/mm^2. Hardness is shown versus Fe and O content, each of which represents a major impurity phase (Figure 4.4).

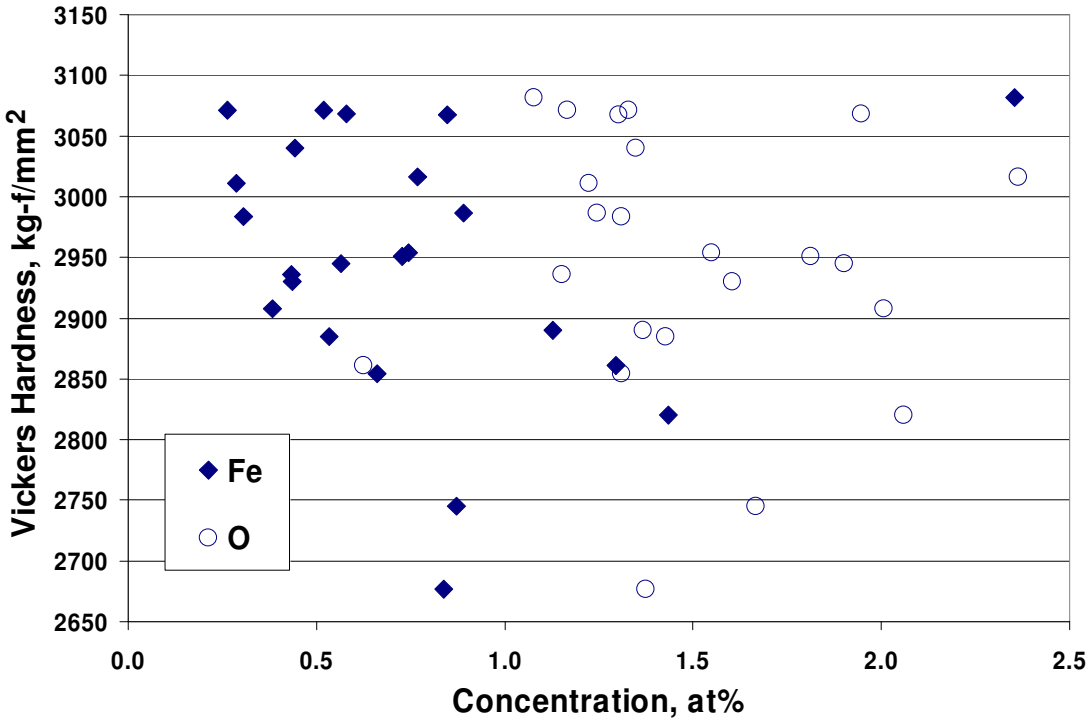

Figure 4.4: Vickers hardness versus both iron and oxygen concentration.

No direct correlation was found between the measured hardness and composition for all measured elements. Plots for other elements and for the Al/Mg ratio are not shown as they gave similarly low correlation with hardness. Linear regression for the data resulted in R^2 (correlation coefficient) values ranging from 0.0375 to 0.0025. Although each indent was measured at least 5 times there was still considerable deviation for each indent, on average around 100 VH. X-ray dispersive spectroscopy is less sensitive to

oxygen and boron, because they produce low-energy X-rays that are easily absorbed within the sample. This makes calibration difficult and complicates semi-quantitative data, especially for a boron-rich material such as this.

4.5: Discussion

It would appear that errors in both hardness and spectroscopy measurements were too large to enable any unambiguous correlation between the two. Porosity is another significant factor that may introduce scatter in the measured values. $AlMgB_{14}$ composites, such as the one examined in this study, typically contain between 1 and 5% porosity resulting from the dry-pressing of ultra-fine powder. The porosity is not evenly distributed, mostly as a result of powder agglomeration. This is the same reason impurities are not evenly distributed, and therefore there is likely some relationship between porosity and impurity distribution. Measuring local porosity in this material would likely prove very difficult, as most porosity is of the same scale as the grain size (less than 1 μm).

There may also be a direct relationship between Fe contamination and porosity. Fe introduced by milling is known to form FeB after hot consolidation, yet the concentration of FeB in the as-milled powders appears to be lower. If there is "free" Fe or lower iron borides present in the powder, they would melt at the pressing temperature of 1400ºC. This could contribute enough liquid phase to accelerate densification and reduce porosity, eventually reacting to form FeB. FeB is too refractory to melt at this temperature, but the benefit of reduced porosity may outweigh the reduced hardness caused by the presence of

FeB. This may complicate the correlation between Fe concentration and hardness if porosity is not measured and accounted for. Evidence that Fe may act as a sintering aid can be seen in Table 4.1 where Fe concentration in milled powders was measured by atomic emission spectroscopy. Planetary milling is a low-energy method in comparison to vibratory milling and results in $AlMgB_{14}$ powder with significantly less Fe contamination. $AlMgB_{14}$ consolidated from planetary milled powders have both lower hardness and density.

Table 4.1: Iron concentration and properties of $AlMgB_{14}$ consolidated from powder milled by two methods.

	Hardness	Density	Fe
Planetary Milled	24-32 GPa	94-97 %	1 wt%
Vibratory Milled	30-33 GPa	96-99 %	10.5 wt%

The EPMA is highly precise for most compositional analyses with precision errors typically less than 0.1%, though the error for boron can be around 0.5%. Accuracy is more dependent on calibration using standards of known composition. When studying boron-rich compounds, calibration becomes difficult because of absorption problems with characteristic boron X-rays. Aside from the expected error from WDS, surface contamination could be another complicating factor. $AlMgB_{14}$ is known to form a boron-rich oxide/hydroxide surface layer [89,110]. When using a wide-angle electron beam and a low accelerating voltage for X-ray spectroscopy, surface contamination can be a significant issue. A low accelerating voltage is required to prevent excessive absorption of weaker B and O characteristic X-rays, yet simultaneously also increases the fraction of X-rays from any surface layer. This is compounded by using a wide angle beam that

covers more of the surface. Sputtering the sample surface before analysis could be a solution, though the EPMA unit used in this study did not possess that capability.

Accurately measuring hardness also becomes increasingly difficult with exceptionally hard materials. The indentation size effect becomes significant in these materials if inadequate indentation loads are used [45]. This effect causes artificially high readings and increased error as indentation load decreases. At higher loads there is an asymptotic leveling of measured values where valid data can be recorded. Studies have shown that 1000 kg-f should be a sufficient load for baseline $AlMgB_{14}$ [14]. Indentation size is still on the order of 25 μm which can be difficult to measure precisely with an optical microscope. A higher indentation load would produce larger indents and measurement error would be reduced proportionately. Work is underway to perform similar experiments on this material utilizing a hardness indenter capable of higher indentation loads and with improved optics.

Despite the difficulties revealed in the current study, this method could still be useful in characterizing $AlMgB_{14}$-TiB_2 composites. The relative fractions of each phase on a local level should be easier to determine through the excitation of Al, Mg, and Ti. Impurities may not be detected as easily, but the inhomogeneity of TiB_2 distribution could be measured as well as phase size (not necessarily crystallite size) in an indentation region. Hardness is higher in these composites and therefore indents are smaller. Higher loads may be required to minimize error and the indentation size effect.

4.6: Acknowledgments

This work was supported by the U.S. Department of Energy, Office of Energy Efficiency and Renewable Energy, Industrial Technology Program. Ames Laboratory is operated for the U.S. Department of Energy by Iowa State University under Contract Number W-7405-ENG-82.

Chapter 5: Improved hardness and toughness of $AlMgB_{14}$ composites through addition of reinforcement phases

A paper published in *Proceedings of the 2005 International Conference on Powder Metallurgy & Particulate Materials*

Justin S. Peters[2], Bruce A. Cook[1], Joel L. Harringa[1],
Alan M. Russell[2], and Atiq Ahmed[3]

[1]Materials and Engineering Physics Program, Ames Laboratory, USDOE,
[2]Department of Materials Science and Engineering,
and
[3]Department of Mechanical Engineering,
Iowa State University
Ames, Iowa 50011

5.1: Abstract

Toughening of ultra-hard $AlMgB_{14}$ was explored through the addition of second phase reinforcements. The high hardness of $AlMgB_{14}$ combined with its low chemical reactivity with titanium and other metallic alloys makes these materials promising for high-speed machining, coatings, and other wear-resistant applications. However, actual performance to date has suffered as a result of low toughness. Initial machining and wear tests have had encouraging results and optimization of composition and microstructure of these composites is expected to result in additional performance benefits. High-energy milling was used to produce sub-micron powders that were consolidated into composites, some of which exhibited a maximum hardness of 46 GPa. Additions of TiB_2 have increased hardness, toughness, and erosion resistance. Improvements in fracture toughness will expand the array of possible applications for this material.

5.2: Introduction

Wear resistance of materials is not strictly a function of hardness. Toughness is the other determining factor for this property. The rate of erosion in single phase materials by impacting particles is inversely proportional to both the material's hardness and toughness as shown below:

$$V \propto K^m H^n \tag{10}$$

Where V is the volume of material removed and m and n have been experimentally determined to be around -1.3 and -.25, respectively [121]. Most hard material applications require wear resistance, such as in cutting, grinding, and protective coatings. Hard materials are brittle by nature and using these materials for many wear-resistant applications is often not sufficient. Toughness is increased by the addition of metallic binders, as in cemented tungsten carbide composites. It can also be improved to some degree by the addition of reinforcement phases, which may also be hard and are therefore not a great detriment to the composite's hardness.

Research has shown that the addition of TiB_2 to $AlMgB_{14}$ not only improves toughness, but hardness as well by way of a nanoscale microstructure, with maximum local hardness as high as 46 GPa [3,22]. An average hardness of 40 GPa combined with a mode I fracture toughness of 4 MPa$\sqrt{m}$ have been recorded simultaneously in samples with 70 wt% TiB_2 additions [69]. High-energy mechanical alloying has been used to produce fine-grained powder mixtures of $AlMgB_{14}$ and TiB_2, which were consolidated by pressure assisted reaction sintering. The entire range of $AlMgB_{14}$-TiB_2 composites have

been studied from 0% to 100% TiB_2. Neither hardness nor toughness of these composites was found to follow a simple rule of mixtures. Both reach a maximum around 50-60 vol% of TiB_2 [69].

These composites exhibit microstructures in the sub-micron and nanoscale range and the improved mechanical properties may be a result of effects similar to those proposed by Vepřek, et al [22,120]. This theory states that a nano-grained mixture of hard, insoluble phases can inhibit dislocation motion and flaw formation. Inconsistencies in powder processing lead to variations in both particle size and distribution of the reinforcement. Moreover, the presence of porosity, a common concern in the dry-pressing of ceramic powders, increases point-to-point variations in hardness and toughness and significantly reduces wear resistance. The purpose of this study was to examine some enhancements to the basic powder production process in an attempt to refine grain size and reduce the overall number of inhomogeneities in the composites.

5.3: Experimental

$AlMgB_{14}$ powders were produced by high-energy milling of elemental precursors prior to the addition of reinforcement phases. The materials were handled under inert helium or argon atmospheres during all stages of processing to minimize oxygen contamination. Additive-free $AlMgB_{14}$ powder, or baseline powder, was prepared by sealing stoichiometric quantities of B powder, Al wire, and distilled Mg (99%, 99.9999%, and 99.99% purity, respectively) in a hardened steel vial with three 8 g and three 1 g chrome steel milling media. Spex-8000 vibratory/oscillatory mills were used to comminute the

powder for 12 hours. TiB_2 powder was added either in as-purchased commercial form (Alfa-Aesar -325 mesh (99.5% purity)) or as produced by a 6 hour mechanical alloying of elemental Ti (99.5% purity) and B powder. The recovered baseline $AlMgB_{14}$ powder was weighed out along with the desired fraction of TiB_2 and sealed in an identical clean vial with milling media. The powder mixtures were then milled for an additional 30 minutes. The mixed powder was retrieved and loaded into a graphite die for hot-pressing. Consolidation was performed in a Centorr vacuum hot press under 106 MPa pressure for 1 hour at 1400ºC. Any modifications to the above procedures will be noted for specific samples.

The various samples produced were characterized for hardness, toughness, erosion resistance, and microstructure. Hardness and toughness were measured using a Wilson Tukon Vickers microhardness tester. Hardness was measured at a load of 1000 g and toughness was estimated using the Palmqvist technique shown in equation 2 [99]:

$$K_{IC} = 0.016\left(\frac{E}{H}\right)^{1/2}\left(\frac{P}{C^{3/2}}\right) \tag{11}$$

Where the indentation fracture toughness is related to the elastic modulus (E, GPa), the Vickers hardness (H, kg/mm^2), indentation load (P, N), and average crack length (C, μm). Density of each sample was measured by Archimedes displacement method. Porosity was calculated using estimates of impurity concentrations measured from previous samples.

Erosion testing was performed using an industrial abrasive grit blaster. 100 mesh alumina grit was used as the erodent which was characterized by electron microscopy as sharp, angular particles. Air pressure and impact angle were noted and reference samples of commercially produced cemented carbide cutting tool inserts were measured each time to quantify any variations in the equipment. Impact at a 90º angle to the surface is the most aggressive for brittle materials and was used for most of the erosion resistance measurements. For microstructural examinations, erosion was performed at a 45º angle to study both fracture and possible plastic deformation in the form of ploughing. Sample weight was measured before and after erosion and scaled to the exposed surface area of each sample, as the particle jet was larger than the samples' surfaces. Consecutive runs were done to ensure steady-state erosion, eliminating the effects of any surface treatment.

The microstructures were characterized using a JEOL 5910 LV SEM for imaging and observation of crack propagation and wear surfaces. Phase and impurity determination was largely performed by utilizing the energy dispersive spectroscopy (EDS) capabilities of the SEM. Verification of phases present was carried out by X-ray crystallography (XRD) to confirm proper phase formation when processing variables were changed, using a Scintag PadV X-ray diffractometer with CuK_{α} radiation.

5.4: Results

One generation of samples was produced to observe the effect of TiB_2 fraction in $AlMgB_{14}$. All samples were produced as described above using commercially available TiB_2. A 100% TiB_2 sample was also prepared by milling commercial TiB_2 for 30 min and

consolidated in the same fashion as the other samples to 95.6 % density. These samples were measured for hardness, toughness, and scratch and belt abrasion resistance in previous studies [69-70]. Figure 5.1 shows hardness and toughness as a function of volume % reinforcement. The highest hardness values were observed in the 70 wt% TiB_2 (approximately 60 volume %) samples and maximum toughness was shown with 60 wt% (50 vol. %) addition.

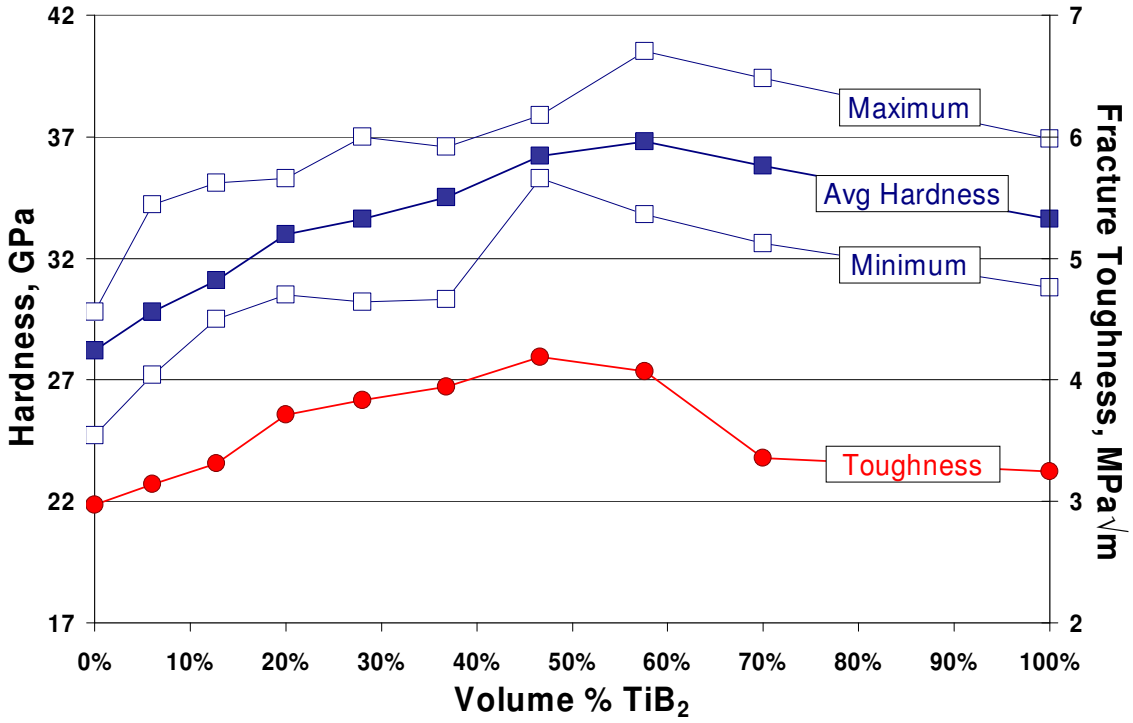

Figure 5.1: Vickers hardness and Palmqvist fracture toughness for $AlMgB_{14}$-TiB_2 composites [69].

Figure 5.2 below displays electron micrographs for samples produced by three different processing methods. The first three samples consist of 70 wt% TiB_2 addition, the composition in which the highest hardness values were recorded. Sample A was prepared with commercial TiB_2 as described earlier. Samples B and C were prepared with TiB_2 formed by mechanical alloying of the constituent elements. Sample C was

different from B in that it was consolidated from powder produced after multiple milling runs in which a considerable volume of the milling vial (estimated around 30 vol. %) was packed with dense agglomerate material. This agglomerate was expected to impair the motion of the milling media and therefore reduce their energy. As the micrographs of sample B and C suggest, there was some diminished capacity for particle size reduction with agglomerate present. Unlike the other samples, sample D was previously produced for comparison with earlier generations of $AlMgB_{14}$ composites and contains only 30 wt% TiB_2 [3]. Therefore its mechanical properties cannot be directly compared to the 70 wt% TiB_2 composites, but many of the microstructural features can be compared. The TiB_2 phase was also produced in an alternate manner than the other samples. Al, Mg, Ti, and B were weighed out for a stoichiometric mixture of $AlMgB_{14}$ - 30 wt% TiB_2 and milled together for 12 hours in the same fashion as described in the experimental section, with the intent of forming the TiB_2 phase in-situ during milling.

Samples from each production method were analyzed by X-ray diffraction to verify that the phases present were $AlMgB_{14}$ and TiB_2. They were also found to contain $MgAl_2O_4$ (spinel) and FeB. These phases are present in all mechanically alloyed $AlMgB_{14}$ composites to date, as O is introduced from the powder surfaces of the starting materials and Fe is picked up from wear debris from the vial and milling media during milling [101].

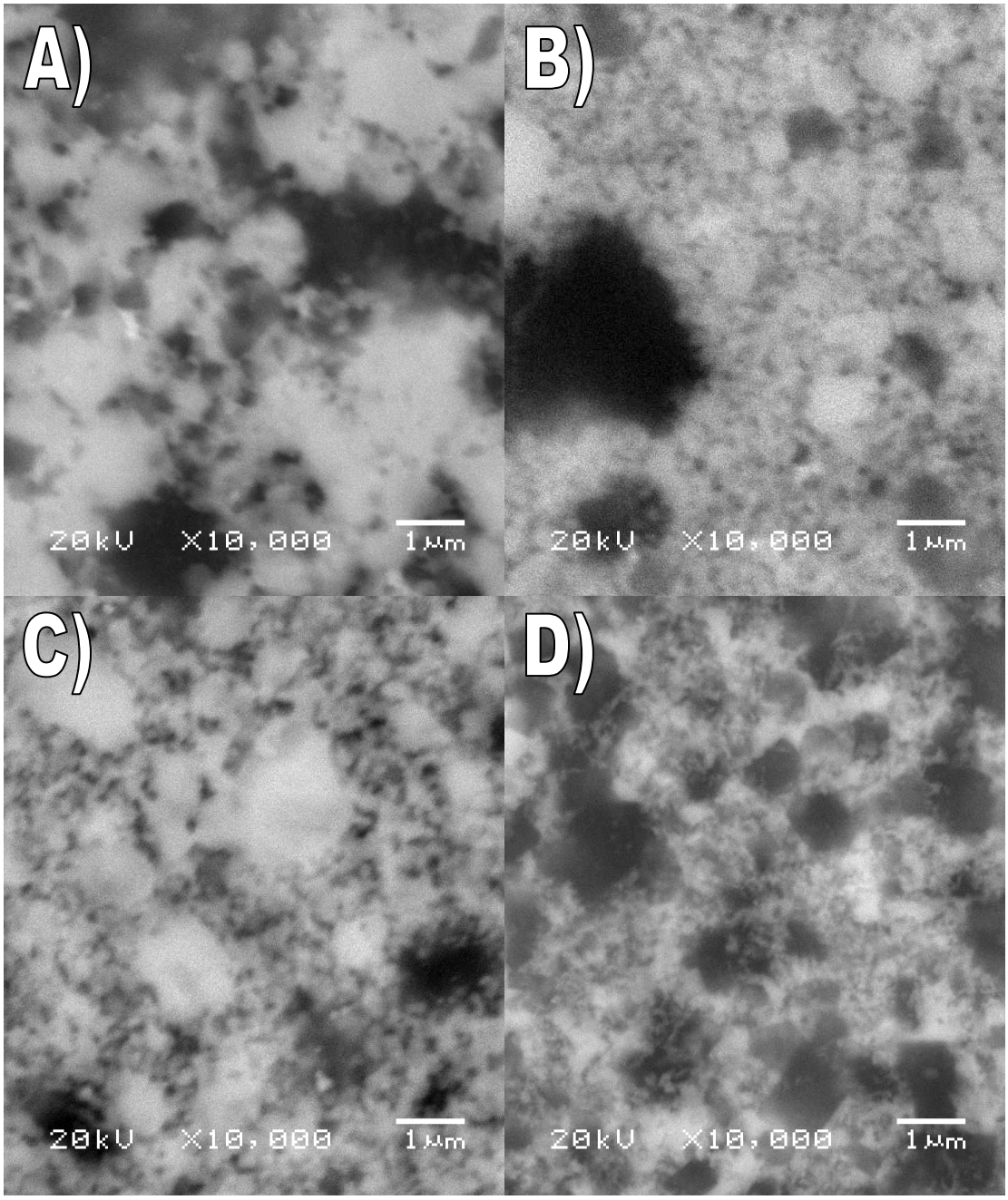

Figure 5.2: Backscattered electron images (BEI) of $AlMgB_{14}$-TiB_2 composites, white regions are TiB_2 and black or grey regions correspond to $AlMgB_{14}$. A) 70 wt% commercial TiB_2, B&C) 70 wt% MA TiB_2, D) 30 wt% TiB_2, MA simultaneously with $AlMgB_{14}$.

The above micrographs show some of the finer-grained regions in each sample, which do comprise the majority of each sample, but do not illustrate long-range variations seen at lower magnification. Figure 5.3 shows the range of inhomogeneity which results from

the different powder processing methods employed for samples A and D. Samples B and C are similar to A in homogeneity.

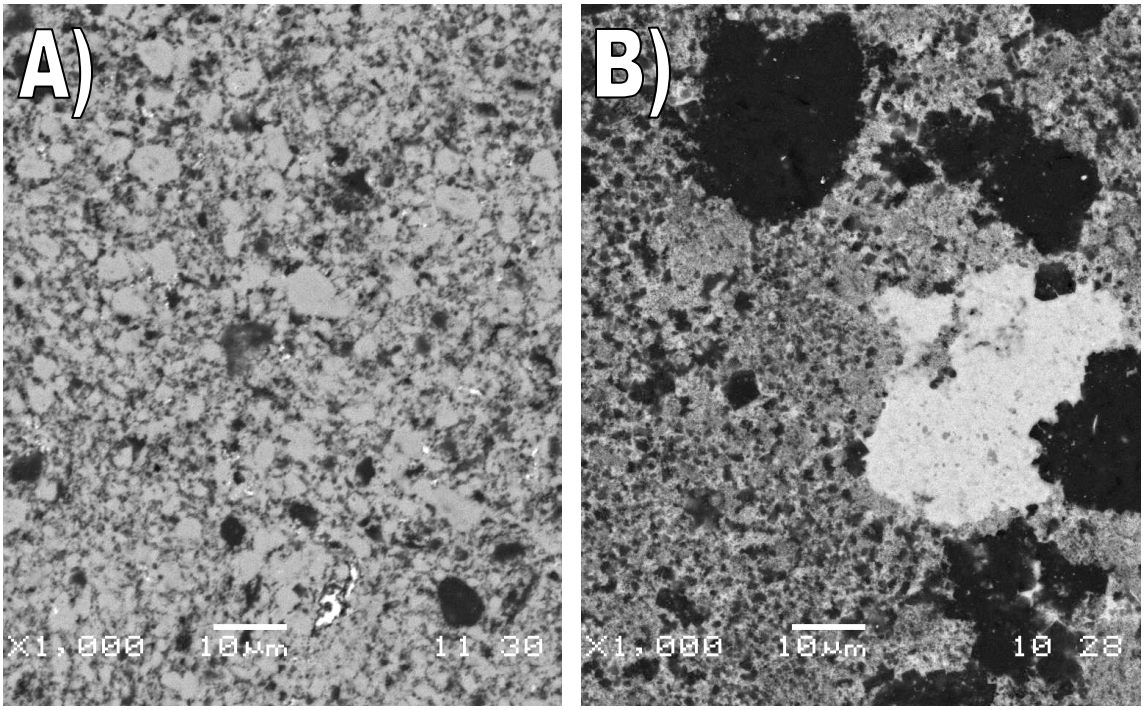

Figure 5.3: Backscattered imaging A) Typical microstructure from sample in figure 2A with average grain size ~1 µm. D) Inhomogeneous microstructure from sample pictured in figure 2D containing large agglomerated particles up to ~250 µm along with many grains ~100 nm.

Under observation by optical and electron microscopy, the finer-grained samples appeared to contain higher levels of porosity, although a quantitative determination of the relative porosity of the two classes of samples has not been attempted. As a consequence, microhardness values for the finer-grained samples produced with 70 wt% MA TiB_2 were not found to exceed those observed in samples prepared with 70 wt% commercial TiB_2; average hardness for samples prepared with commercial TiB_2 was around 3800 HV while the samples prepared with MA TiB_2 averaged around 3400 HV.

Density measurements by Archimedes displacement method resulted in similar densities for the sample sets produced with each TiB_2 source, averaging 96.3 % and 95.4 % of theoretical density for commercial and MA TiB_2, respectively. However, the Archimedes technique does not take into consideration the size and distribution of porosity; an equal volume fraction of porosity, uniformly distributed on a fine scale, is expected to degrade average hardness values more than a smaller number of larger pores. Obviously, regions of macroscopic porosity are avoided during microhardness measurements, while sub-micron porosity is more difficult to observe in typical microhardness optical systems. Moreover, theoretical density calculations accounted for average estimated concentrations of impurity phases since Fe and O impurity concentrations were only measured for baseline $AlMgB_{14}$ samples. Impurity concentrations likely differ in the $AlMgB_{14}$-TiB_2 composites and also vary with processing method.

Additional milling involved in the production of the MA TiB_2 is a probable source for excess Fe contamination. TiB_2 is also known to form readily by MA and would likely be very abrasive [122,82]. $AlMgB_{14}$ does not form in appreciable amounts by MA and the resulting powders would probably be less abrasive [71]. The Fe contribution from MA of TiB_2 may be very significant. The resulting FeB and $MgAl_2O_4$ phases are much softer than the major phases in the composite and are both known to be detrimental to its mechanical properties [101]. Chemical analysis will be required to determine if this is the case.

The source of the wide range of particle sizes in the $AlMgB_{14}$ - 30 wt% TiB_2 sample produced by simultaneous MA is not completely understood. Agglomeration probably plays some role, though incomplete milling or variations in powder retrieval may also contribute. Some techniques have been improved since the production of this sample and this technique should be investigated further, especially in the production of a 70 wt% TiB_2 composite.

The erosive wear resistance of these composites was also studied. As described earlier, testing was performed with a commercial grit blaster, in which engineering controls were implemented to ensure a high degree of reproducibility between tests. The calculated erodent velocity for this arrangement was 100 m/s, which is a factor of approximately five higher than the ASTM G76 standard. As wear is roughly proportional to velocity squared, the configuration employed in the current study is expected to generate 25 times the wear volume per unit time as compared with the ASTM test protocol.

The erosion rates of the $AlMgB_{14}$ - 70wt% TiB_2 composites were measured along with commercially available WC/Co cermets, polycrystalline diamond (PCD), and cubic-boron nitride (CBN), including one grade of CBN from Diamond Innovations designed for superior erosion resistance [89]. Figure 5.4 compares the erosion resistance of the commercial materials in addition to selected $AlMgB_{14}$-TiB_2 composites.

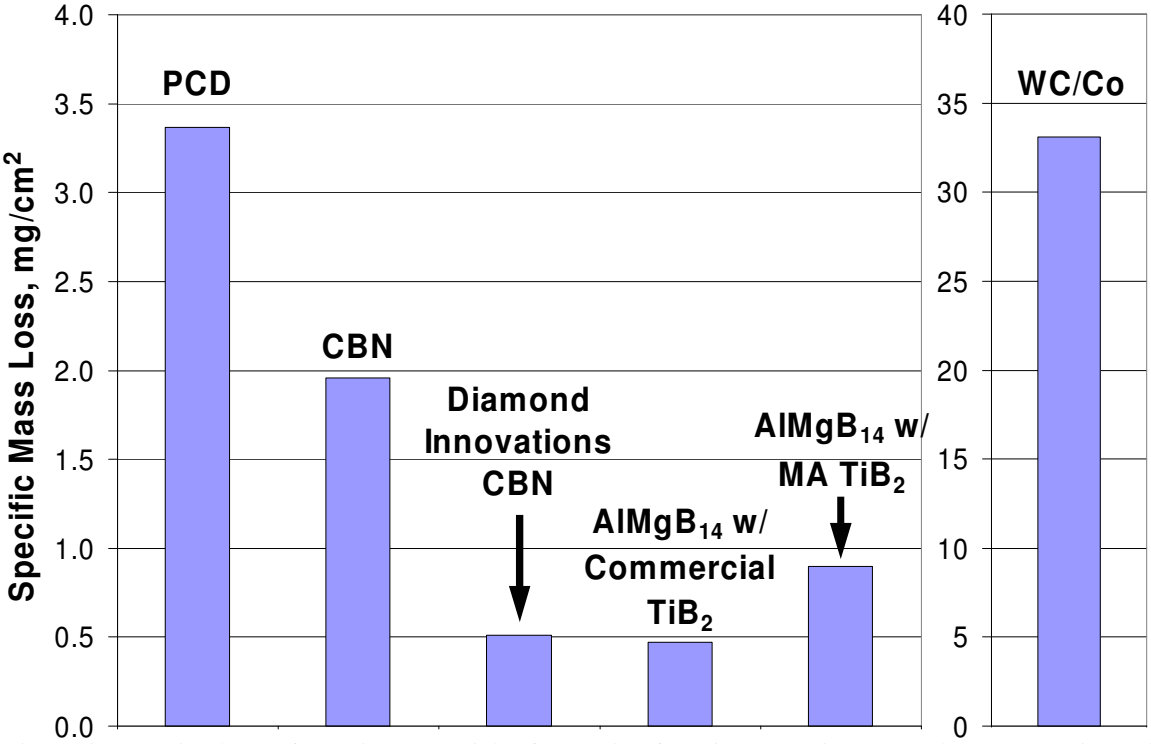

Figure 5.4: Erosion losses for various materials after 1 min of erosion at 90º impact angle. WC/Co pictured on a different scale as the erosion rate was an order of magnitude higher.

The fracture surfaces were also investigated in the SEM to examine the surface morphology and crack formation. The commercial WC and CBN exhibited large-scale fracture and grain ejection. The Diamond Innovations CBN did not display evidence of grain ejection, but was characterized by rough surface features. In comparison, the $AlMgB_{14}$ - 70 wt% TiB_2 composites possessed relatively smooth surfaces and exhibited flake-like material removal. The contrasting behavior between regular machining grade CBN and the $AlMgB_{14}$ - 70 wt% TiB_2 composites are shown in Figure 5.5.

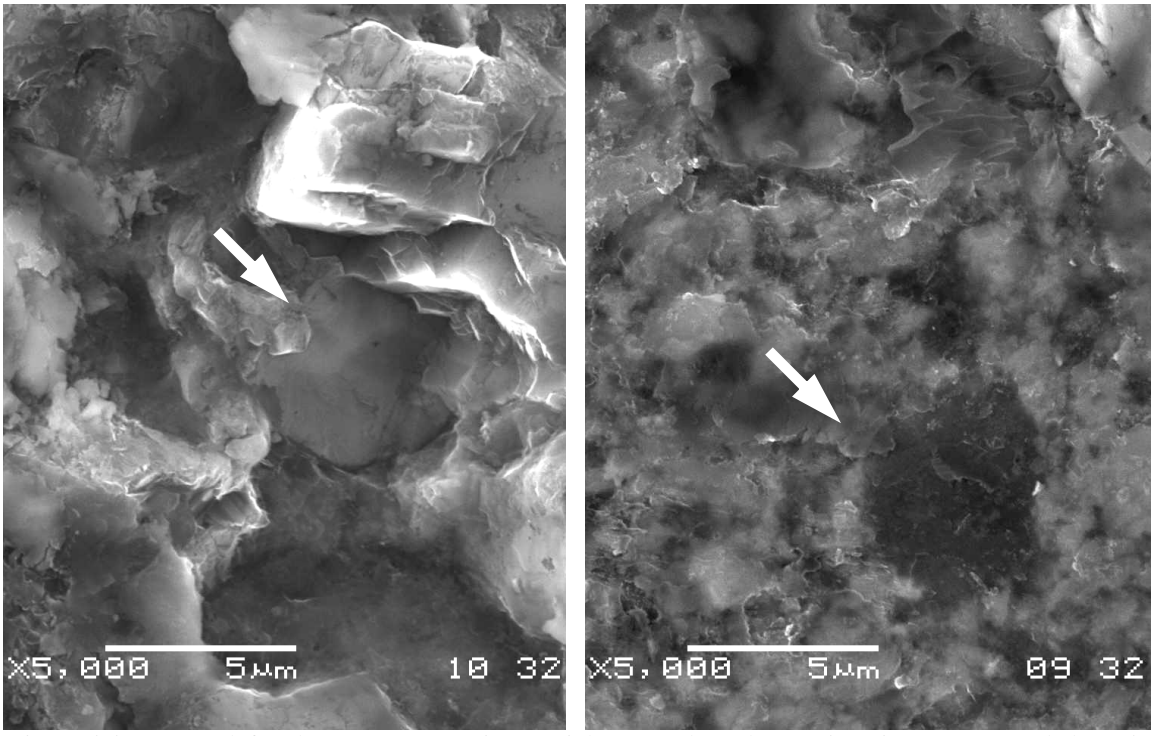

Figure 5.5: CBN on left, $AlMgB_{14}$-70wt% TiB_2 on right, secondary electron imaging (SEI). Eroded at 45º for several minutes to achieve steady-state erosion. CBN exhibits multiple fractures and grain ejection (marked). $AlMgB_{14}$-TiB_2 has a relatively smooth surface and flake-like fractures (marked).

Figure 5.6 illustrates other features observed in the eroded $AlMgB_{14}$ - 70 wt% TiB_2 composites. The image on the left shows what appears to be flow of material in the direction of the erosive jet. Boron-rich oxides form on the surface of these composites and impact at particle velocities of 100 m/s can induce local temperatures great enough to melt B_2O_3 [89]. A simple calculation relating kinetic energy of the incident abrasive particles to the quantity of heat deposited within the plastic deformation region at the point of impact suggests that localized temperature increases on the order of several hundred degrees are possible. Such temperature spikes are likely to form molten B_2O_3, which would flow as a result of momentum transfer from the gas and abrasive. Fracture within the bulk of the material was observed with backscattered electron imaging, and a few such fractures in TiB_2 are shown in the figure on the right. These cracks appear to be

deflected or arrested at $AlMgB_{14}/TiB_2$ boundaries, although any possible cracks within the dark $AlMgB_{14}$ phase would not be readily visible. Some evidence of plowing was also observed, but it is not certain whether it was only in the surface oxide layer.

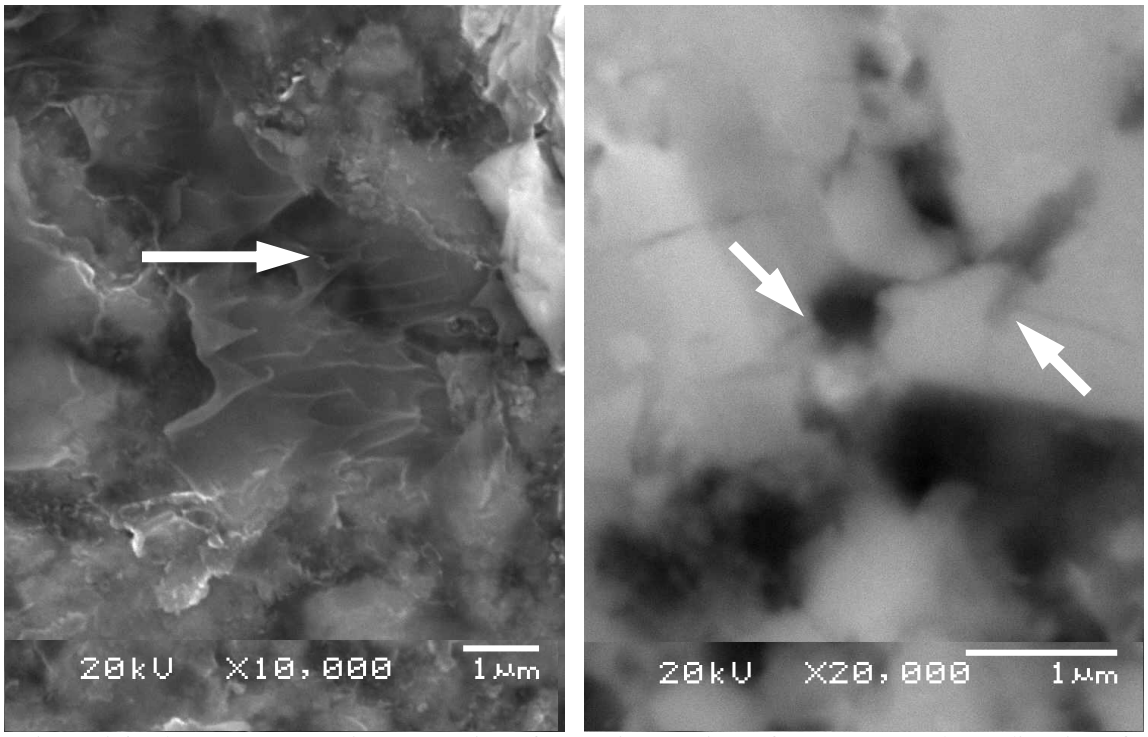

Figure 5.6: $AlMgB_{14}$-70wt% TiB_2 composites after erosion at 45º. Left: (SEI) arrow shows direction of erodent jet and molten oxide flow. Right: (BEI) transgranular fracture within TiB_2 grains, cracks possibly arrested or deflected at $AlMgB_{14}$ interface (marked).

5.5: Conclusions

Composites of $AlMgB_{14}$-TiB_2 exhibit microhardness and wear resistance higher than that of either constituent. The deviation of hardness and erosion resistance from that predicted by a rule of mixtures is attributed to the sub-micron microstructures observed in these samples, contributing "extrinsic hardness" as discussed by Vepřek, et al [22,120].

Various powder processing routes have been examined for addition of TiB_2 to $AlMgB_{14}$, including use of commercial powder and in-situ reaction during the mechanical alloying of $AlMgB_{14}$. The latter was shown to result in an extremely fine distribution of second phase reinforcement; however, the presence of microscopic porosity and contamination phases obviated the expected increase in hardness. Erosive wear resistance of these composites was found to be superior to cemented carbide, and comparable to, or slightly better than cubic BN. With further processing improvements to eliminate porosity and reduce impurities, it is reasonable to expect these materials to achieve even higher levels of wear resistance.

5.6: Acknowledgments

This work was supported by the U.S. Department of Energy, Office of Energy Efficiency and Renewable Energy, Industrial Technology Program. Ames Laboratory is operated for the U.S. Department of Energy by Iowa State University under Contract Number W-7405-ENG-82.

Chapter 6: Microstructure and wear-resistance of mechanically alloyed TiB_2

A paper to be submitted to *Wear*

J.S. Peters[1,2], B.A. Cook[2], J.L. Harringa[2], A.M. Russell[1,2], and N. Oster[1]

[1]Department of Materials Science and Engineering and
[2]Ames Laboratory Materials and Engineering Physics Program,
Iowa State University, Ames, IA 50011 USA

6.1: Abstract

Fine-grained TiB_2 compacts have been hot pressed to 98-99% theoretical density at 1400 to 1500ºC. The compacts were consolidated from sub-micron-sized powders prepared by a high-energy ball milling technique. TiB_2 powders were produced from both the milling of commercially synthesized TiB_2 and from the mechanical alloying of Ti and B precursors. The formation of TiB_2 from Ti and B powders by mechanical alloying was found to reach completion after 3 hours, and wear debris from steel mill vials and media used in the processing introduced 0.8 to 1.5 wt% Fe in the sintered compacts. The dry erosion resistance of the highest density compacts was examined using an abrasive jet of Al_2O_3 impinging at a normal angle incidence. Steady-state erosion rates of 5 $x10^{-4}$ mm^3 per gram of erodent compare favorably with the measured value of 90 $x10^{-4}$ mm^3/g for commercial, fine grained WC-Co cermets under identical conditions. Microstructures, fracture surfaces, and erosion craters were also examined by electron microscopy.

6.2: Introduction

Titanium diboride (TiB_2) is particularly useful for a variety of high-temperature applications due to its high hardness, high modulus, high electrical and thermal

conductivities and its exceptional corrosion and erosion resistance in many environments. The difficulty in forming TiB_2 components is the major reason for its high cost and limited scope in engineering applications. Due to the refractory nature of this material, high-temperature powder consolidation methods such as HIP or hot-pressing are generally required. In order to obtain nearly fully dense material, sintering temperatures of 1800ºC or higher are usually needed unless large additions of sintering aids, especially metallic, are used [63-64,66-68,123-125]. Studies have shown that small additions of Si_3N_4 or metallic elements such as Fe or Ni perform exceptionally well at reducing the temperatures and pressures required to sinter TiB_2 to near 100% density [102,126]. TiC and TiN additions are common in the sintering of TiB_2, usually in high concentrations, because they aid in sintering while inhibiting grain growth due to their immiscibility in TiB_2 [63,65,85]. Oxygen contamination has been shown to have detrimental effects during the sintering process, because of its effect on grain coarsening and retention of porosity [102,127].

Formation of TiB_2 by mechanical alloying (MA) of the constituent elements has been reported, requiring milling times ranging from 1 to over 100 hours [82-83,122,128]. Milling time is largely dependent on impact energy and frequency, which vary by mill type and media mass. The transformation of elemental Ti and B to TiB_2 is generally accompanied by a sudden temperature increase during which the reaction occurs quickly by combustion synthesis, also known as a mechanically-induced self-propagating reaction, or MSR [78,80]. When the constituent elements are heavily comminuted and the activity is increased by deformation, the activation energy is lowered, and the reaction

can become self-sustaining when initiated by the heat generated during an impact event [79-80].

Most research involving the wear resistance of TiB_2 has focused on TiB_2 with appreciable amounts of binder phase or with TiB_2 as a reinforcement phase for a softer ceramic or alloy [126-132]. The presence of only a few percent porosity in monolithic TiB_2 has been shown to have a significant impact on erosion resistance. In addition, the high sintering temperatures required for densification can lead to grain growth that can be detrimental to wear properties [133]. Reduced temperature densification of TiB_2 would be desirable if porosity could be minimized, because of the enhanced wear resistance accompanying retention of the fine-grained microstructures.

6.3: Experimental Procedures

The TiB_2 powders for this study were prepared by milling of high-purity powders in a He atmosphere. Spex-8000 vibratory/oscillatory mills were used to comminute the powders in sealed, hardened steel vials with chrome steel milling media (three 1 gm and three 8 gm balls). Two types of powders were prepared, the first consisting of Aesar -325 mesh TiB_2 (99.5 % purity, metals basis) which was mechanically milled (MM) for 30 minutes to reduce the particle size. Other powder was prepared by MA for 6 hours of Ti (Aesar -325 mesh, 99.5 % purity, metals basis) and amorphous B (Atlantic Equipment Engineering 99 % purity, metals basis, vacuum out-gassed at 1400ºC). All powder handling occurred under He atmosphere in a glove box to minimize oxygen contamination. Samples of the MA TiB_2 were obtained at 0.5, 1, 2, 3, and 6 hours of

processing to monitor the formation of TiB_2 by X-ray diffraction (XRD). The powder morphologies were also examined by scanning electron microscopy (SEM) and energy dispersive spectroscopy (EDS). Analysis of Fe contamination from milling was performed by NSL Analytical by inductively coupled plasma (ICP) mass spectrometry.

Powder consolidation was performed in a Centorr hot press in graphite dies under a flowing Ar atmosphere. The dies were lined with boron nitride and graphite sheet as lubricants. Powder samples of both MM and MA TiB_2 were pressed at 1300, 1400, and 1500ºC for 1 hour under a pressure of 106 MPa to produce 12.7 mm diameter compacts. To ensure smooth and parallel sides, the compacts were faced with a diamond grinder before polishing and subsequent characterization.

Density was determined by the Archimedes displacement method, except for the lowest density samples for which the porosity was interconnected. In this case, density was estimated by direct measurement of sample dimensions and mass. Impurity phase concentrations were included in the theoretical density calculations for an accurate representation of residual porosity. Hardness was measured by Vickers microindentation, and toughness was estimated from the resulting cracks by the Palmqvist method [100]. Indentation was performed with a Wilson-Tukon Vickers microhardness tester at a load of 1000 gm. Elastic modulus was measured by ultrasonic transmittance between the parallel faces of the sample. XRD was employed to verify formation of the TiB_2 phase, and microstructure and impurities were analyzed by SEM and EDS. All aforementioned characterization was performed prior to erosion testing.

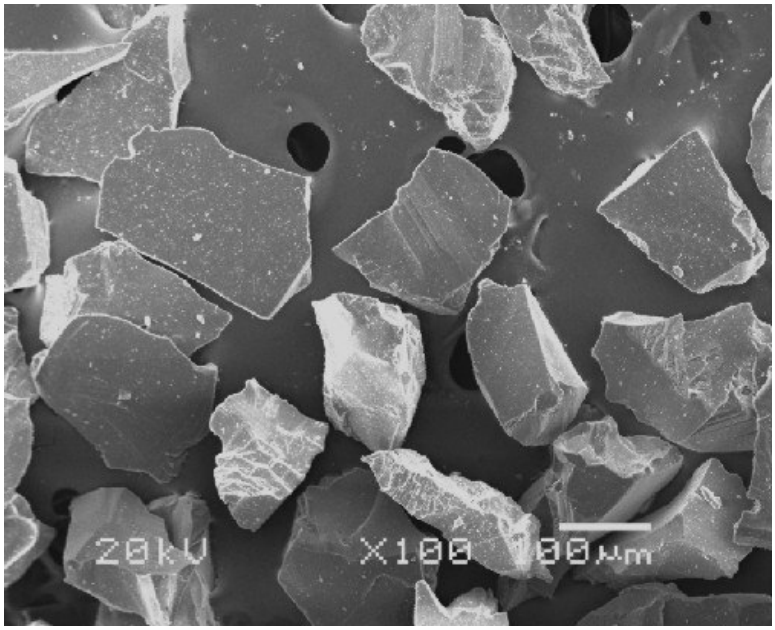

Figure 6.1: Secondary electron image of +100 µm Comenco Al_2O_3 grit.

Erosion resistance of the samples was measured by mass change after exposure to a high-velocity abrasive jet in accordance with ASTM G 76 procedures. Alumina grit (+100 µm, Comenco) was entrained in a regulated, compressed air stream. Electron microscopy revealed that the average particle diameter was closer to 200 µm and highly angular, which acts as a more aggressive erodent than rounded particles (Figure 6.1). Impact angles were maintained perpendicular to the sample surface at a distance of 1 cm, and the particle velocity was approximately 77 m/s, as measured by high-speed digital photography [89]. Impact normal to the sample surface was chosen because it results in the highest wear rates for materials that fail primarily by brittle fracture [92]. The impact area was smaller than the sample surface to ensure that all of the particles impacted the sample. To maintain consistent erosion conditions, abrasive grit was collected and not reused. Mass change was measured at 30 and 60 minute intervals over a total of 4 hours

of erosion. The total mass of erodent during each interval was also recorded so that the ratio of mass loss to erodent mass could be calculated.

After erosion testing, the resulting wear craters were examined by SEM. Surface roughness, material removal mechanisms, and sub-surface fracture were investigated. Additionally, samples were fractured for examination of clean fracture surfaces with SEM.

6.4: Results

The milled TiB_2 powders showed good uniformity in particle size and morphology. The MM TiB_2 powder prepared from -325 mesh TiB_2 crystallites contained many angular particles. The material produced by MA on the other hand was comprised primarily of more rounded particles. Some of the MA powder appeared to consist of agglomerates of much finer particles. As seen in Figure 6.2, the particle sizes in both powders range from a few micrometers to under 100 nm. Fe content was measured by ICP analysis to be 0.86 wt% in the MM powder (milled 30 minutes) and 1.55 wt% in the MA powder (milled 360 minutes).

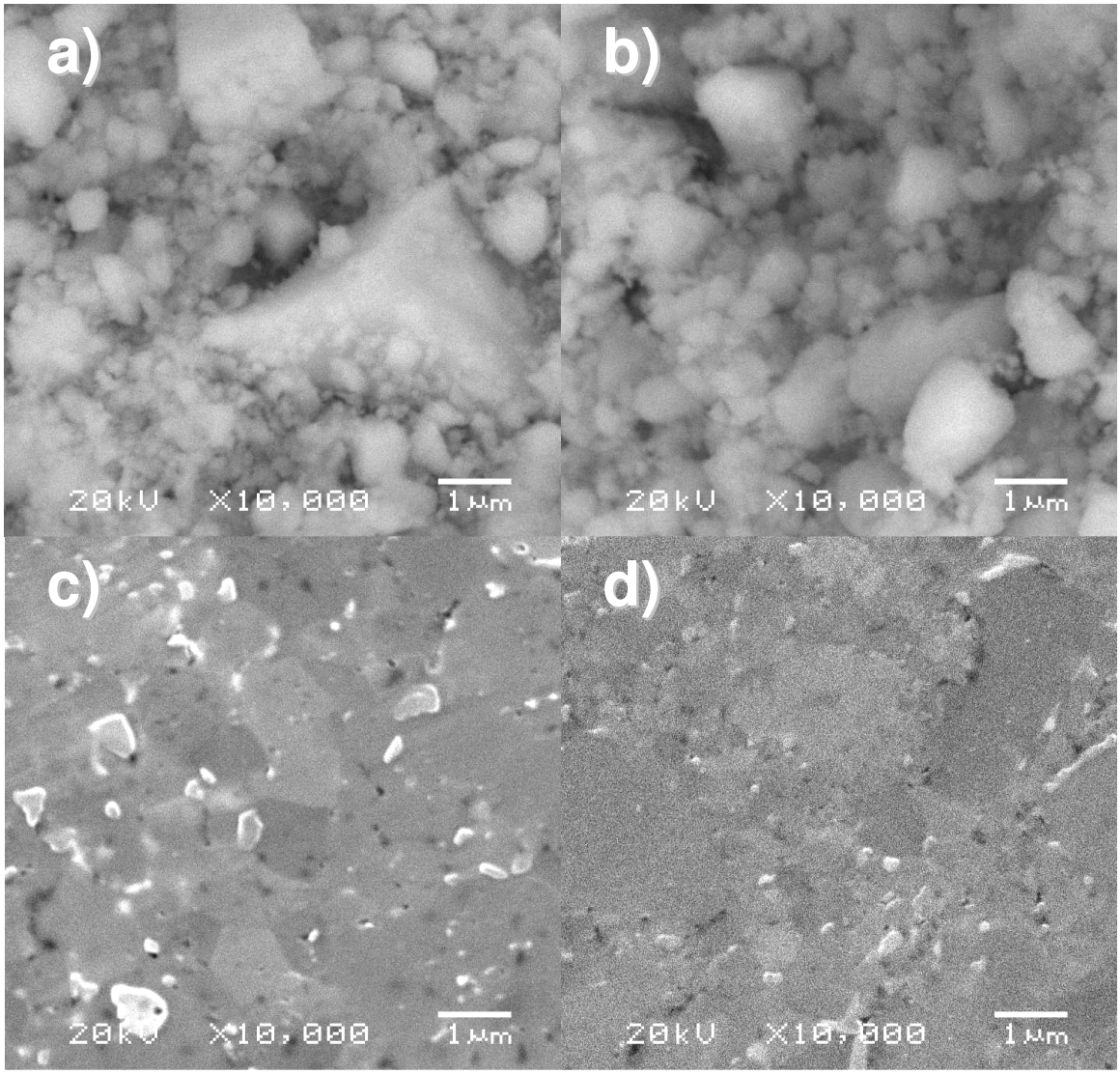

Figure 6.2: SEM micrographs of MM (left) and MA (right) TiB_2 before hot pressing (upper photos) and after hot pressing (lower photos).

As shown in Figure 6.3, the MSR of Ti and B reached completion between 2-3 hrs of milling. The temperature of the powder was not measured during milling, but a spontaneous reaction is expected to have occurred. This is inferred from the absence of TiB_2 peaks after 2 hrs of milling and the complete conversion to TiB_2 after 3 hrs. Such MSRs have also been reported previously for this system [85,128].

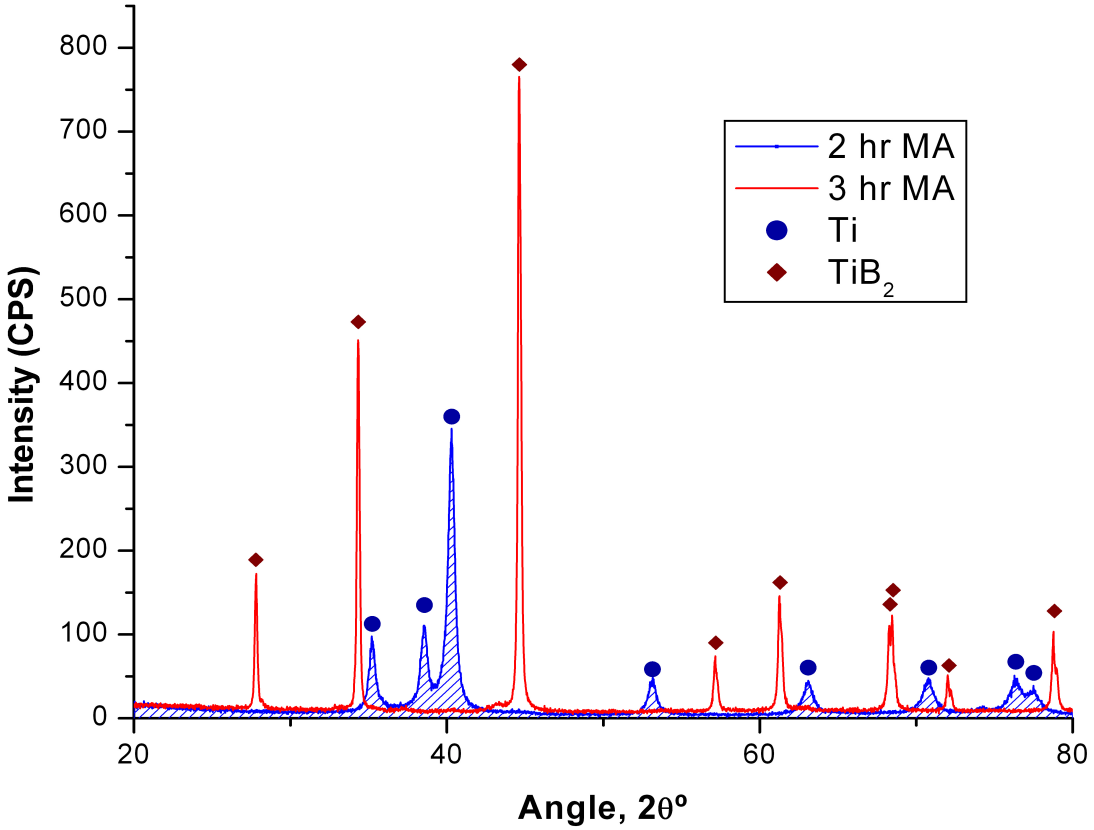

Figure 6.3: XRD patterns of MA powder samples taken before and after combustion synthesis reaction (MSR). Boron peaks are not visible in the pre-synthesis pattern due to the use of amorphous B.

Figure 6.4 shows the progression of the alloying of the MA powder before and after MSR. Note in Figure 6.4(a) that fine B particles (dark) are evenly embedded in a Ti matrix (bright). After MSR, the TiB_2 particles are quickly reduced in size, as shown in Figure 6.4(b), although 3 additional hours of milling are required to achieve the grain refinement shown in Figure 6.2(b).

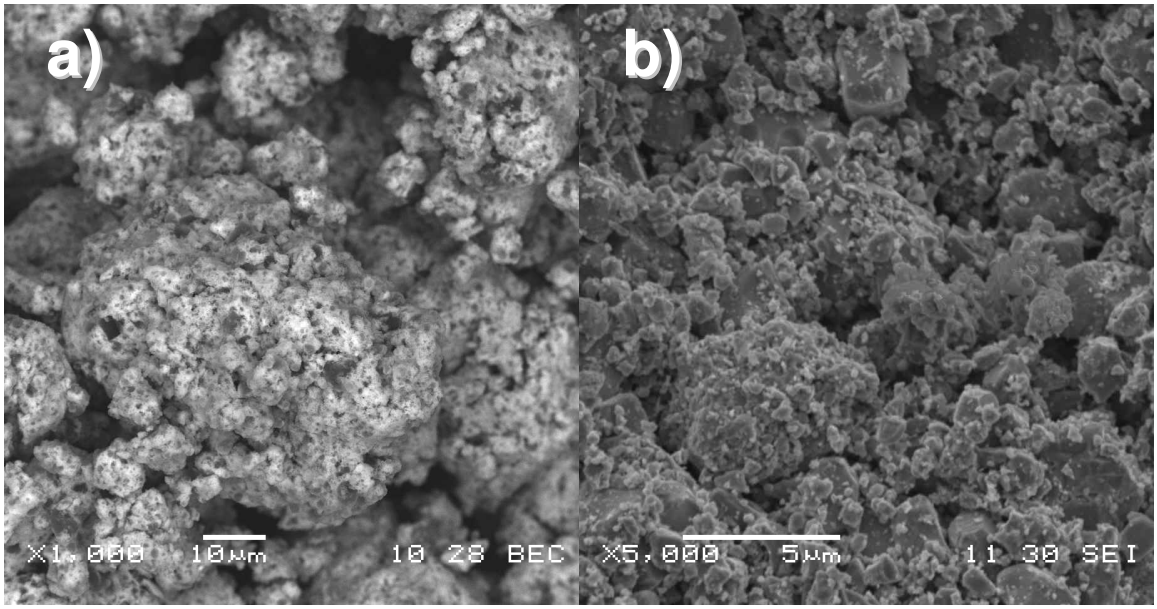

Figure 6.4: (a) Backscattered image of MA before MSR (2 hrs) and (b) secondary image after MSR (3 hrs). Note: not at same magnification.

Hot pressing of the packed powder resulted in densification to as much as 98.9% of theoretical density. There is a noticeable increase in density accompanying an increase in hot pressing temperature from 1300ºC to 1400ºC, and a further, albeit slight increase between 1400ºC and 1500ºC. Mechanical properties measured for these samples are summarized in Table 6.1. As expected, elastic modulus and density were closely correlated. For these samples, the major impurity phase visible by XRD (not pictured) was a mixed Ti(C,N) phase. Diffraction peaks for Fe- or O-rich impurity phases were not detected, though EDS suggests that Fe may be soluble in the Ti(C,N) phase. It has also been reported that Fe is partially soluble in the TiB_2 lattice, concentrated near the grain boundaries and causing lattice distortion [134].

Table 6.1: Density (ρ) both measured and % of theoretical, Vickers microhardness (H_V, kg/mm^2), plane strain fracture toughness (K_{IC}, MPa√m), Young's modulus (E), and Erosion Rate (mm^3/kg) for samples hot-pressed at 106 MPa pressure from MA or MM powder at various temperatures (T).

T (ºC)	Source	ρ (g/cm^3)	ρ (%)	H_V	K_{IC}	E (GPa)	Erosion
1300	MA	3.94*	87% *	*	*	357	*
1400	MA	4.438	97.9%	2915	2.5	479	0.51
1500	MA	4.470	98.6%	2807	2.7	510	0.67
1300	MM	4.14*	92% *	*	*	465	*
1400	MM	4.462	98.8%	3091	2.5	509	0.75
1500	MM	4.468	98.9%	2682	2.7	500	2.19

Note: Density (ρ) calculated by Archimedes method except when too porous (*), in which case density was estimated from sample dimensions. Hardness (H_V) and toughness (K_{IC}) by Vickers microindentation at 1kg and Palmqvist method, respectively. Samples marked * were also too porous for polishing and indentation. Young's modulus (E) determined by ultrasound.

Samples were also pressed from MM powder under varying conditions to examine the effect of a single processing variable on densification. One sample was hot-pressed at 1400ºC from MM powder at 35 MPa, as opposed to 106 MPa for the remaining samples. This was done for closer comparison to the results of other researchers [64,102,126]. Two additional samples were hot-pressed at 1400ºC and 106 MPa using different die liners. The first was hot-pressed in a die with a thick BN spray coating to inhibit C diffusion from the graphite die. The second employed only graphite foil as a lubricant, eliminating any source of N. The differences in these samples are listed in Table 6.2.

Table 6.2: Comparison of change in density of hot-pressed MM TiB_2 compacts by varying pressure or liner materials.

T (ºC)	Source	P (MPa)	Liner	ρ (g/cm^3)	ρ (%)
1400	MM	106	C, BN	4.462	98.8%
1400	MM	35	C, BN	4.248	92.8%
1400	MM	106	BN	4.402	97.5%
1400	MM	106	C	4.395	97.3%

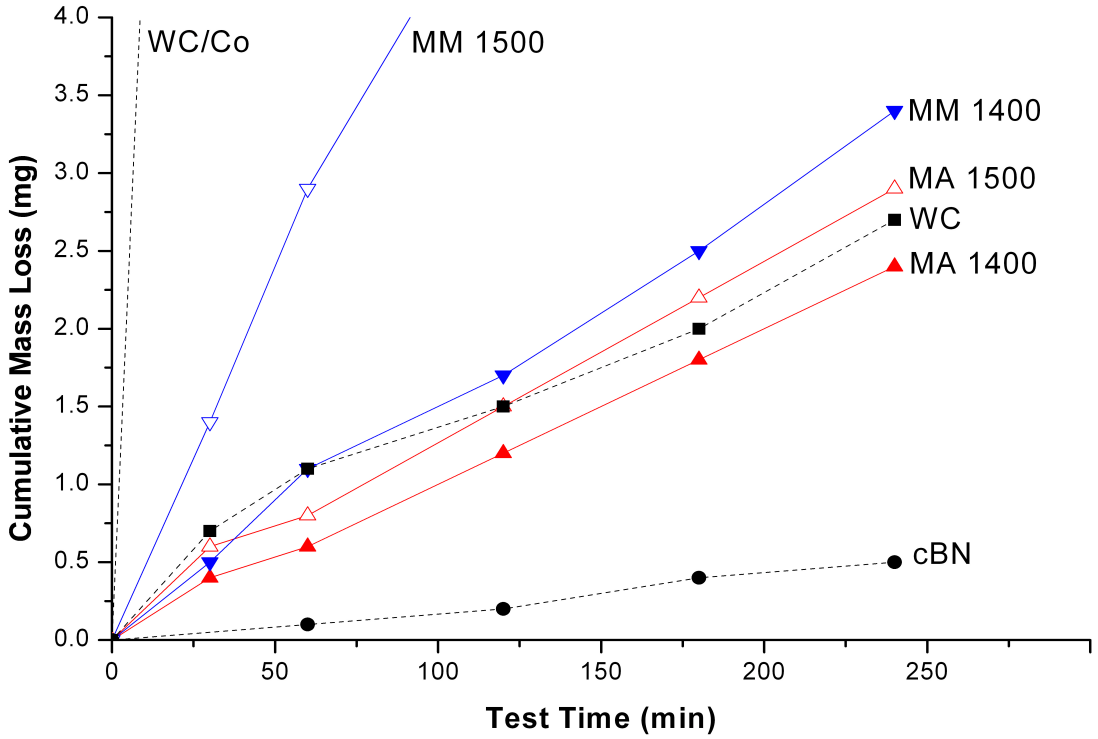

Figure 6.5: Erosion rates of TiB_2 and commercial WC and CBN samples. Erosion test conditions were held at 90º incident angle at 1 cm from sample surface, abrasive flow rate of 4 g/min, and 77 m/s particle velocity for all samples.

Steady state erosion rates of the TiB_2 compacts hot-pressed at 1400 and 1500ºC are included in Table 6.1. Figure 6.5 compares mass loss rates to those of selected commercial materials under the same conditions. The WC and WC-6wt% Co (RocTec 500 and K68 grade, respectively) were obtained from Kennametal, while the CBN insert was a Borazon 7000 tool obtained from Diamond Innovations. The wear surfaces of the TiB_2 samples were also investigated by SEM after erosion, examples of which can be seen in Figure 6.6. Surface roughness from grain ejection is visible, along with examples of intergranular fracture and microcracking.

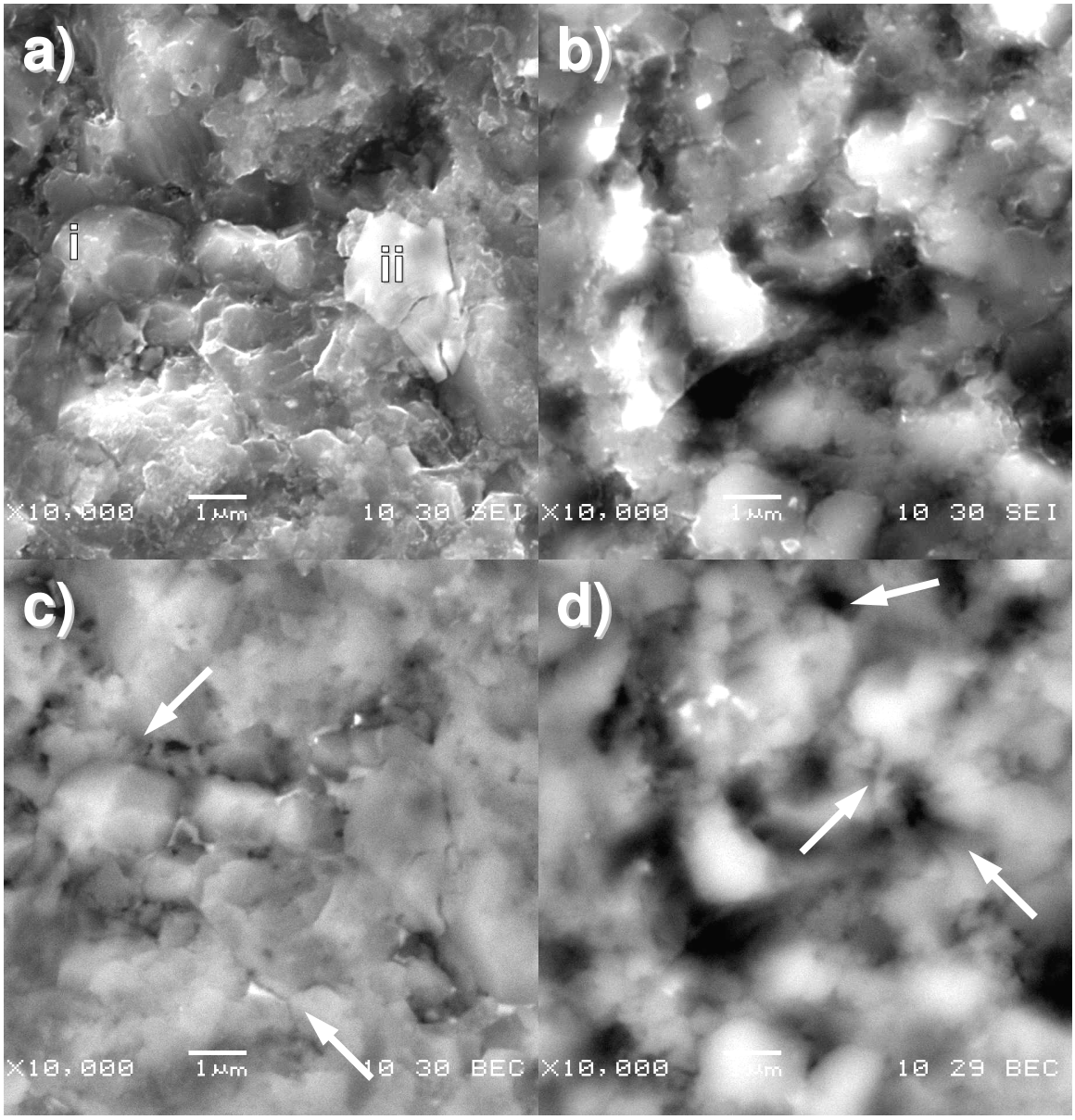

Figure 6.6: SEM micrographs from center of erosion crater of 1500ºC MM (left) and 1400ºC MA (right) TiB_2 samples, both hot-pressed at 1400ºC. Secondary images (top) show surfaces from intergranular fracture (i) and a partially dislodged grain (ii). Backscattered images (bottom) reveal microcracking (indicated by arrows).

6.5: Discussion

The ability to sinter TiB_2 to nearly 99% density at 1400 to 1500ºC can be attributed to a number of factors which result from processing the powders by high-energy milling. The fine grain size is critical, especially the range of particle sizes down to nanoscale sizes,

which can improve the fill ratio of a cold-pressed compact. In addition, milling under an inert atmosphere produces clean, oxide-free surfaces that have a high activity and are more readily sinterable [57]. For comparison, attempts to sinter un-milled -325 mesh TiB_2 resulted in highly porous, low-strength compacts.

Another benefit of the high-energy milling technique is that the small amount of Fe introduced from the steel media acts as a sintering aid. Chemical analysis shows that even with approximately half the Fe concentration, the MM powder still sintered to slightly higher densities. In many cases, large amounts of metallic binders are added to TiB_2 powders to aid in sintering, often exceeding 10 wt% [67-68,124-125]. It has been shown that less than 1 wt% of metallic additive can have a significant effect on sinterability at lower temperatures [102]. While lower sintering temperatures were employed in this study, Table 6.2 shows that higher pressure substantially improves densification. The agglomerates resulting from the increased attractive forces of sub-micron powders require higher pressure to achieve deformation and rearrangement of clusters before and during the necking stage of sintering. Sintering to high density at 1400ºC is significant, because this temperature corresponds to only 48 % of the 3498 K absolute melting temperature of TiB_2 [135].

C and N impurities in TiB_2 powders have both been shown to enhance sinterability, with free C having the added benefit of gettering O contamination and being able to diffuse from a graphite die [65,102,127]. TiN and TiC have also both been shown to impede grain growth during sintering [65,85,102]. While C and N concentrations were not

measured in the powders, Table 6.2 shows that limiting diffusion of either element can have an effect on densification. Although similar densities resulted from contact with only C or BN, C likely has a greater effect since diffusion could not be eliminated by using a BN liner, as was shown by the presence of TiC in all samples by XRD. It is unknown what effects the C concentration profile through the thickness may have on the wear properties of the compacts as testing was done near the surface.

Microstructure.

Milling of commercial TiB_2 and MA of Ti and B resulted in similar powders. Likewise, material hot-pressed from both sources had similar microstructures and comparable hardness, toughness, and modulus values. However, minor differences resulted in significant changes in erosion resistance. As shown in Figure 6.2, impurity phases (brighter) appear to be more pronounced in the MM material. Significant differences in concentration of Ti(C,N) impurities could not be resolved between MM and MA TiB_2 by XRD. Figure 6.7 shows similar MM material hot-pressed at 1500ºC. Two distinguishing characteristics are most notable; grain size and pore size have both increased significantly over material sintered at lower temperature. Both weaker impurity phases and larger pores act as stress concentrators and can promote crack propagation. Large grain size is also detrimental to erosion resistance [97].

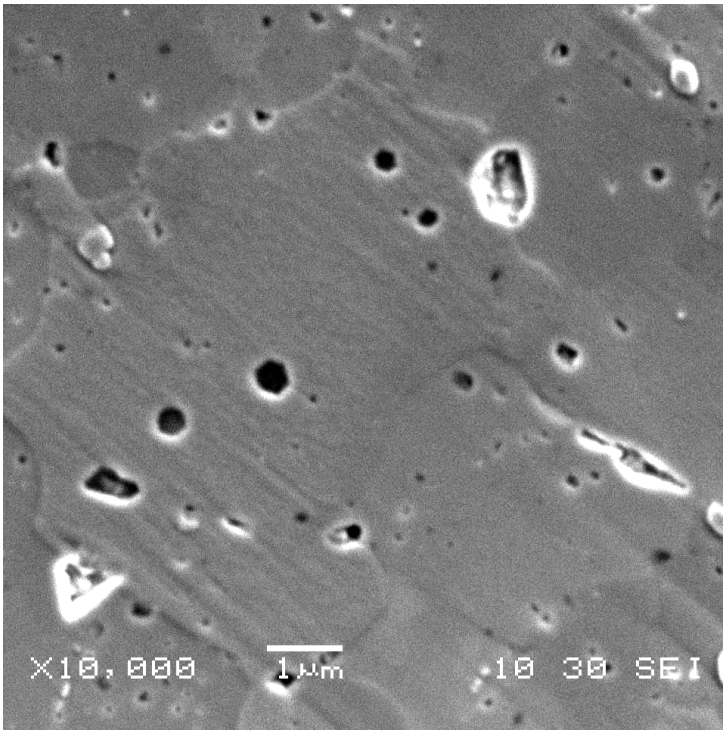

Figure 6.7: MM TiB_2 hot-pressed at 1500ºC, exhibiting interior pores (dark) and pores between grains (bright).

Erosion.

The surface roughness visible in Figure 6.6(a) is largely the result of grain ejection caused by deeply penetrating cracks. Microcracking is visible in the larger grains and probably penetrates the entire width of each grain. This relates to ejection of larger pieces of material and more deeply penetrating microcracks, both of which promote higher material removal rates. Fine grains can disperse a crack closer to the surface, resulting in greater absorption of energy and removal of material in thin layers, as in Figure 6.6(b) which shows less pitting. Pressing at 1400ºC preserves the finer grains produced by milling, further refinement of the ~1 μm sized grains in both the MA and MM TiB_2 would be expected to improve wear resistance [97,133]. A key factor in

increasing erosive impact resistance is maximizing the damage and deformation (and therefore the energy absorption) a region can sustain before particles detach.

The benefit of finer grains is significantly reduced if intergranular fracture dominates. Fracture along weak grain boundaries reduces the energy absorption by crack deflection in the fine-grained regions during erosion and also allows cracks to penetrate more deeply. TiB_2 pressed at 1500ºC shows some coarsening, but the most significant factor in the difference in erosion performance between MM material hot-pressed at 1400 and 1500ºC may be the distribution of impurity phases. Figure 6.8 shows 1500ºC MM after 4 hrs of erosion at the site of a pit caused by grain ejection. Ti(C,N) impurities are clearly visible along the grain boundaries in Figure 6.8(b) and also in Figure 6.6(a) near the site of intergranular fracture. Gu, et al report that TiN additions improve grain boundary strength and reduce intergranular fracture [65]. It may be that lattice strain caused by C and Fe reduce the coherency of TiN. As mentioned earlier, O contamination can lead to enhanced grain growth and inhibit the removal of porosity [102,127]. Note the difference in appearance of pores within the grain and along the grain boundaries in Figure 6.7(b). The brighter contrast of the intergranular pores is due to the charging of surface oxides, indicating the migration of O impurities to the boundaries as well. The interior pores are also clear and faceted, while the boundary pores have rough surfaces likely from impurity phases. Obviously, the large intra- and intergranular pores will also have an effect on the material's structural integrity.

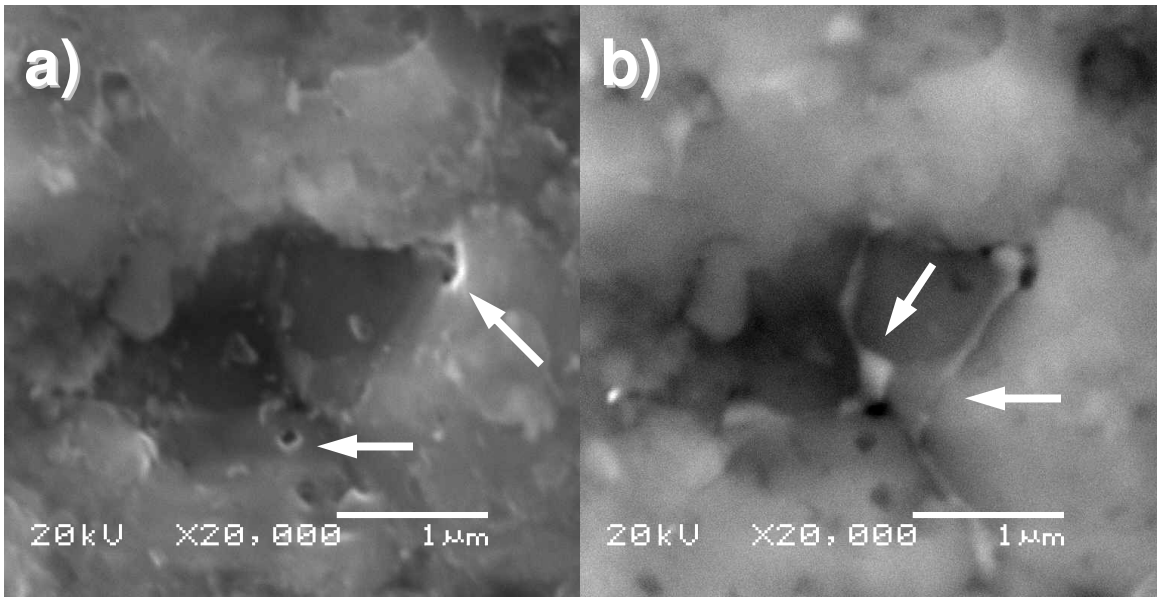

Figure 6.8: Secondary (a) and backscattered (b) electron images of the same region of an erosion crater from 1500ºC MM TiB_2 after 4 hr erosion. Arrows indicate pores in (a) and impurity phases (bright) visible along the grain boundaries in (b).

Fracture.

Samples fractured by impact (Figure 6.9) support previous observations. TiB_2 sintered at 1400ºC preferentially fractures by intragranular crack propagation. Material sintered at 1500ºC fractures along weaker grain boundaries containing impurity phases. Figure 6.9(b) shows many recesses where entire grains have been ejected. As observed experimentally and supported by the fracture surfaces in Figure 6.9, fracture in the 1500ºC TiB_2 samples follows a more erratic path than for fracture in samples sintered at 1400ºC. The toughness estimated from Vickers indentation in Table 6.1 may be artificially high for the 1500ºC samples (due to wandering crack paths) and therefore contains a wide margin of error. Both hardness and toughness affect erosion resistance, yet the relative contribution of each varies between materials. Erosion results would indicate that material pressed at 1500ºC has a lower toughness in addition to slightly lower hardness. The benefit of slightly higher densities achieved by sintering at 1500ºC

was outweighed by grain growth, pore coalescence, and accumulation of impurities on grain boundaries. Further toughness testing by measuring actual fracture energies would then be required, although it would require samples larger than those produced in these experiments.

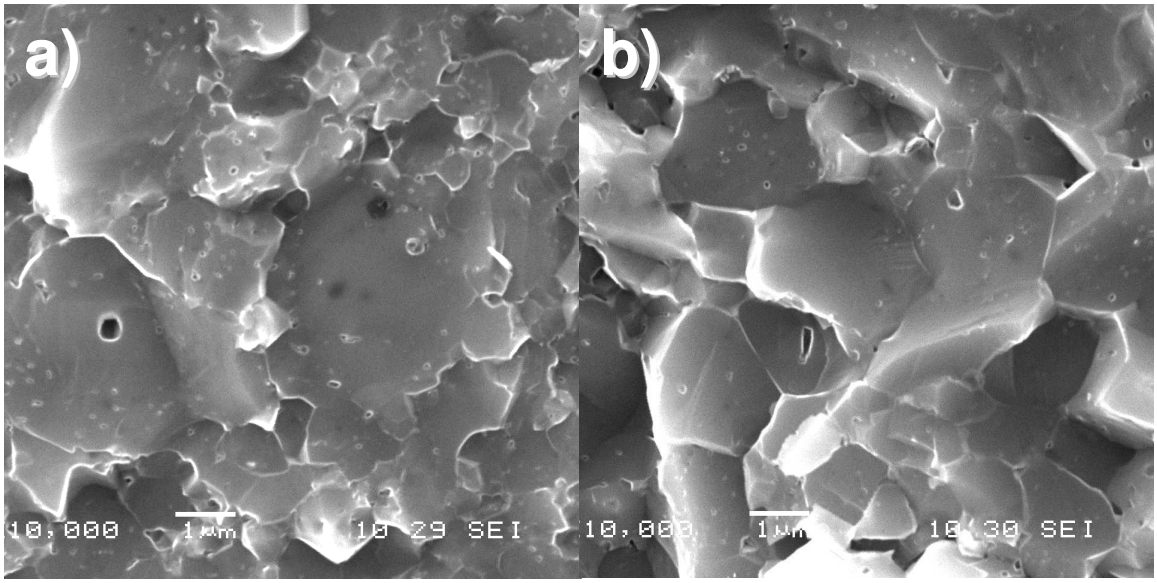

Figure 6.9: SEM micrographs of 1400ºC MM (a) and 1500ºC MM (b) TiB_2. Note higher frequency of intergranular fracture in (b).

6.6: Conclusions

Often high temperatures and high concentrations of sintering aids are used to produce high density TiB_2 compacts. This study corroborates other research that shows that low sintering aid additions (~1%) and low temperatures (as low as 1400ºC) can produce high-density material when proper processing methods are employed. Equally as important, this study has shown that temperatures considerably below those commonly employed for densification of TiB_2 (1400ºC vs. 1500 to 2000ºC) can result in an enhancement in the mechanical properties, especially erosion resistance, by preserving a highly refined grain size without a significant increase in porosity.

Steady state erosion rates of the TiB_2 samples are comparable to those for the erosion resistant grades of WC and CBN, and are significantly lower than that of the fine-grained WC-6%Co cermet. The large disparity between the erosion rates of the two WC materials illustrates how significant microstructure (both grain size and second phase additions) can be to the wear resistance of a material, as is also seen in comparisons between TiB_2 sintered at 1400 and 1500ºC. Further refinement of the microstructure as well as control of Fe, C, and O impurities could be utilized to improve the wear properties of low-temperature sintered TiB_2.

6.7: Acknowledgments

Work at the Ames Laboratory was supported by the Department of Energy, Materials & Engineering Physics, under contract number DE-AC02-07CH11358.

Chapter 7: General Conclusions

7.1: General Discussion

As stated in Chapter 3, phase-pure $AlMgB_{14}$ is difficult to form by reaction of stochiometric mixtures [117]. The same appears to be true for precipitation of $AlMgB_{14}$ crystallites from Al melts, where multiple phases of AlB_2, AlB_{12}-type (α, β or γ), and $AlMgB_{22}$ grow simultaneously with the 1:1:14 phase [4-5,8,50]. Conversely, $AlMgB_{14}$ forms readily by hot pressing of high-energy milled powders, as discussed in Chapter 4, with no evidence of the above extraneous boride phases [3,24,101].

Highly phase-pure Mg_2B_{14} was prepared in this study (Chapter 3) and by Guette, et al [7]. Attempts were made to produce Mg_2B_{14} by ball milling and subsequent hot pressing, which resulted in very low-density (estimated 20-30 % porosity) compacts with low yield of the 1:1:14 phase. A partially indexed diffraction pattern is shown in Figure 7.1, FeB was the dominant phase to form in such samples. Mg vaporization may be partially to blame, although it doesn't appear to be a significant problem in the hot pressing of $AlMgB_{14}$.

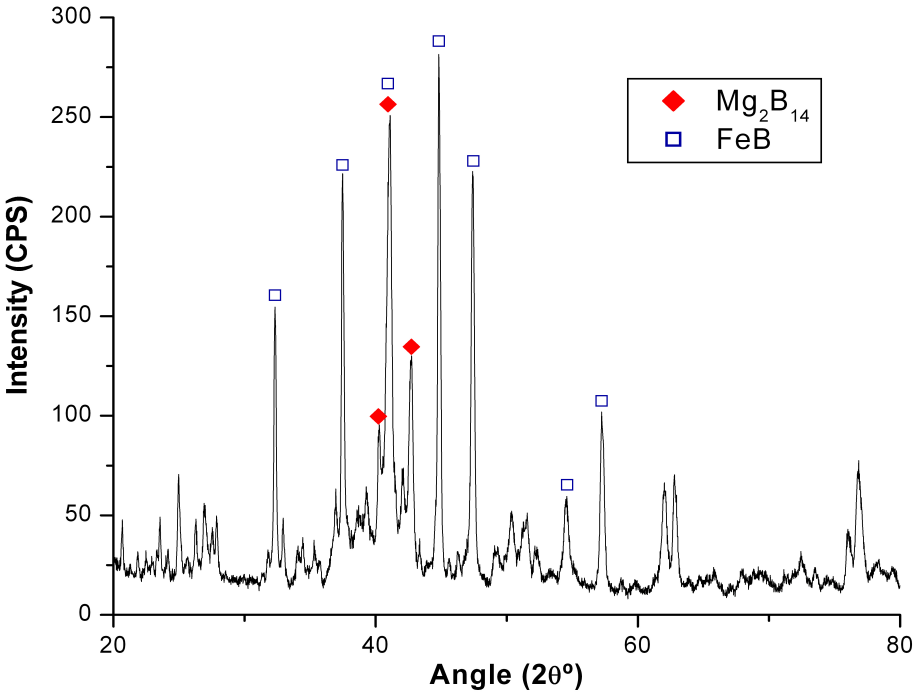

Figure 7.1: XRD pattern of Mg_2B_{14} powder hot-pressed at 1300ºC.

As discussed in Chapters 1.8 and 4, the common impurities in $AlMgB_{14}$ and its composites are O and Fe, resulting in Al_2MgO_4 and FeB phases. It was initially thought that Fe_3O_4 was another contaminant, isostructural with Al_2MgO_4 and possesing nearly identical lattice parameters and diffraction patterns. As the spinel and FeB phases are much more thermodynamically stable than any iron oxide, it is now believed that Fe_3O_4 is not present. Figure 7.2 shows the indexing of phases in a baseline sample milled with a higher media/powder ratio (~2 times greater) than average, resulting in higher Fe contamination. Note that spinel and FeB diffraction peaks have higher intensities than those of the $AlMgB_{14}$ phase. This does not correlate directly with concentration as the impurity phases have much higher X-ray scattering abilitiy than the $AlMgB_{14}$ phase. Actual impurty concentrations based on chemical analysis are estimated at 13 vol% FeB (typically 7 vol%) and 10 vol% Al_2MgO_4.

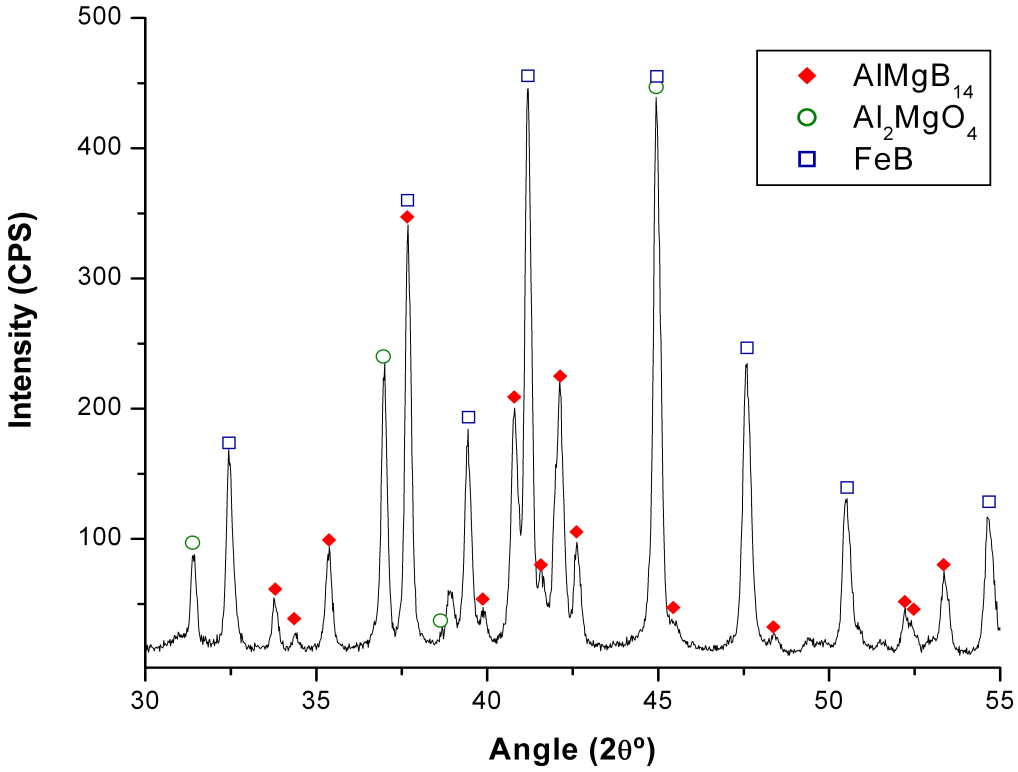

Figure 7.2: Indexing of impurity phases in baseline $AlMgB_{14}$ sample prepared with excess Fe.

More current estimates including neutron activation analysis for O characterization and inductively coupled plasma (ICP) for Fe measurements place impurities at about 5 wt% O and 10-13 wt% Fe. This is equivalent to about 10 vol% Al_2MgO_4 and 7 vol % FeB in baseline $AlMgB_{14}$ samples, see Table 7.1. Theoretical densities of all composites are based on these measurments. It should be noted that the impurity concentrations listed here disagree strongly with those measured in Chapter 4. In Chapter 4, impurities were measured by WDS which, like EDS, is less accurate with respect to light elements, especially when the material is rich in B. In the earlier case, many standards and corrections were used in the analysis of the data, which resulted in an over-estimation of B and as a consequence, a proportional drop in other, heavier elements. The differences between the data in Figure 4.4 and Table 7.1 illustrate how qualitative X-ray

spectroscopy is for these materials. Despite this, characteristic X-ray intensities for the heavier elements can still be compared for relative analysis between data aquired under the same conditions. Alternate impurity analysis techniques, such as ICP or neutron activation, of each individual sample are not feasible because these tests generally consume enough material to prepare one or more samples.

Table 7.1: Nominal and measured compositions due to impurities and average densites for Spex samples.

Nominal:		Actual:				
TiB_2 (wt %)	TiB_2 (vol %)	$AlMgB_{14}$ (vol %)	TiB_2 (vol %)	FeB (vol %)	Al_2MgO_4 (vol %)	Density (g/cm^3)
0.0%	0.0%	82.9%	0.0%	7.3%	9.8%	93-94%
30.0%	20.8%	63.9%	22.7%	5.8%	7.6%	95-96%
50.0%	38.0%	49.0%	40.6%	4.6%	5.8%	95-98%
70.0%	58.8%	31.7%	61.3%	3.2%	3.8%	98-99%

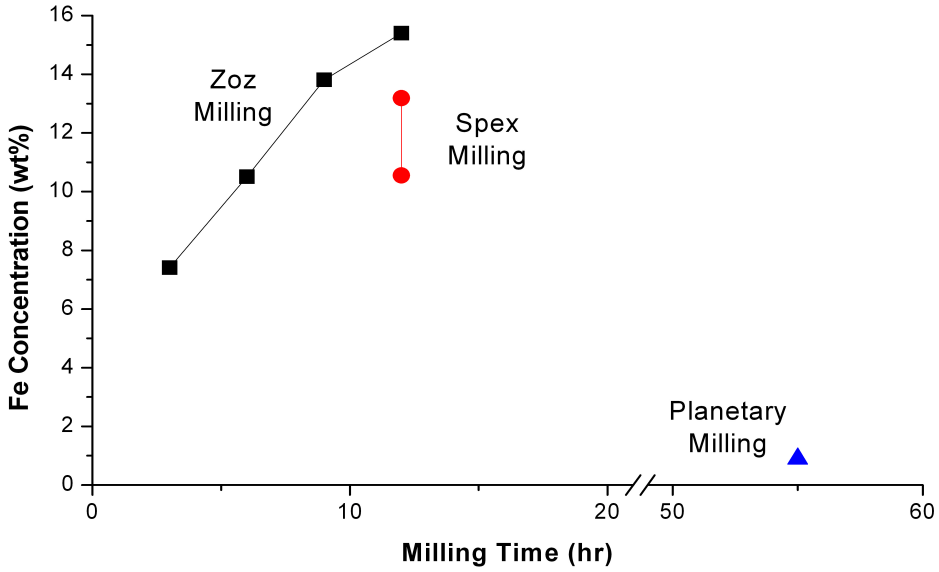

Figure 7.3: Fe contamination after milling as measured by ICP.

Fe contamination is the result of wear of the media and vial during milling. In the Zoz mill, there is additional wear from the impellers which can be quite significant as is evident after multiple milling cycles where “fins” of smeared steel trail behind each of

the impeller tines. Figure 7.3 shows how Fe concentration varies with milling type. Planetary milling tends to introduce less than 1 wt% Fe, resulting in low density compacts, between 90 and 95 % of theoretical, and due to the low energy of the mill, the grain size is larger than that of Spex material. Planetary milling has since been abandoned in favor of the higher comminution rate and resulting finer grain sizes when using Spex milling. Again, Fe shows a significant contribution to densification. The decrease in Fe contamination with added TiB_2 is due to the introduction of most of the Fe from wear during the 12 hr preparation of the baseline material. As Table 7.1 shows, density actually increases with TiB_2 addition and reduced Fe contamination. This indicates that a few percent Fe may be all that is necessary for proper densification for all compositions of the $AlMgB_{14}$ - TiB_2 composites.

Figure 7.4 compares the comminution behavior of baseline powder milled in the Zoz and Spex mills. After an hour of Zoz milling the peaks of the constituent metals are still visible. The broadening of peaks beyond this point indicates heavy plastic deformation and the beginning of amorphitization of the powders. The pattern at the top of Figure 7.5 is for powder produced in a typical 12 hr Spex milling of $AlMgB_{14}$, as described in Chapter 2.1, and appears to be very similar to only 3 hr of Zoz milling. Since the media speed in the Zoz mill was expected to be, at best, comparable to that in the Spex mill, this was investigated further.

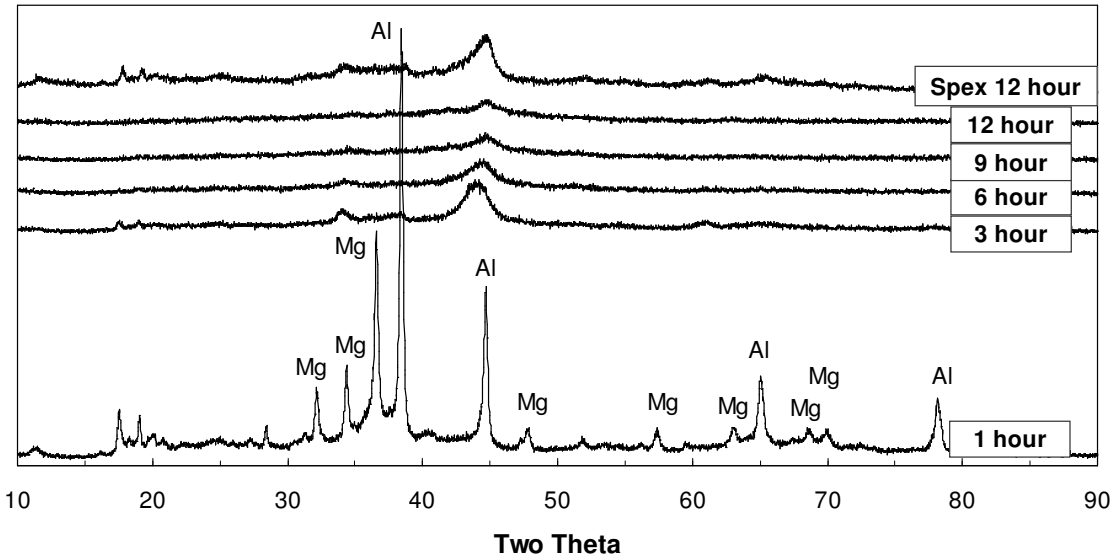

Figure 7.4: XRD patterns of $AlMgB_{14}$ powders produced by Zoz milling, compared to $AlMgB_{14}$ Spex milled for 12 hours (top).

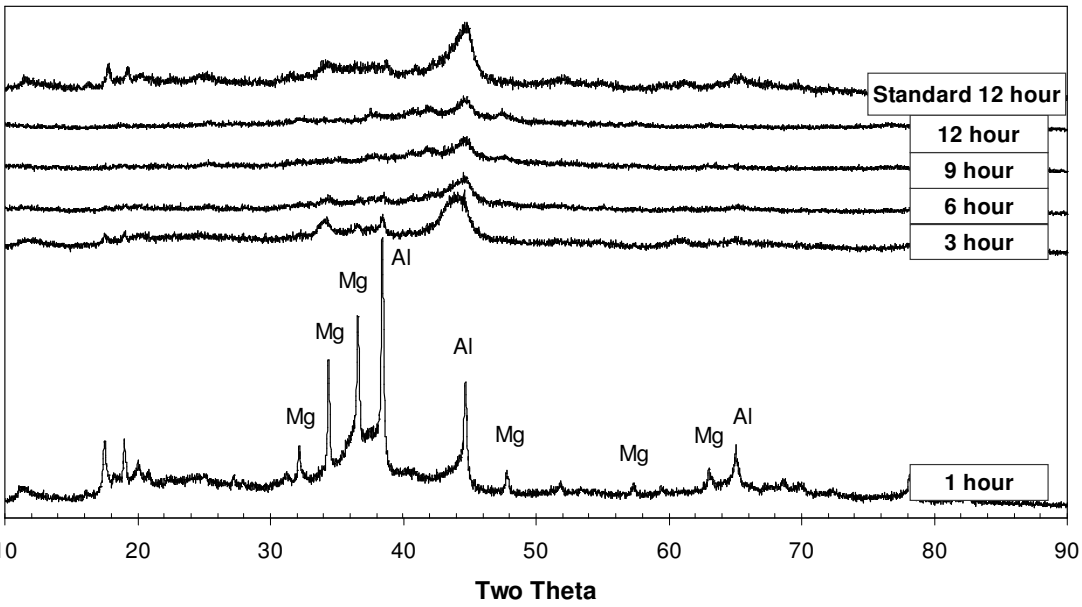

Figure 7.5: XRD patterns of $AlMgB_{14}$ powders produced by Spex milling with media/powder mass ratio, 13.3, identical to that used in Zoz milling, compared to $AlMgB_{14}$ Spex milled for 12 hours with typical media/powder ratio of 6.75 (top).

The media to powder ratio in the Zoz mill was about twice that used in the Spex mill. For comparison, a Spex vial was loaded with a media/powder mass ratio of 13.3 (equal to Zoz milling) and XRD patterns were taken of powder sampled at the same times. ICP

analysis of this powder indicated Fe contamination as high as 22 wt% (~13 vol% FeB), significantly higher than in Zoz milling for identical times. Figure 7.5 shows how the comminution rate increased compared to a standard Spex milling by increasing the media/powder ratio. Comparison of Figures 7.4 and 7.5 shows high correlation between Spex and Zoz milled powder with the same charge ratio. Although the level of plastic deformation in both powders appears to be approximately the same by XRD, the higher wear rate in the Spex vial, resulting in 22 wt% Fe, indicates much higher energy collisions with this type of mill.

Hot-pressed compacts from Zoz material had densities ranging from 87-91 % of theoretical. Baseline Spex samples with 13 to 22 wt% Fe densified to 92 and 94 %, respectively, indicating that 16 wt% Fe in the Zoz powders shouldn't be the source of lower densities. As mentioned in Chapter 4, the form of the Fe additions may be important. If Fe wear debris form FeB during milling, the sintering potential of the powder is drastically reduced. Due to the level of deformation in both the Spex and Zoz powders, the state of the Fe contamination cannot be determined by XRD, but XPS or PEELS may be able to resolve the binding state of Fe even if the powders are partially amorphous. If there is a difference in Fe compounds between Zoz and Spex powder, it must depend on some condition of the milling process, such as collision energy, temperature, or perhaps composition of the steels used in the mills. Both mills use similar Cr-steel media, but the milling chambers are likely different grades of steel. Even minor elemental additions could catalyze the Fe → FeB transformation.

Zoz material also has a higher risk of O contaminiation, which may fluctuate from batch to batch. The powder loading and retrieval system of the Zoz mill incorporates ball valves to isolate the atmosphere. The valves are easily clogged with powder and the abrasive powders used in this study quickly damage the seals. O concentration has not been measured for all powders produced by the Zoz mill, and so the significance of these failures is unknown. Spinel likely hinders densification as it is a rather refractory phase (T_m > 2000ºC), and is considered to be entirely deleterious to the properties of the $AlMgB_{14}$ composites. Redesign of the powder transfer mechanisms of the Zoz mill is required to alleviate any O problem as well as ease the relative difficulty of powder transfer to and from the mill currently.

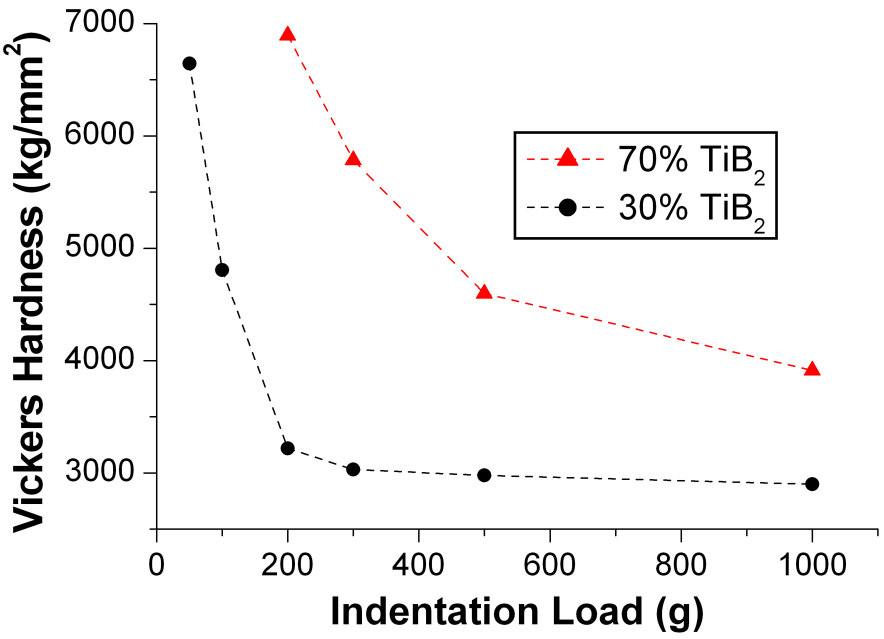

Figure 7.6: Indentation size effect on hardness of an $AlMgB_{14}$ - 70 wt% TiB_2 composite compared to an older 30 wt% TiB_2 composite (Lewis) [14].

As advancements in production of the $AlMgB_{14}$ composites have resulted in increasing hardnesses, mostly through the refinement of grain sizes and increase of TiB_2 additions to

70 wt%, the indentation size effect becomes a serious problem when measuring hardness. As shown in Figure 7.6, 1000 gm-f indentation loads are not sufficient to be in the plateau hardness region for higher concentrations of TiB_2.

Perhaps just as significant to hardness measurement of super-hard materials are the various sources of measurement error. Measurement at 1000 gm-f produces indent diagonals 20 to 25 μm in length. Figure 7.7 shows a hypothetical plot (based on actual data) for measured hardness of a composite with a nominal hardness around 3500 kg/mm^2 standard deviation of about 0.7 μm in the measurement of the indent diagonals. The value of 0.7 μm was chosen since it is approximately the least variation achieved with optical measurements of indentations on 70 wt% TiB_2 composites. At low loads (including 1000 gm-f), two standard deviations (95% confidence interval) result in measurement fluctuations of greater than ±500 kg/mm^2. Since area does not change linearly with diagonal length, balanced error in length measurements result in hardness values skewed slightly towards over-estimation.

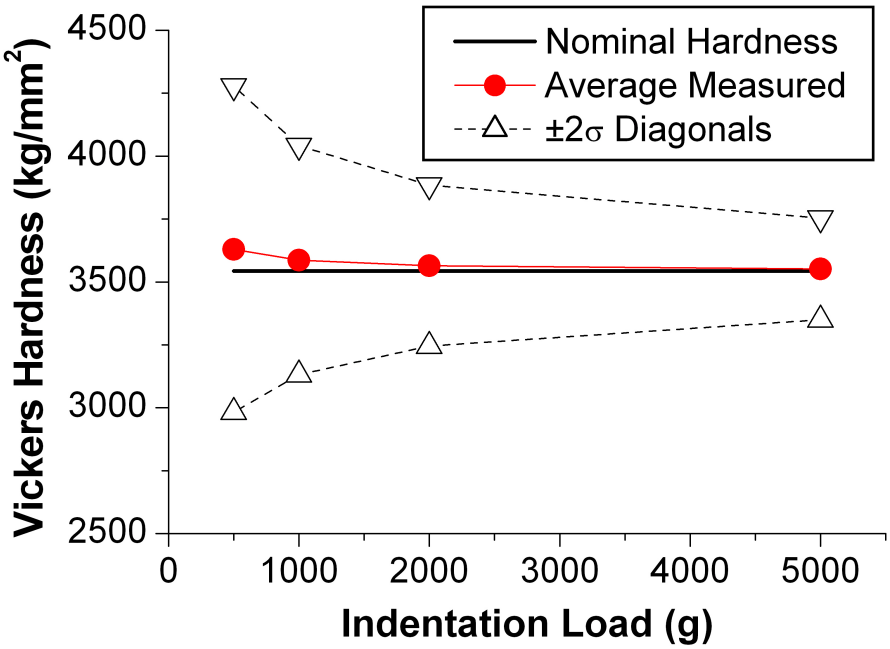

Figure 7.7: Effect of measurement error on hardness at different indentation loads. For $AlMgB_{14}$ - 70 wt% TiB_2 composite with nominal hardness 3540 kg/mm^2 and standard deviation of diagonal measurement of ±0.7 µm.

More serious than the slight fluctuation caused by perfectly symmetrical data errors are asymmetric variations in measurement. Optical measurement of indentations, especially those 20-25 µm wide, can be very subjective and this lends easily towards a bias of measurement. Average measurements of the same sample from various observers can result in differences >200 kg/mm^2. As shown in Figure 7.7, biased data collection of about 1 µm can easily account for this error. Repeated measurements by the same observer on the same sample can have nearly as much variation. Indentation loads of 5000 gm-f or greater can drastically reduce the significance of measurement error, as indents are about 60 µm in 70 wt% TiB_2 composites.

Measurement of hardness indentations using SEM, though significantly more time-consuming, was investigated. Reduced edge contrast compared to optical microscopy

resulted in similar measurement errors. Lower accelerating volatage (~5 kV) reduced phase contrast but did not significantly improve edge contrast. The vast improvement in depth of field over optical measurements offered some advantage, and standard deviation of measurements was marginally lower. But this was not deemed worth the extra effort required versus optical measurements. As shown above, in Figures 7.6 and 7.7, measurement errors and subjectivity have proven to be at least as significant as the indentation size effect over the same range of testing loads.

Those familiar with hardness measurements understand these complications. As mentioned it Chapter 1.3, the most reliable hardness data are reported with details of the measurement parameters, sometimes including micrographs of indentations for readers to make their own, at least rough, observations [30,46,131]. Sometimes the emphasis on hardness without mention of the potential errors can lead some to jump to conclusions and report extraneous data rather than averages or fail to appreciat concepts such as the indentation size effect [136]. Hardness appears to be a simple concept, yet quantifying it is quite difficult, especially when investigating potential super- and ultra-hard materials.

Because hardness measurements made with available equipment were proving to be less dependable as a quantifiable measurement of sample quality, perfomance based tests were employed more frequently. Testing had already been performed on select samples with respect to cutting performance, abrasion testing, and scratch hardness [13,69-70]. Erosion testing had been performed on some samples using an industrial grit-blaster. Variations in erodent flow rate, velocity, grit quality, etc. limited its use at the time to

purely qualitative comparisons. Yet when samples were tested alongside a commercial WC/Co cutting tool, data "calibrated" to the WC standard was surprisingly reproducible. Testing parameters were standardized to a degree, making this somewhat primitive form of erosion testing at least semi-quantitative.

The ease, rapidity, and reproducibility of this testing lead to the acquisition of an erosion testing system that conformed completely to the ASTM G 76 standard for "Conducting Erosion Tests by Solid Particle Impingement Using Gas Jets" [89]. Figure 7.8 shows some results using the ASTM standard test. The standard allows for significant flexibility in testing parameters, provided all said parameters can be controlled and the settings reported. Some of the guidelines include; that particle velocities are typically less than 100 m/s, the sample must be significantly larger than the erodent stream to ensure all erodent impacts the specimen, and all results should be reported in mm^3/g (volume of target loss per gram of erodent). Estimated particle velocities during previous use of the industrial grit blaster were between 100 and 200 m/s and the erodent stream was significantly larger than any sample, thus preventing any measurement of the amount of grit impacting the sample.

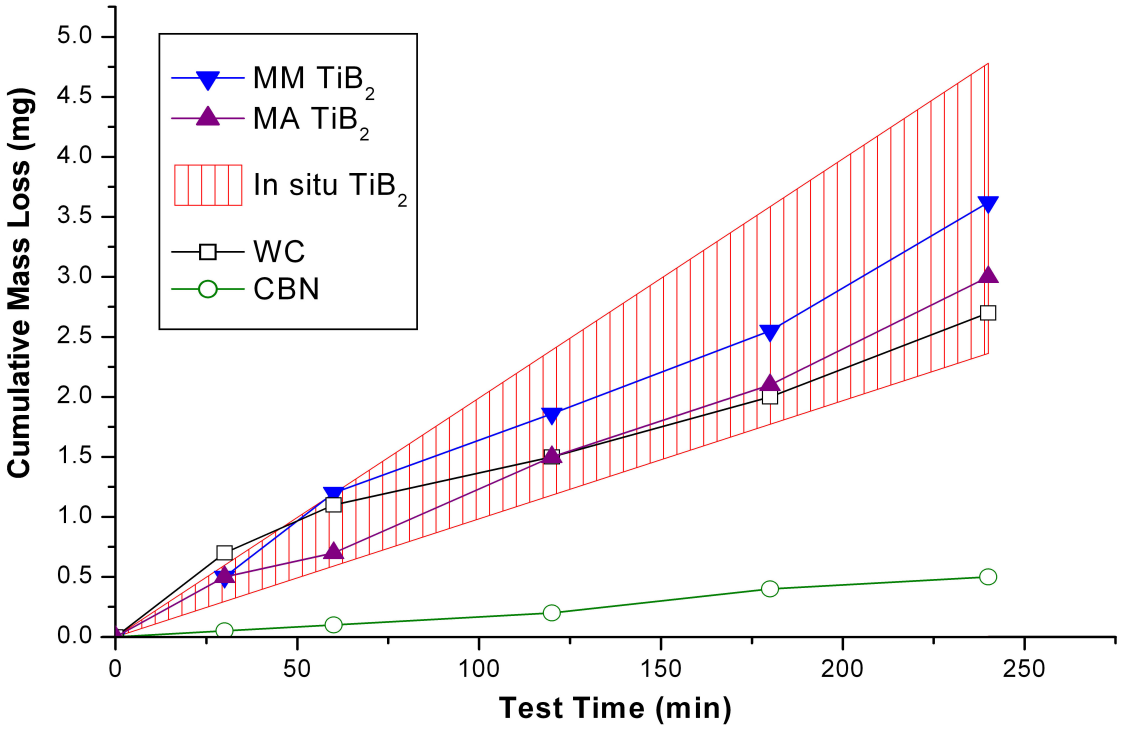

Figure 7.8: Erosion losses using ASTM standard test of three $AlMgB_{14}$ - 70 wt% TiB_2 composites, prepared identically except for the nature of the TiB_2 addition; MM, MA, and a range of erosion rates for in-situ TiB_2. Erosion rates compared to wear resistant grades of commercial WC and cBN. Erosion test conditions were as follows: 100+ µm Al_2O_3 grit, 1 cm stand-off distance, and 77 m/s impact velocity at 90º to the sample surface.

Figure 7.8 shows the erosion rates of $AlMgB_{14}$ composites with 70 wt% of either MM, MA, or in-situ TiB_2. MM TiB_2 is coarser than that produced by MA, and a corresponding trend in reduced erosion rates can be seen. In-situ TiB_2 additions produce a mixture of microstructures which result in the range of erosion rates seen above. The majority of the microstructure is comprised of a fine mixture of TiB_2 grains which are surrounded by a thin layer of $AlMgB_{14}$. The $AlMgB_{14}/TiB_2$ ratio in these regions is lower than that in other 70 wt% TiB_2 composites. The excess $AlMgB_{14}$ appears to comprise larger (1-5 µm) crystals that are unevenly distributed throughout the material. Inspection of erosion craters shows that these crystals erode faster than the surrounding fine-grained material, and clusters of these crystals can seriously degrade the erosion

resistance of the surrounding microstructure, thus causing the range of erosion rates shown by this composite. Due to the distribution of $AlMgB_{14}$ around the TiB_2 grains in the in-situ composite, TiB_2 grain growth is suppressed and the grain boundaries appear to be stronger than those in pure TiB_2, as discussed in Chapter 6. The strengthening effect of the $AlMgB_{14}$ layer may also arise from similar mechanisms observed in the $TiB_{2.4}$ films discussed in Chapter 1.3 [39]. With removal of the larger crystals, higher concentrations of TiB_2 could be used as $AlMgB_{14}$ is better distributed and less is needed to strengthen the grain boundaries. As seen in Figure 7.8, this could result in further improvement of erosion resistance over current composites.

Erosion data reported in Chapter 5 was aquired by the semi-quantitative grit blast method and indicated that some $AlMgB_{14}$ - 70 wt% TiB_2 composites perfomed at least as well as cBN tools designed specifically for erosion resistance. These results show comparitively better performance of the $AlMgB_{14}$ composites than results obtained using ASTM standard testing. The major difference in erosion conditions between the to tests were particle velocity, >100 m/s and 77 m/s, and erodent size, +150 µm Al_2O_3 vs +100 µm Al_2O_3, for the grit blast and ASTM tests, respectively. Since impact energy is proportional to $m \cdot v^2$, it scales exponentially with each of the above parameters. As a rough comparison, erosion rates seen in the ASTM tester after about 1 hr occurred in the grit blaster in about 1 min, although the ASTM erosion crater is approx. 2-3 mm in diameter and the grit blaster erodes the entire 13 mm dia. sample. Additionally, the grit blaster abrasive is re-used repeatedly and for many applications and is therefore likely less angular and aggressive an erodent than in the ASTM test.

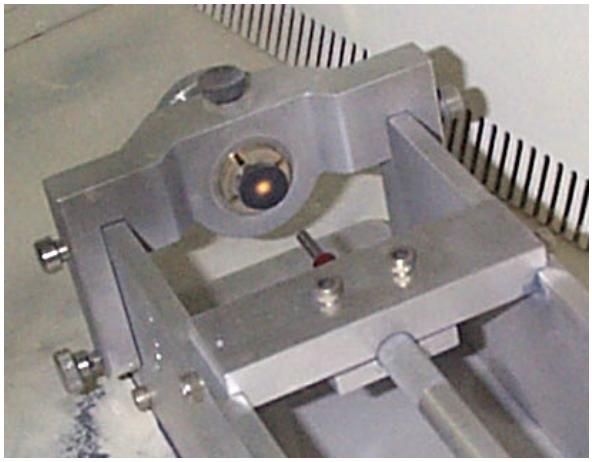

Figure 7.9: Close-up of ASTM standard erosion tester. Sample (dark) near center of image. Note faint orange glow from center of sample, due to heat generated by erosive jet (not visible).

As can be seen in Figure 7.9, the impact crater glows lightly during testing, indicating a surface temperature of >500ºC. Calculations predict a local temperature increase of anywhere from 200 to 700 Cº for the ASTM testing conditions. Surface temperatures during grit blasting, at least locally during impact, would then be expected to be much higher. As shown in Figure 5.4, such improvement in relative performance to commerical hard materials indicate the $AlMgB_{14}$ composites' superior high-temperature strength and oxidation resistance. WC is known to have especially low oxidation resistance. Open-air oxidation tests at 1000ºC showed rapid oxidation of a half-inch dia. WC/Co ceremet into many times its volume of spongy oxide. Erosion testing with an inert gas propellant would eliminate the oxidation component and determine how significant the composites high-temperature strength is in comparison to commericial materials.

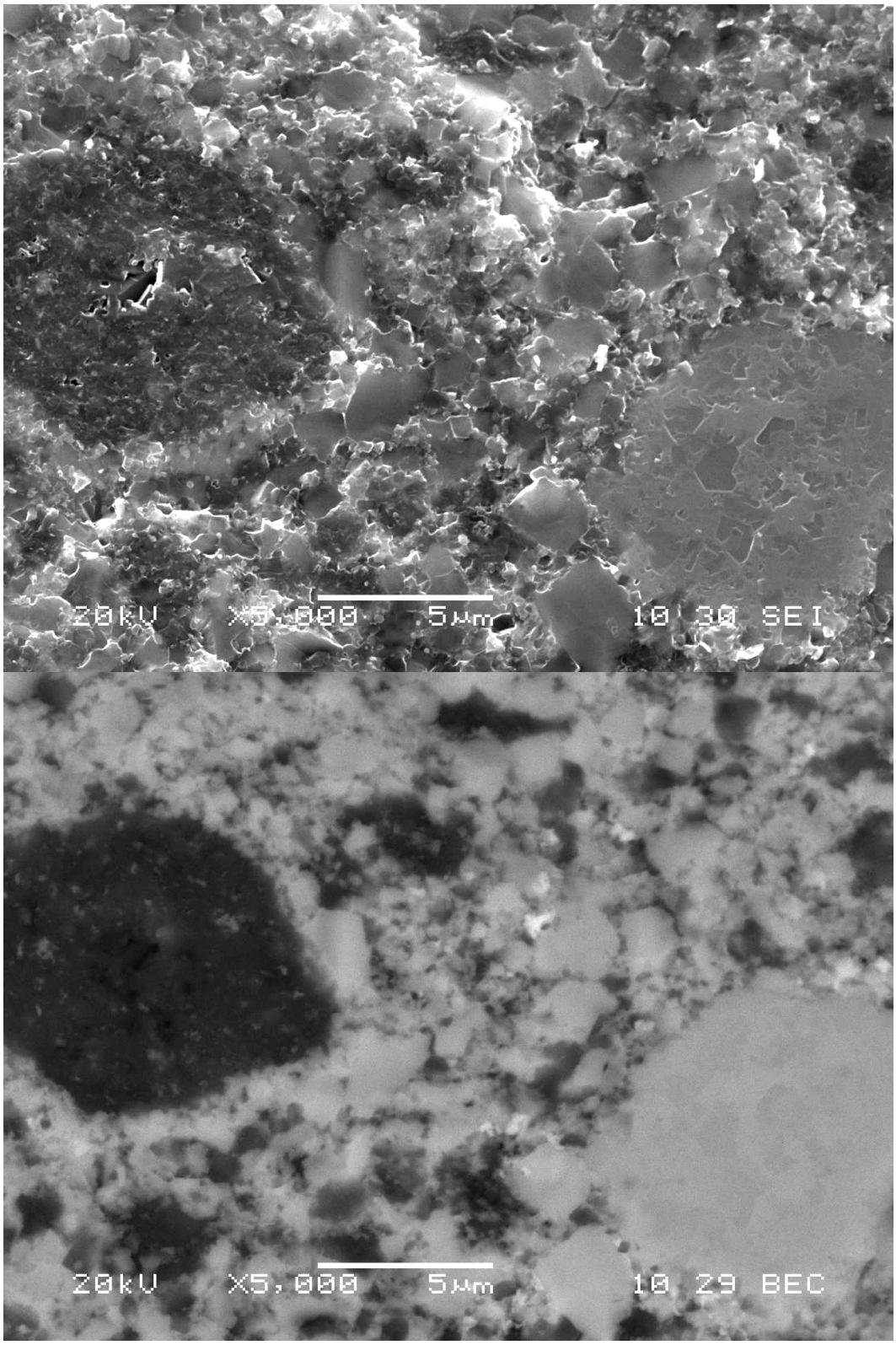

Figure 7.10: Fracture surface of $AlMgB_{14}$ - 70 wt% MM TiB_2 composite, same area by SE (top) and BSE (bottom) imaging. $AlMgB_{14}$ agglomerate (dark) and TiB_2 agglomerate (light) surrounded by typical composite microstructure. Hot-pressed at 1400ºC and 106 MPa pressure.

Figure 7.10 shows a special case of average composite microstructure with well-formed agglomerates of each $AlMgB_{14}$ and TiB_2 in close proximity. The resulting fracture surface of this region should show all the modes of fracture expected in this composite. Both of the agglomerates exhibit roughly planar fracture, indicating little crack deflection. In the case of single phase agglomerates, this is not undesirable, since without the inclusion of reinforcement phases, crack deflection would then be largely the result of pre-existing microcracks and weakness along grain boundaries. Excessive microcracking and interfacial weakness can quickly degrade properties, the above images indicate minimal flaws and good grain-boundary strength. The surrounding fine-grained region does not show any obvious examples of grain-pullout and all TiB_2 grains appear to fracture transgranularly. The TiB_2 fracture surfaces all appear to be roughly in parallel to each other, indicating a lack of weaker, preferential cleavage planes from the presumably randomly oriented grains. The behavior at the edges of the TiB_2 grains, where finer $AlMgB_{14}$ particles are dispersed, is less clear. The surface roughness indicates crack deflection, yet it is uncertain whether this is due to an inherent weakness (low grain boundary cohesion, etc) or strengthening mechanisms (such as crack tip bridging). A fractograph alone is not enough to tell for certain, but the low erosion rate of this sample provides encouragement for the latter. Two additional fracture surfaces are shown in Figure 7.11. The left similar to that in Figure 7.9 but with MA TiB_2, which resulted in a finer distribution of TiB_2, and the right a sample hot-pressed at 1500ºC from $AlMgB_{14}$ - 50 vol% TiB_2 powder produced by Ceramatec, Inc.

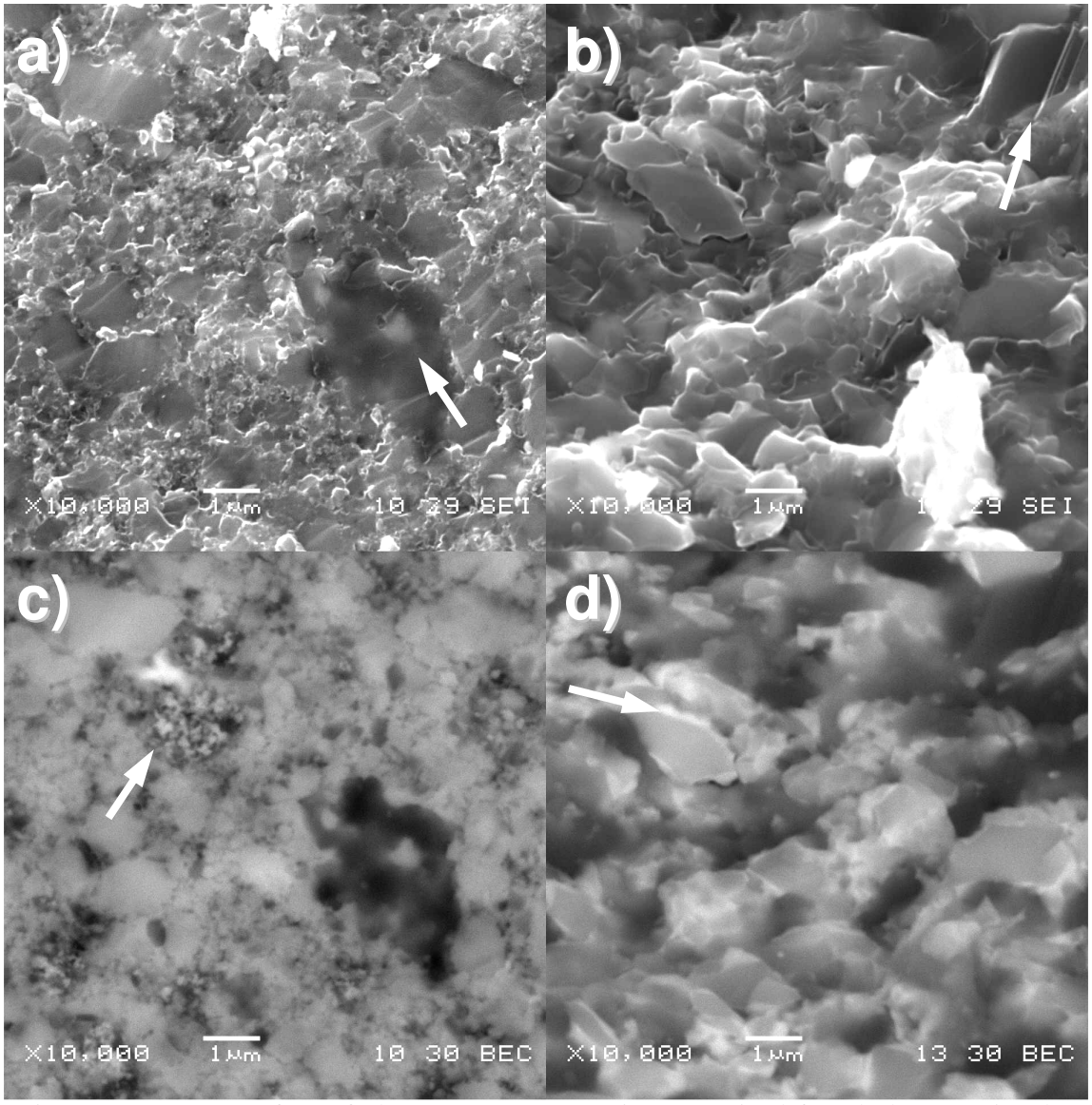

Figure 7.11: Fracture surfaces of $AlMgB_{14}$ - 70 wt% MA TiB_2 composite (left) and $AlMgB_{14}$ - 50 vol% TiB_2 Ceramatec composite (right), same areas by SE (top) and BSE (bottom) imaging.

Figure 7.11(a) shows similar fracture features to that in Figure 7.10, only with a finer distribution of TiB_2. Note the large $AlMgB_{14}$ grain (arrow) with interior TiB_2 grain. There appears to be no disturbance of the crack front as it passed across the central TiB_2 grain, indicating a very coherent grain boundary. Conversly, a cluster of Fe-rich impurities is visble near the arrow in Figure 7.11(c), which as a whole, likely constitutes

a significant flaw. Little is known about the preparation of the Ceramatec powder as the production methods are proprietary. The average grain size is comparable to that of the MM TiB_2 powder (~1 μm), but the tighter size control and near absence of <200 nm grains indicates that no high-energy milling processes were used. EDS shows the presence of W (Figure 7.11(d), bright phase indicated by arrow), likely in the form of WC, which appears to coat many grain boundaries. Either this is intentionally added or a product of wear of WC media. The fracture surface in Figure 7.11(b) shows significant porosity and possibly some grain pull-out. The presence of bright WC phases at many of the free edges of TiB_2 grains may be evidence that this WC layer weakens the grain boundaries. But this cannot be infered strictly from the fracture surface; the visible porosity alone could be sufficient to weaken the composite. The Ceramatec material partially supports the use of high-energy milling to produce fine microstructures. Even the agglomerates seen in Figure 7.11 are comprised of many sub-micron grains. Each particle in the Ceramatec composite appears to be comprised of a single grain, judging by some of the fracture surfaces and cleavage steps indicated by the arrow in Figure 7.11(b).

7.2: Conclusions

- Reliable, easily reproducible hardness data of the $AlMgB_{14}$ - TiB_2 composites will require indentation loads higher than 1 kg-f. Until such equipment is accessible, only qualitative comparisons should be made between samples measured with the same tester, as consistently as possible, and preferably by the same person.
- Fe additions should be limited to ~3 wt% for optimum combination of sinerability and minimum necessary residual FeB. O contamination should be eliminated to

whatever degree possible. No benefit has been shown for the presence of the Al_2MgO_4 phase. Fe reduction will require changes in milling parameters, this must be done while maintaining the degree of comminution provided by the Spex mill.

- Despite up to 7 vol% FeB and 10 vol% spinel in most $AlMgB_{14}$ - TiB_2 composites, they possess quite remarkable hardness and erosion resistance. Reduction of these impurity phases could potentially result in a substantial improvement over current property records for these composites.
- $AlMgB_{14}$ - 70 wt% (60 vol%) TiB_2 composites show the best combination of mechanical properties. This may partially be due to the overall reduction in impurity phases with increasing TiB_2, but the ideal composition of the composites should be around 60 vol% TiB_2.
- Reduction of grain size results in a noticable increase in erosion resistance. Due to changes in impurity concentrations with changes in milling methods that result in grain refinement, the optimum ratio of $AlMgB_{14}$/TiB_2 may vary. Likewise, the optimum ratio may vary as changes in microstructure result in changes in strengthening mechanisms.

7.3: Future Work

As mentioned above, reduction of impurity phases should be the top priority. While Fe reduction will require changes in milling, Steve Nunn at Oak Ridge National Laboratory (ORNL) is investigating the removal of O-based impurities from raw B powder using methylation of B_2O_3. B_2O_3 reacts with methanol to form trimethyl borate ($B(OCH_3)_3$), a

volatile compound that can be removed from the powder by vacuum drying. Catalysts and milling can be used to accelerate this reaction. Partial cleaning of oxides from boron powder is also possible using water. Hydrated boron oxide (boric acid) is readily soluble in hot water. Subsequent rinsing with deionized water and vacuum drying can result in the removal of excess oxide impurities.

Scale-up of powder production from ~1 gram Spex milled samples to kilogram quantities in the Zoz mill should move forward. Use of the Zoz mill is currently on hold as the rotors need to be replaced and improvements need to be made to the powder handling system. Currently, powder is loaded and retrieved through piping and isolated from outside air by ball valves. The piping readily clogs with the fluffy, cohesive powder before and after milling. Additionally, the moving parts of the ball valves quickly wear from the abrasive particles, causing them to stick and degrading the quality of the seals. Re-design of the powder handling system would have a significant impact on the usability of the mill and the quality of the powder produced.

Reduction of grain size has been shown to have a significant effect on erosion resistance. Milling parameters could be adjusted to reduce the grain size in MM and MA composites further; specifically milling time or media size, type, or fraction, but this will also have an effect on impurity concentration and other factors. The in-situ composites show promise, but the nature of the large crystals needs to be understood so they can be eliminated from the microstructure. Compared to the MM and MA composites, the difference in the distribution of the $AlMgB_{14}$ phase around the TiB_2 grains results in a higher local TiB_2

fraction and may be analogous to the heterostructures described in Chapter 1.3. This may shift the greater than rule of mixtures mechanical properties seen in the composites to higher TiB_2 concentrations.

Outside investors in the $AlMgB_{14}$ composite technologies are investigating other methods of powder production, though none so far have been able to compare to the fine grain structure produced by high-energy milling. Ceramatec, Inc. has succeeded in producing large quantities of $AlMgB_{14}$-TiB_2 powder through proprietary methods. This powder has significantly larger grains (1-5 μm) than high-energy milled material and compacts hot-pressed from this coarser material exhibit inferior erosion resistance. This powder is also partially handled in air, although the larger grain size lessens the effect of oxygen contamination, and contains a small amount of W_2B_5 along phase boundaries that appears to promote intergranular fracture.

Hardness testing requires higher-load indentation equipment in order to improve the reliability of hardness data, though this is not immediately necessary. Erosion testing has shown excellent reliability in rating sample quality and since its results correlate very closely with real wear applications, it can provide direct comparisons to expected performance. Steve Nunn at ORNL can also provide Vickers hardness testing up to 10 kg loads. Additionally, Ames Laboratory is in the process of purchasing a new Vickers hardness tester capable of loads as high as 50 kg. With faster sample turn-around due to an on-site high-load indenter, hardness and erosion data will provide a broader picture of composite properties. Higher indentation loads should also allow for the determination

of the proper Palmqvist equation to use at a given load. This can be accomplished by plotting toughness estimated by Equations 3 and 4 versus indentation load until a discontinuity is found in each. In the regime where toughness is constant, Equation 3, for half-penny cracks, should be valid for any load above the discontinuity. A valid regime for Equation 4 will only be found if Palmqvist-type cracks appear at loads higher than the onset of the indentation size effect.

If resources allow for more exploratory and theoretical investigations, certain modifications to both the $AlMgB_{14}$ and the TiB_2 phases would be especially interesting. Previous $AlMgB_{14}$ samples prepared by milling used a 1:1:14 ratio of the constituents, yet the actual stoichiometry of the compound is expected to be around 0.75:0.78:14, respectively. Since there is also expected to be some loss of Mg and Al due to vaporization and formation of oxide impurities, a stoichiometric ratio may contain too little Mg or Al to form the 1:1:14 phase, but a ratio of constituent elements closer to the actual stoichiometry may be found to be more favorable. Table 7.2 lists two compositions that should be prepared first to compare to the current $AlMgB_{14}$ production method. The "Excess Mg" composition would be a starting point to account for Mg vaporization, which has been observed during hot pressing of some samples, especially under vacuum.

Table 7.2: Alternate $AlMgB_{14}$ compositions

	Atomic Ratio		
	Al	Mg	B
Current	1.00	1.00	14
Stoichiometric	0.75	0.78	14
Excess Mg	0.75	1.00	14

Unless there is a drastic reduction in densification or mechanical properties, the differences between these compositions may be small and hence difficult to determine. XRD will be useful for verifying formation of the 1:1:14 phase, but any additional phases resulting from excess Al, Mg, or B would likely be present in concentrations too low to detect; currently if any such phases exist, they have gone undetected. Prior to testing the above compositions, chemical analysis should be performed on current baseline $AlMgB_{14}$ material as it would be useful in determining how much Mg is expected to be lost due to vaporization. In order to do this properly, new chemical analysis techniques would have to be sought. The high B content of the samples makes accurate composition difficult to determine by methods currently used, such as ICP or EDS.

As discussed in Chapter 1.4, there are many 1:1:14 compounds of as-yet unknown hardness. Single crystal hardness measurements have indicated that $AlLiB_{14}$ may be harder than $AlMgB_{14}$, but again, one must avoid jumping to conclusions over individual reports of hardness [50]. Single samples of $AlLiB_{14}$, $AlYB_{14}$, and $AlErB_{14}$ have been produced by ball milling in the past, yet were destroyed before XRD was performed. Additional research into the mechanical alloying of these compounds, and Mg_2B_{14}, should focus on altering processing parameters to form phase-pure compacts. Milling time and hot-pressing temperature may have the greatest effect, as evidenced by the small amount of work done in the milling of Mg_2B_{14}. Also, mixed elements in Site I and II of the lattice appear to be possible, though there are no reports of such compounds. Table 7.3 lists these above compositions with other potential mixed 1:1:14 borides. Unless experiments mentioned above show benefits to preparing $AlMgB_{14}$ powder from

elemental ratios closer to actual stoichiometry than 1:1:14, the following samples should also be prepared with the 1:1:14 ratio. Metal-deficient systems have not been prepared previously and may prevent formation of the 1:1:14 phase.

Table 7.3: Potential substitutions and mixed substitutions to the $AlMgB_{14}$ compound.

Nominal Composition	Site I	Site II
Mg_2B_{14}	Mg	Mg
$AlLiB_{14}$	Li	Al
$AlYB_{14}$	Y	Al
$AlErB_{14}$	Er	Al
$Al_{0.5}Mg_{1.5}B_{14}$	Mg	Mg/Al
$AlLi_{0.5}Mg_{0.5}B_{14}$	Mg/Li	Al
$AlRE_{0.5}Mg_{0.5}B_{14}$	Mg/RE	Al

Due to the amount of research already done, the most important of these compositions is Mg_2B_{14}. Work on Mg_2B_{14} production by high-energy milling should continue. Previous work showed the highest fraction of the 1:1:14 phase when milling time was reduced to 2 hr and hot pressing temperature reduced to 1300ºC. Porosity was high in this sample, likely due to a combination of temperature, Fe concentration, and large particle size. Milling with WC media rather than steel could be used to increase milling time while minimizing formation of FeB which was found to be a significant contaminant (Figure 7.1). Excess Mg may need to be added to account for any losses due to vaporization, a ratio of Mg:B as high as 3:14 may be suitable. Again, better compositional analysis to determine the amount of Mg loss would provide a better starting point. Whether or not the densification of Mg_2B_{14} is improved, if the fraction of the phase formed can be increased, a mixed composition of $Al_{0.5}Mg_{1.5}B_{14}$ should be attempted. XRD would be able to distinguish if one or two 1:1:14 phases form during sintering. Site II substitutions of less than 50% Mg (i.e. $Al_{0.8}Mg_{1.2}B_{14}$) may produce a single phase compound more

readily, and should be attempted if initial experiment fails, but changes in structure would be harder to detect.

If the above investigation results in a better understanding of the processing required to form the 1:1:14 phase, the additional compositions listed in table 7.3 could be attempted. Additional samples of $AlLiB_{14}$, $AlYB_{14}$, and $AlErB_{14}$ should be attempted to determine if the 1:1:14 phase will form from milled powder. The larger site, Site I, is able to hold more variety of metallic elements and explorations replacing Mg in $AlMgB_{14}$ with 50-50 concentrations of Mg-Li or Mg-RE would be interesting. In addition to the greater understanding of icosahedral borides and complex hard structures, these studies may reveal compounds superior to $AlMgB_{14}$ in the boride composites, with respect to one or more properties.

Mutual solubility of many diboride compounds is already known. Replacing Ti partially or fully in the $AlMgB_{14}$ - TiB_2 composites with other transition metals could have a number of effects. A recent experiment attempted to produce $Ti_{0.5}Zr_{0.5}B_2$ by MA as described in Chapter 6. XRD showed that the powder was single phase diboride, presumably formed by MSR [82,128]. Initial observations indicate that hot pressing of this powder at 1400ºC resulted in a near-fully dense compact. A mixture of this powder with $AlMgB_{14}$ did not produce a dense compact prior to hot pressing, this will need to be investigated further. Additionally, VB_2 and CrB_2 are fully miscible with TiB_2 and would make good candidates for similar tests [54]. VB_2 has mechanical properties and corrosion resistances comparable to, though less than, those of TiB_2, yet with a

significantly lower melting temperature that could be utilized to lower the processing temperature of the composites [137]. CrB_2 possesses significant corrosion resistance, and excels in oxidation resistance over TiB_2 and thus could have many potential applications [138]. ZrB_2 has a larger lattice than TiB_2, while the VB_2 lattice is smaller. Slight lattice parameter changes may affect the strength of the 1:1:14-diboride interface and this may play an additional role in composites' mechanical properties.

Due to the potential increase in oxidation resistance of the composites with addition of CrB_2, this additive should be investigated first. Crude oxidation tests measuring weight gain after various heat treatments in air have shown that combined additions of CrB_2 and AlB_{12} to $AlMgB_{14}$ lower the oxidation rate and form a more protective oxide later. As mentioned earlier, baseline $AlMgB_{14}$ forms a glassy, boron-rich oxide layer that is only moderately protective. As described in Chapter 6 and as was done with Zr additions to TiB_2, attempts should be made to produce $Cr_{0.5}Ti_{0.5}B_2$ by MA. Whether this results in a single phase diboride or two phase mixture, it could still be a useful additive to $AlMgB_{14}$. $AlMgB_{14}$ - 60 vol% $Cr_{0.5}Ti_{0.5}B_2$ would be a good composition for initial investigation. XRD would be necessary to verify the formation of the expected phases. While CrB_2 additions are expected to result in somewhat reduced hardness, erosion testing should be performed to ensure that it does not cause a drastic reduction in wear resistance. This would give an initial indication to the chemical stability and bonding between the phases. Additionally, SEM analysis of polished and fractured surfaces should be compared to the same for $AlMgB_{14}$-TiB_2 composites. If significant differences, such as unwanted phases or intergranular fracture, are not discovered, major concerns revolving around this

addition should be alleviated. Oxidation tests of $AlMgB_{14}$-TiB_2 and -$(TiCr)B_2$ composites would be needed to determine if the addition of Cr to the oxide layer has any benefit. Small bars of material with equal surface area cut from these samples by EDM would be suitable for thermogravimetric analysis (TGA) in flowing air.

Whether to the benefit or detriment of the composites, such alterations of both the 1:1:14 and diboride phases could provide valuable information. CrB_2 additions should be the highest priority of these exploratory investigations as it could have immediate industrial applications. Due to the potential solubility of CrB_2 and TiB_2, any range of compositions could be prepared depending on the desired balance between hardness and corrosion resistance. Throughout the field of materials engineering, every material has its pros and cons and it would be wise to diversify the family of $AlMgB_{14}$ - TiB_2 composites to broaden the scope of potential applications.

7.4: Acknowledgment

This work was performed at Ames Laboratory under Contract No. DE-AC02-07CH11358 with the U.S. Department of Energy through the Energy Efficiency and Renewable Energy Industrial Technologies Program. The United States government has assigned the DOE Report number IS-T 2888 to this thesis.

References:

[1] S. Vepřek, A.S. Argon, Journal of Vacuum Science and Technology B 20 (2002) 650-664.

[2] J.E. Lowther, Physica B 322 (2002) 173-178.

[3] B.A. Cook, J. L. Harringa, T. L. Lewis, A. M. Russell, Scripta Materialia 42 (2000) 597-602.

[4] S. Okada, K. Kudou, T. Mori, T. Shishido, I. Higashi, N. Kamegashira, K. Nakajima, T. Lundström, Materials Science Forum 449-452 (2004) 365-368.

[5] H. Werheit, U. Kuhlmann, G. Krach, I. Higashi, T. Lundström, Y. Yu, Journal of Alloys and Compounds 202 (1993) 269-281.

[6] I. Higashi, Journal of the Less-Common Metals 82 (1981) 317-323.

[7] A. Guette, M. Barret, R. Naslain, P. Hagenmuller, L.E. Tergenius, T. Lundström, Journal of the Less-Common Metals 82 (1981) 325-334.

[8] V.I. Matkovich, J. Economy, Acta Crystallographica B 26 (1970) 616-621.

[9] I. Higashi, T. Ito, Journal of the Less-Common Metals 92 (1983) 239-246.

[10] M.M. Korsukova, V.N. Gurin, Y.B. Kuzma, N.F. Chaban, S.I. Chykhrii, V.V. Moshchalkov, N.B. Brandt, A.A. Gippius, K.K. Nyan, Physica Status Solidi 114 (1989) 265-272.

[11] M.M. Korsukova, L.E. Tergenius, T. Lundström, V.N. Gurin, Journal of Alloys and Compounds 187 (1992) 39-48.

[12] M.M. Korsukova, V.N. Gurin, L.E. Tergenius, T. Lundström, Journal of Alloys and Compounds 190 (1993) 185-187.

[13] R. Cherukuri, P. Molian, Machining Science and Technology 7 (2003) 119-135.

[14] T.L. Lewis, A study of selected properties and applications of $AlMgB_{14}$ and related composites: Ultra-hard materials, M.S. Thesis, Iowa State University 2001.

[15] Y. Peng, T. Ishigaki, S. Horiuchi, Applied Physics Letters 73 (1998) 3671-3673.

[16] P. Lemis-Petropoulos, V. Kapaklis, A.B. Peikrishvili, C. Politis, International Journal of Modern Physics B 17 (2003) 2781-2788.

[17] K.A. Schwetz, L.S. Sigl, J. Greim, H. Knoch, Wear 181-183 (1995) 148-155.

[18] F. Gao, J. He, E. Wu, S. Liu, D. Yu, D. Li, S. Zhang, Y. Tian, Physical Review Letters 91 (2003) 015502.

[19] S. Vepřek, M.G.J. Veprek-Heijman, P. Karvankova, J. Prochazka, Thin Solid Films 476 (2005) 1-29.

[20] A.Y. Liu, M.L. Cohen, Science 245 (1989) 841-842.

[21] Y.H. Han, J.F. Luo, C.X. Gao, H.A. Ma, A.M. Hao, Y.C. Li, X.D. Li, J. Liu, M. Li, H.W. Liu, G.T. Zou, Chinese Physics Letters 22 (2005) 1347-1349.

[22] S. Vepřek, Surface and Coatings Technology 97 (1997) 15-22.

[23] D.M. Teter, MRS Bulletin 23 (1998) 22-27.

[24] B.A. Cook, J. L. Harringa, T. L. Lewis, A. M. Russell, Journal of Advanced Materials 36 (2004) 56-63.

[25] Y. Lee, B.N. Harmon, Journal of Alloys and Compounds 338 (2002) 242-247.

[26] Callister, William D., Jr, Materials Science and Engineering, An Introduction 5th Edition Wiley, New York 2000.

[27] S. Yip, Nature 391 (1998) 532-533.

[28] R.A. Masumura, P.M. Hazzledine, C.S. Pande, Acta Materialia 46 (1998) 4527-4534.

[29] S. Christiansen, M. Albrecht, H.P. Strunk, S. Vepřek, Journal of Vacuum Science and Technology B 16 (1998) 19-22.

[30] S. Vepřek, S. Mukherjee, P. Karvankova, H.D. Männling, J.L. He, K. Moto, J. Prochazka, A.S. Argon, Thin Solid Films 436 (2003) 220-231.

[31] S. Vepřek, Journal of Vacuum Science and Technology A 17 (1999) 2401-2420.

[32] S. Vepřek, M. Jilek, Vacuum 67 (2002) 443-449.

[33] S. Vepřek, H.D. Männling, M. Jilek, P. Holubar, Materials Science and Engineering A 366 (2004) 202-205.

[34] S. Vepřek, Reviews on Advanced Materials Science 5 (2003) 6-16.

[35] S. Vepřek, The European Physical Journal Applied Physics 28 (2004) 313-317.

[36] J.S. Koehler, Physical Review B 2 (1970) 547-551.

[37] C. Pfohl, A. Bulak, K.T. Rie, Surface and Coatings Technology 131 (2000) 141-146.

[38] F. Kunc, J. Musil, P.H. Mayrhofer, C. Mitterer, Surface and Coatings Technology 174-5 (2003) 744-753.

[39] P.H. Mayrhofer, C. Mitterer, J.G. Wen, J.E. Greene, I. Petrov, Applied Physics Letters 86 (2005) 131909.

[40] J. Musil, H. Zeman, F. Kunc, J. Vlcek, Materials Science and Engineering A 340 (2003) 281-285.

[41] N. Dubrovinskaia, V. L. Solozhenko, N. Miyajima, V. Dmitriev, O.O. Kurakevych, L. Dubrovinsky, Applied Physics Letters 90 (2007) 101912.

[42] C. Frondel, U.B. Marvin. Nature 214 (1967) 587–589.

[43] R.A. Andrievski, Surface and Coatings Technology 201 (2007) 6112-6116.

[44] B.R. Lawn, Journal of Materials Research 19 (2004) 22-29.

[45] V. Brazhkin, N. Dubrovinskaia, M. Nicol, N. Novikov, R. Riedel, V. Solozhenko, Y. Zhao, Nature Materials 3 (2004) 576-577.

[46] A.C. Fischer-Cripps, P. Karvankova, S. Vepřek, Surface and Coatings Technology 200 (2006) 5645-5654.

[47] T. Ito, I. Higashi, Acta Crystallographica B 39 (1983) 239-243.

[48] D. Emin, Physics Today 40 (1987) 55-62.

[49] A.M. Russell, B.A. Cook, J.L. Harringa, T.L. Lewis, Scripta Materialia 46 (2002) 629-633.

[50] I. Higashi, M. Kobayashi, S. Okada, K. Hamano, T. Lundström T. Journal of Crystal Growth 128 (1993) 1113-1119.

[51] I. Higashi, Journal of Solid State Chemistry 32 (1980) 201-212.

[52] R.D. Shannon, C.T. Prewitt, Acta Crystallographia B 26 (1970) 1046-1048.

[53] K.L. Barbalace, Periodic Table of Elements - Sorted by Ionic Radius. "http://EnvironmentalChemistry.com/yogi/periodic/ionicradius.html" EnvironmentalChemistry.com 1995 - 2007. Accessed: 6/23/2007.

[54] B. Post, F.W. Glaser, D. Moskowitz, Acta Metallurgica 2 (1954) 20-25.

[55] I. J. McColm, D. Phil, Ceramic Science for Materials Technologists, Leonard Hill, New York 1983.

[56] A.M. Russell, K.L. Lee, Structure-Property Relations in Nonferrous Metals, Wiley, New Jersey 2005.

[57] R. Königshofer, S. Fürnsinn, P. Steinkellner, W. Lengauer, R. Haas, K. Rabitsch, M. Scheerer, International Journal of Refractory Metals & Hard Materials 23 (2005) 350-357.

[58] H. Schmidt, G. Borchardt, C. Schmalzried, R. Telle, S. Weber, H. Scherrer, Journal of Applied Physics 93 (2003) 907-911.

[59] W.A. Zdaniewski, Journal of the American Ceramic Society 70 (1987) 793-97.

[60] M. Moriyama, H. Aoki, Y. Kobayashi, Journal of the Ceramic Society of Japan 106 (1998) 1196-1200.

[61] F. Monteverde, A. Bellosi, S. Guicciardi, Journal of the European Ceramic Society 22 (2002) 279-288.

[62] W.M. Wang, H. Wang, Z.Y. Fu, Key Engineering Materials 249 (2003) 109-114.

[63] H. Holleck, H. Leiste, W. Schneider, International Journal of Refractory & Hard Metals 6 (1987) 149-154.

[64] L.H. Li, H.E. Kim, E.S. Kang. Journal of the European Ceramic Society 22 (2002) 973-977.

[65] M. Gu, C. Huang, B. Zou, B. Liu, Materials Science Engineering A 433 (2006) 39-44.

[66] D.B. Lee, Y.C. Lee, D.J. Kim, Oxidation of Metals 56 (2001) 177-189.

[67] M.G. Barandika, J.J. Echeberría, J.M. Sánchez, F. Castro, Journal of Materials Chemistry 8 (1998) 1851-1857.

[68] Y.V. Levinskii, A.P. Petrov, Inorganic Materials 31 (1995) 298-300.

[69] A. Ahmed, S. Bahadur, B.A. Cook, J. Peters, Tribology International 39 (2006) 129-137.

[70] A. Ahmed, S. Bahadur, A. Russell, B.A. Cook, "Diamond belt abrasion resistance and cutting tool wear studies on new ultra-hard boride materials." *article in press*.

[71] J. Peters, B.A. Cook, J.H. Harringa, A.M. Russell, Proceedings of the 2003 International Conference on Powder Metallurgy & Particulate Materials Pt 2, 106-116.

[72] R.B. Schwarz, Scripta Materialia 34 (1996) 1-4.

[73] H. Zoz, H. Ren, Materials Science Forum 343-6 (2000) 955-963.

[74] C.C. Koch, Annual Review of Materials Science 19 (1989) 121-143.

[75] P.B. Wheelock, B.C. Cook, J.L. Harringa, A.M. Russell, Journal of Materials Science 39 (2004) 343-347.

[76] T.H. Courtney, D. Maurice, Scripta Materialia 34 (1996) 5-11.

[77] L. Lu, M.O. Lai, S. Zhang, Journal of Materials Processing Technology 52 (1995) 539-546.

[78] L. Takacs, Progress in Materials Science 47 (2002) 355-414.

[79] C. Deidda, F. Delogu, G. Cocco, Journal of Materials Science 39 (2004) 5315-5318.

[80] G. Manai, F. Delogu, L. Schiffini, G. Cocco, Journal of Materials Science 39 (2004) 5319-5324.

[81] P. Millet, T. Hwang, Journal of Materials Science 31 (1996) 351-355.

[82] Y. Hwang, J.K. Lee, Materials Letters 54 (2002) 1-7.

[83] D.D. Radev, D. Klisurski, Journal of Alloys and Compounds 206 (1994) 39-41.

[84] T.S Ward, W. Chen, M. Schoenitz, R.N. Dave, E.L. Dreizin, Acta Materialia 53 (2005) 2909-2918.

[85] J.W. Kim, H.S. Chung, S.H. Lee, K.H. Oh, J.H. Shim, Y.W. Cho, Intermetallics 15 (2007) 206-210.

[86] R.M. Davis, B. McDermott, C.C. Koch, Metallurgical Transactions A 19 (1988) 2867-2874.

[87] D.R. Maurice, T.H. Courtney, Metallurgical Transactions A 21 (1990) 289-303.

[88] B.R. Lawn, Fracture of Brittle Solids 2nd Edition, Cambridge University Press, Cambridge 1993.

[89] B.A. Cook, J.L. Harringa, J.S. Peters, A.M. Russell, "Wear Resistance of $AlMgB_{14}$ - TiB_2 Composites," *submitted to Wear*.

[90] I. Finnie, Wear 3 (1960) 87-103.

[91] I. Finnie, Wear 186-7 (1995) 1-10.

[92] Q. Chen, D.Y. Li, Wear 254 (2003) 203-210.

[93] A.G. Evans, Journal of the American Ceramic Society 73 (1990) 187-206.

[94] K. Xia, T.G. Langdon, Journal of Materials Science 29 (1994) 5219-5231.

[95] T. Ohji, Y.K. Jeong, Y.H. Choa, K. Niihara, Journal of the American Ceramic Society 81 (1998) 1453-1460.

[96] A.G. Evans, K.T. Faber, Journal of the American Ceramic Society 64 (1981) 394-398.

[97] Q. Chen, D.Y. Li, Wear 255 (2003) 78-84.

[98] J. Hu, D.Y. Li, R. Llewellyn, Wear 259 (2005) 6-17.

[99] G.R. Anstis, P. Chantikul, B.R. Lawn, D.B. Marshall, Journal of the American Ceramic Society 64 (1981) 533-538.

[100] D. Chicot, A. Pertuz, F. Roudet, M.H. Staia, J. Lesage, Materials Science and Technology 20 (2004) 877-884.

[101] T.L. Lewis, A.M. Russell, B.A. Cook, J.L. Harringa, Mat Sci & Engineering A 351 (2003) 117-122.

[102] C.B. Finch, P.F. Becher, P. Angelini, S. Baik, C.E. Bamberger, J. Brynestad, Advanced Ceramic Materials 1 (1986) 50-54.

[103] K. Shobu, T. Watanabe, Advances in Ceramics 24 (1998) 1091-1099.

[104] T. Watanabe, K. Shobu, Journal of the American Ceramic Society 68 (1985) C34-C36.

[105] R. Telle, S. Meyer, G. Petzow, E.D. Franz, Materials Science and Engineering A 105-106 (1988) 125-129.

[106] V. Bedekar, D.G. Bhat, S.A. Batzer, L. Walker, L. Allard, Annual Regional ASME – GSTC Conference. March 2003.

[107] V. Bedekar, D.G. Bhat, S.A. Batzer, Machining Science and Technology 8 (2004) 341-355.

[108] R. Cherukuri, M. Womack, P. Molian, A. Russell, Y. Tian, Surface and Coatings Technology 155 (2002) 112-120.

[109] Y. Tian, A. Constant, C.C.H. Lo, J.W. Anderegg, A.M. Russell, J.E. Snyder, P. Molian, Journal of Vacuum Science and Technology A 21 (2003) 1055-1063.

[110] Y. Tian, A.F. Bastawros, C.C.H. Lo, A.P. Constant, A.M. Russell, B.A. Cook, Applied Physics Letters 83 (2003) 2781-2783.

[111] B.A. Cook, Personal Interview, Ames, Iowa: Ames Laboratory 2002-2007.

[112] O. Gedeon, K. Jurek, V. Hulínský, Journal of Non-Crystalline Solids 246 (1999) 1-8.

[113] K. Jurek, O. Gedeon, Spectrochimica Acta B 58 (2003) 741-744.

[114] J. Zemek, P. Jiricek, O. Gedeon, B. Lesiak, A. Jozwik, Journal of Non-Crystalline Solids 351 (2005) 1665-1674.

[115] J. Zemek, O. Gedeon, Journal of Non-Crystalline Solids 337 (2004) 268-271.

[116] A.P. Boresi, K.P. Chong, Elasticity in Engineering Mechanics 2nd Edition, Wiley, New York 2000.

[117] J.M. Hill, D.C. Johnston, B.A. Cook, J.L. Harringa, A.M. Russell, Journal of Magnetism and Magnetic Materials 265 (2003) 23-32.

[118] H.M. Rietveld, Journal of Applied Crystallography 2 (1969) 65-71.

[119] V.K. Pecharsky, P.Y. Zavalij, Fundamentals of powder diffraction and structural characterization of materials, Kluwer Academic Publishers, Boston 2003.

[120] S. Veprek, P. Nesladek, A. Niederhofer, F. Glatz, NanoStructured Materials 10 (1998) 679-689.

[121] A.G. Evans, M.E. Gulden, M. Rosenblatt, Procedures of the Royal Society of London A 361 (1978) 343-365.

[122] L. Lu, M.O. Lai, H.Y. Wang, Journal of Materials Science 35 (2000) 241-248.

[123] S. Torizuka, K. Sato, H. Nishio, T. Kishi, Journal of the American Ceramic Society 78 (1995) 1606-1610.

[124] T. Watanabe, Ceramic Bulletin 59 (1980) 485-486.

[125] P.F. Becher, C.B. Finch, M.K. Ferber, Journal of Materials Science Letters 5 (1986) 195-197.

[126] J.H. Park, Y.H. Lee, Y.H. Koh, H.E. Kim, S.S. Baek, Journal of the American Ceramic Society 83 (2000) 1542-1544.

[127] S. Baik, P.F. Becher, Journal of the American Ceramic Society 70 (1987) 527-530.

[128] Y.H. Park, H. Hashimoto, T. Abe, Materials Science and Engineering A 181-182 (1994) 1291-1295.

[129] J.A. Hawk, D.E. Alman, Wear 225-229 (1999) 544-556.

[130] J.J. Kim, S.K. Park, Journal of Materials Science Letters 16 (1997) 821-823.

[131] S.J. Cho, C.D. Um, S.S. Kim, Journal of the American Ceramic Society 79 (1996) 1247-1251.

[132] A.F. Colclough, J.A. Yeomans, Journal of Hard Materials 3 (1992) 53-61.

[133] R. Riedel, Handbook of Ceramic Hard Materials, Vol 2, Wiley-VCH, Weinheim, Germany 2000.

[134] K.B. Shim, J. Kwiencinski, M.J. Edirisinghe, B. Ralph, Materials Science Forum 189-190 (1995) 129-134.

[135] T.B. Massalski, Binary Alloy Phase Diagrams 2nd Edition, Vol 1, ASM International, Materials Park, Ohio 1990.

[136] H.Y. Chung, M.B. Weinberger, J.B. Levine, A. Kavner, J.M. Yang, S.H. Tolbert, R.B. Kaner, Science 316 (2007) 436-439.

[137] L. Shi, Y. Gu, L. Chen, Z. Yang, J. Ma, Y Qian, Materials Letters 58 (2004) 2890-2892.

[138] M. Audronis, P.J. Kelly, R.D. Arnell, A. Leyland, A. Matthews, Surface and Coatings Technology 200 (2005) 1366-1371.